TAMPEREEN TEKNILLINEN YLIOPISTO
TAMPERE UNIVERSITY OF TECHNOLOGY

Sanna Vesti

Methodology for Dynamic Stability and Robustness Analysis of Commercial-Power-Module-Based DC-Distributed Systems

Julkaisu 1326 • Publication 1326

Tampere 2015

Tampereen teknillinen yliopisto. Julkaisu 1326
Tampere University of Technology. Publication 1326

Sanna Vesti

Methodology for Dynamic Stability and Robustness Analysis of Commercial-Power-Module-Based DC-Distributed Systems

Thesis for the degree of Doctor of Science in Technology to be presented with due permission for public examination and criticism in Rakennustalo Building, Auditorium RG202, at Tampere University of Technology, on the 9th of October 2015, at 12 noon.

Tampereen teknillinen yliopisto - Tampere University of Technology
Tampere 2015

ISBN 978-952-15-3584-0 (printed)
ISBN 978-952-15-3591-8 (PDF)
ISSN 1459-2045

ABSTRACT

The purpose of this thesis is to present dynamic small-signal stability and performance analysis methodology for dc-distributed systems consisting of commercial power modules. Furthermore, the objective is to introduce simple method to state the least conservative margins for robust stability as a single number. In addition, an index characterizing the overall system stability is obtained, based on which different dc-distributed systems can be compared in terms of robustness.

The interconnected systems are prone to impedance-based interactions which might lead to transient-performance degradation or even instability. These systems typically are constructed using commercial converters with unknown internal structure. Therefore, the analysis presented throughout this thesis is based on frequency responses measurable from the input and output terminals. The stability margins are stated utilizing a concept of maximum peak criteria, derived from the behavior of impedance-based sensitivity function that provides a single number to state robust stability. Using this concept, the stability information at every system interface is combined to a meaningful number to state the average robustness of the system. In addition, theoretical formulas are extracted to assess source and load side interactions in order to describe detailed couplings within the system. The presented theoretical analysis methodologies are experimentally validated throughout the thesis.

In this thesis, according to the presented analysis, the least conservative stability margins are provided as a single number guaranteeing robustness. It is also shown that within the interconnected system the robust stability is ensured only if the impedance-based minor-loop gain is determined at the very input or output of each subsystem. Moreover, a complete set of impedance-type internal parameters as well as the formulas according to which the interaction sensitivity can be fully explained and analyzed, is provided. The given formulation can be utilized equally either based on measured frequency responses, time-domain identified internal parameters or extracted analytic transfer functions.

Based on the analysis methodologies presented in this thesis, the stability and performance of interconnected systems consisting of converters with unknown internal structure, can be predicted. Moreover, the provided concept to assess the least conservative stability margins enables to obtain an index to state the overall robust stability of distributed power architecture and thus to compare different systems in terms of stability.

PREFACE

This research work was performed as a collaboration project between the Centro de Electronica Industrial (CEI) at Universidad Politecnica de Madrid (UPM) and the Department of Electrical Energy Engineering (DEEE) at Tampere University of Technology (TUT) during the years 2010-2013. The work was funded by personal grants from the Emil Aaltonen foundation and the Ministerio de Ciencia e Innovacion of Spain through the project (MOREGREEN) Modelos Rapidos Equivalentes para Gestion de Redes Electronicas de Energia (DPI2010-17466).

First of all, I want to express my deepest and the most sincere gratitude to my thesis supervisor Professor Teuvo Suntio for his guidance and endless support during these years. Without him, I would have never continued towards the PhD. Furthermore, I am especially grateful to my other supervisor, Dr. Jesus A. Oliver for all his help and valuable technical advices as well as feedback and also to Dr. Roberto Prieto for his help and support related to the MOREGREEN project. In addition, I want to thank Dr. Richard Redl and Dr. Alon Kuperman for examining my thesis.

I want to thank all my former colleagues in Madrid for the great years we spent together at the university and especially outside work and to Dejana Cucak for the nice coffee and lunch breaks during these years. I am also very grateful to the colleagues in DEEE for helping me with the measurements and for creating such a great working atmosphere.

Finally, I want to thank my parents Arja and Jorma for their support during my years at the university as well as my brother Jussi and sister Laura for always being there for me. My deepest thanks to all my amazing friends in Finland, Spain, Austria and everywhere in the world for their encouragements. A special thanks to my husband David for his patience and continuous support and who always kept believing in me.

Villach, August 2015

Sanna Vesti

SYMBOLS AND ABBREVIATIONS

ABBREVIATIONS

A	Ampere
AC, ac	Alternative current
CCM	Continuous conduction mode
CF	Current-fed (i.e. supplied by a current source)
ctrl	control
DC, dc	Direct current
DCM	Discontinuous conduction mode
DDR	Direct-duty-ratio
dB	Decibel
dBΩ	Decibel-ohm
DSP	Digital signal processor, processing
EET	Extra element theorem
EMI	Electromagnetic interference
ESR	Equivalent series resistance
G	G-parameter model (i.e. voltage-to-voltage)
GM	Gain margin
GM_{MPC}	Gain margin obtained from MPC criteria
G.M.	Geometric mean
H.M.	Harmonic mean
Hz	Hertz
IBA	Intermediate bus architecture
IVFF	Input-voltage-feedforward
ML	Minor-loop gain
MPP	Maximum power point
MPC	Maximum peak criteria
OC	Open circuit
OCF	Output-current-feedforward
PBSC	Passivity based stability criterion
PE	Power electronics
PM	Phase margin
PM_{MPC}	Phase margin obtained from MPC criteria
PCM	Peak-current-mode control
POL	Point-of-load
PV	Photovoltaic
PWM	Pulse width modulation
RHP	Right half of the complex plane

S	Sensitivity function
SC	Short circuit
SSA	State space averaging
T	Complementary sensitivity function
V	Volt
VM	Voltage-mode
W	Watt
Y	Y-parameter model (i.e. voltage-to-current)

GREEK CHARACTERS

Δ	small perturbation
ω_{c}	Gain crossover frequency (rad/s)
ω_{RHP}	RHP (pole/zero) frequency (rad/s)
ω_{180}	Phase crossover frequency (rad/s)
Ω	Ohm

LATIN CHARACTERS

C	Capacitance
C	Capacitor
$\hat{c}$	General control variable
d	Duty ratio
$\hat{d}$	Perturbed duty ratio
D	Steady-state value of the duty ratio
F_{m}	Duty-ratio gain
G_{a}	Modulator gain
G_{cc}	Controller transfer function
G_{ci}	Control-to-input transfer function
G_{co}	Control-to-output transfer function
G_{cr}	Cross-coupling admittance
G_{io}	Audiosusceptibility, input-to-output transfer function
$G_{\mathrm{se\text{-}v}}$	Sensing gain
H_{i}	Output current feedforward gain
i_{C}	Capacitor current
i_{in}	Input current
$\hat{i}_{\mathrm{in}}$	Perturbed input current
i_{L}	Inductor current
$\hat{i}_{\mathrm{L}}$	Perturbed inductor current
i_{o}	Output current
$\hat{i}_{\mathrm{o}}$	Perturbed output current
I_{in}	Average input current

I_{L}	Average load or inductor current
I_{o}	Average output current
$\mathbf{I}$	Identity matrix
j	Complex variable
L	Inductance
L	Inductor
L_{in}	Loop gain for input-current control loop
L_{out}	Loop gain for output-voltage control loop
q_{c}	Inductor-current feedback gain
q_{i}	Input-voltage feedforward gain
r_{C}	Equivalent series resistance of a capacitor
r_{d}	Diode resistance (non-linear)
r_{E}	Equivalent resistance in a current path
r_{L}	Equivalent series resistance of an inductor
r_{ds}	Switch on-state resistance
R_{s1}	Equivalent inductor current sensing resistor
R_{s2}	Equivalent output current sensing resistor
R_{load}	Load resistance
s	Laplace variable
T_{oi}	Reverse (output-to-input) transfer function
u_{d}	Diode voltage
u_{in}	Input voltage
$\hat{u}_{\mathrm{in}}$	Perturbed input voltage
u_{C}	Capacitor voltage
u_{ref}	Reference voltage
u_{L}	Inductor voltage
u_{o}	Output voltage
$\hat{u}_{\mathrm{o}}$	Perturbed output voltage
U_{C}	Average capacitor voltage
U_{E}	Equivalent voltage
U_{in}	Average input voltage
U_{o}	Average output voltage
Y_{in}	Input admittance
Z_{bus}	Bus impedance
Z_{D}	Driving point impedance
Z_{N}	Null impedance
Z_{in}	Input impedance
Z_{o}	Output impedance

SUBSCRIPTS

-∞	Ideal transfer function
c	Closed-loop
F	Filter
in	Input
L	Load, load-affected
max	Maximum
min	Minimum
o	Output, open-loop
oc	Open-circuit
oci	Open-circuit input
RHP	Right half of the complex plane
rms	Root mean square value
S	Source, source-affected
sco	Short-circuit output

SUPERSCRIPTS

-1	Matrix inverse
G	G-parameter model (i.e. voltage-to-voltage)
H	H-parameter model (i.e. current-to-current)
IF	Input-voltage-feedforward
L	Load-affected
S	Source-affected
T	Transpose
OCF	Output-current feedforward
PCM	Peak-current-mode
VM	Voltage-mode
Y	Y-parameter model (i.e. voltage-to-current)
Z	Z-parameter model (i.e. current-to-voltage)

CONTENTS

1 INTRODUCTION

This thesis focuses on the analysis of distributed dc-systems consisting of commercial converters. The first chapter of this thesis introduces the main motivation and objectives for the performed research work as well as provides a comprehensive review of the relevant state-of-the art. First, the general dc-distributed system structure and its main application fields are discussed and the origin of the stability problem occurring within these systems due to the impedance-based interactions, is explained. Moreover, the current methods to assess the small-signal stability and to state the stability margins are introduced as well as the modelling approaches applicable to commercial converters. Finally, the main motivation and objectives for this thesis are given describing the main contributions.

1.1 DC-distributed systems

Distributed system refers to a power system architecture where the loads are being individually supplied by switching converters from a bus voltage, which can be either ac or dc (Liukkonen et al., 2013; Luo and Batarseh, 2005, 2006; Sun, 2009). Traditionally, the dc-distributed systems are widely used to process electricity in various application fields such as telecom, ship, avionic and automotive (Brush, 2003; D.Boroyevic et al., 2010; Emadi and Ehsani, 2000; Khalig, 2008; Sayani and Wanes, 2003; Sudhoff et al., 2002). Currently, the dc-systems are also gaining popularity in facilitating the integration of renewable energy sources and modern electronic loads in the most recent power system applications over the ac-bus voltage systems (Balog and Krein, 2011; Kwasinski, 2011; Rodriguez et al., 2013).

In distributed systems, the dc-dc converters are located at the point-of-use performing the power processing at close proximity to the load (Brush, 2003). This system structure replaced the centralized architecture, which was based on a single custom designed converter with multiple outputs that supplied the loads (Brush, 2003; Sayani and Wanes, 2003). The main advantage of the distributed system structure is the possibility to use standard commercial modules, which can be connected in multiple ways to supply various system loads according to their specific requirements (Abe et al., 2008; F. Lee, 1993; Mammano, 1993; Tabisz et al., 1992). An example of a traditional dc-distributed system for a telecom application is shown in Fig. 1.1.

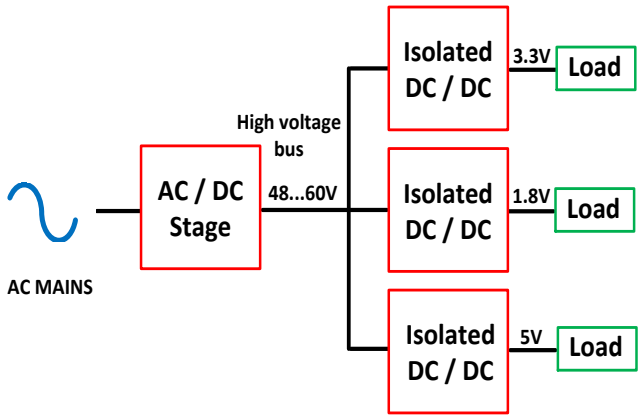

Fig. 1.1: Typical dc-distributed system for telecom application (Brush, 2003; Sayani and Wanes, 2003).

The ac-voltage is rectified to a bus voltage level, typically 48V, and thereafter, the isolated dc-dc converters supply various loads according to their specifications from this bus voltage (Brush, 2003; F. Lee, 1993; Miftakhutdinov, 2009; Sayani and Wanes, 2003). In addition to the dc-dc converters, the systems typically include input filters and other protection elements depending on the intended application field (Hentunen et al., 2004; Liu et al., 201; Oliver et al., 2009; Vesti et al., 2010).

Modern distributed systems consist of different loads, such as microprocessors, which set multiple stringent requirements to the supply voltages in terms of fast transient response and low supply voltage (Abe et al., 2008; F. Lee, 1993). Therefore, to better feed these critical loads, intermediate bus architecture (IBA) was introduced. This architecture refers to a system, where tightly regulated, high efficiency and power-density-optimized point-of-load (POL) converters (Bebic et al., 2010; Foley et al., 2010; López and Alarcon, 2012) are utilized to provide the specific supply voltages for a variety of digital and analog loads (Abe et al., 2008; F. Lee, 1993; Miftakhutdinov, 2009; Tabisz et al., 1992). These low-cost converters are non-isolated and operate from lower input voltage level. Therefore, an intermediate bus converter is required to provide isolation and supply voltage for the POL modules. The IBA for a telecom application is illustrated in Fig. 1.2.

The design of the high-frequency POL converter is extremely demanding especially as the converter has to be optimized in terms of low cost, high efficiency, reliability and short time-to-market. Therefore, the utilized converters in distributed systems are typically commercial. Various manufacturers provide a wide selection of commercial POL converters for different applications. The distributed system is designed according

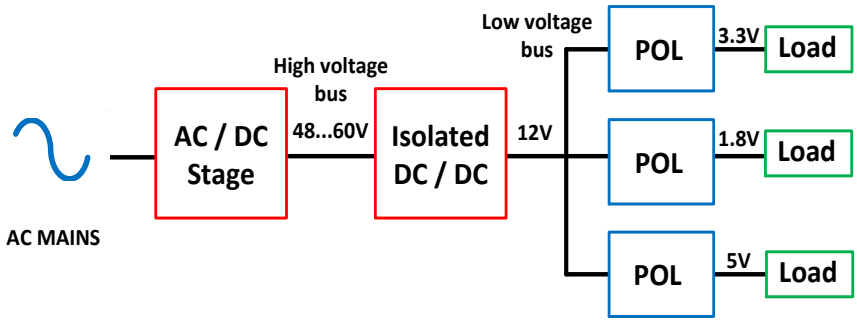

Fig. 1.2: Intermediate bus architecture for telecom application (Brush, 2003; Miftakhutdinov, 2009; Tabisz et al., 2005).

to the predefined specifications and the components are selected in order to supply the loads based on their requirements. The final system architecture may become extremely complicated as the typical design objective of the overall system is to optimize the size, cost and efficiency as well as time-to-market (D.Boroyevic et al., 2010; Luo and Batarseh, 2005).

1.2 System stability and performance

The commercial converters for the distributed systems are selected based on their stand-alone performance according to the datasheet specifications provided by the manufacturer. This stand-alone behavior is typically specified assuming ideal source and load even though in a real system they are hardly ideal. The selected converters are, nevertheless, expected to work in a real system as defined in the datasheet. In the actual system couplings between the input and output impedances exist and adverse interactions might occur in the system leading to a performance degradation or even instability. The consequences of possible interactions are best observed in the time-domain while analyzing the transient performance of the converter. However, the time-domain analysis does not provide any information regarding the origin of the problem, and therefore, in order to better understand the system interactions, the analysis shall be performed in the frequency domain.

1.2.1 Interconnected system

A cascade connection is the most frequently used way to interconnect the system components, converters and filters, to form a distributed system that complies with the predefined requirements for a specific application. In a real system, subsequent to the

system integration, unintentional couplings through the input and output impedances exist, changing the system dynamics. These couplings can be analyzed based on simplified cascaded connection of two subsystems as shown in Fig. 1.3, where Z_{S} is the source output impedance and Z_{L} is the load input impedance.

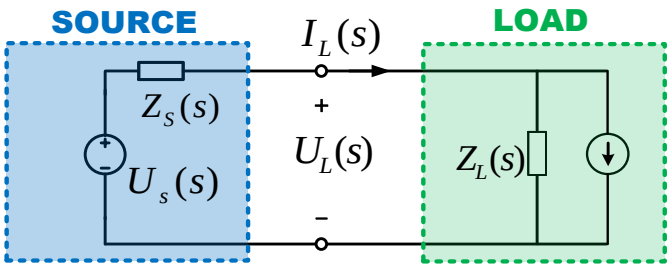

Fig. 1.3: Cascaded source and load module.

These source and the load modules can be either a filter or a dc-dc converter. The behavior of this interconnected system can be analyzed expressing the current from source module to the load module as in (1.1).

$$I_{\mathrm{L}}(s) = \frac{U_{\mathrm{L}}(s)}{Z_{\mathrm{L}}(s)} = \frac{U_{\mathrm{s}}(s)}{Z_{\mathrm{L}}(s)} \frac{1}{1 + \frac{Z_{\mathrm{S}}(s)}{Z_{\mathrm{L}}(s)}} \tag{1.1}$$

Based on this equation, it can be observed that the impedance ratio $Z_{\mathrm{S}}/Z_{\mathrm{L}}$ affects the source-load system behavior and introduces additional dynamics to the system. If both, the source and the load are assumed standalone stable referring that neither the impedance Z_{S} nor the admittance $1/Z_{\mathrm{L}}$ has any RHP poles, the stability of the interconnected system depends on the term $Z_{\mathrm{S}}/Z_{\mathrm{L}}$. This impedance ratio is called minor-loop gain and it can be considered as a system loop gain. It was first introduced by R. D. Middlebrook in the mid-1970s by publishing the input-filter design rules for a regulated converter in (Middlebrook, 1976) and (Middlebrook, 1978). According to these rules, the stability of a cascaded input filter and a dc-dc converter is guaranteed if the condition $Z_{\mathrm{in\_converter}} \gg Z_{\mathrm{o\_filter}}$ is valid (Middlebrook, 1976). Since then, this impedance-based stability analysis method has been frequently used to assess the small-signal stability of interconnected systems by applying the Nyquist criterion (Dorf and Bishop, 2001) to the

minor-loop gain. This stability analysis method is equally valid to assess the small-signal stability of both, dc- and ac- systems (Feng and Lee, 2000; Middlebrook, 1976; Sun, 2011; Wildrick et al., 1995).

Typically in distributed systems most of the energy sources are voltage sources and loads are current sinks. Therefore, the most usual dc-dc converter type is a voltage-to-voltage converter, referring that the input voltage is set by the source and the converter regulates its output voltage. For these traditional voltage-fed systems, the minor-loop gain is composed of the source subsystem output impedance and the load subsystem input impedance (Feng and Lee, 2000; Middlebrook, 1976; Sun, 2011; Wildrick et al., 1995) as was illustrated in Fig. 1.3 and (1.1).

The dc-dc converters can be divided into different types depending on the terminal characteristics of the system i.e. whether the supply is a voltage or current source and whether the load demands constant current or voltage. Therefore, each converter type has different dynamic features which can be represented with a set of transfer functions, depending on the terminal characteristics of the system (Leppaaho, 2008). Recently with the increasing research on the renewable energy systems it has been noticed that in order to correctly predict the stability of these systems, the impedance ratio has to be computed differently (Fangcheng et al., 2013; Leppaaho et al., 2011; Sun, 2009; Suntio et al., 2010) as a comparison to the conventional minor-loop gain.

The proper way to obtain the minor-loop gain can be observed based on general stability assessment of two interconnected subsystems. This interconnection can be represented according to Fig. 1.4 where the system input variables $\hat{x}_{\mathrm{in1}}$, $\hat{x}_{\mathrm{o2}}$, the output variables $\hat{y}_{\mathrm{in1}}$, $\hat{y}_{\mathrm{o2}}$ and the intermediate variables $\hat{x}_{\mathrm{s}}$, $\hat{y}_{\mathrm{s}}$ can be either currents or voltages depending on the terminal characteristics.

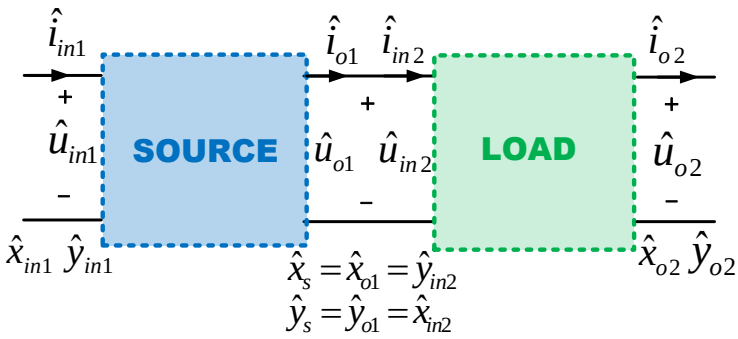

Fig. 1.4: General interconnection of the source and load-subsystems subsystems.

The dynamics of individual subsystems can be obtained without defining the type of the source or the load. The source subsystem can be presented as in (1.2), where the internal transfer functions are denoted as S_{11} to S_{22} and correspondingly, the load subsystem is given as in (1.3), where the internal transfer functions are denoted as L_{11} to L_{22}. Therefore, the overall input-output representation of this interconnected system is obtained as in (1.4) (Leppaaho, 2008) based on which the system stability can be assessed.

$$\begin{bmatrix} \hat{y}_{\mathrm{in1}} \\ \hat{y}_{\mathrm{s}} \end{bmatrix} = \begin{bmatrix} S_{11} & S_{12} \\ S_{21} & -S_{22} \end{bmatrix} \begin{bmatrix} \hat{x}_{\mathrm{in1}} \\ \hat{x}_{\mathrm{s}} \end{bmatrix} \tag{1.2}$$

$$\begin{bmatrix} \hat{x}_{\mathrm{s}} \\ \hat{y}_{\mathrm{o2}} \end{bmatrix} = \begin{bmatrix} L_{11} & L_{12} \\ L_{21} & -L_{22} \end{bmatrix} \begin{bmatrix} \hat{y}_{\mathrm{s}} \\ \hat{x}_{\mathrm{o2}} \end{bmatrix} \tag{1.3}$$

$$\begin{bmatrix} \hat{y}_{\mathrm{in1}} \\ \hat{y}_{\mathrm{o2}} \end{bmatrix} = \begin{bmatrix} S_{11} + \frac{S_{12}S_{21}L_{11}}{1+S_{22}L_{11}} & \frac{S_{12}L_{12}}{1+S_{22}L_{11}} \\ \frac{S_{21}L_{21}}{1+S_{22}L_{11}} & -(L_{22} + \frac{S_{22}L_{12}L_{21}}{1+S_{22}L_{11}}) \end{bmatrix} \begin{bmatrix} \hat{x}_{\mathrm{in1}} \\ \hat{x}_{\mathrm{o2}} \end{bmatrix} \tag{1.4}$$

In order to guarantee stability of this interconnection, every transfer function has to be stable. Again, assuming both subsystems standalone stable, it can be observed from the equations that the stability is dependent on the denominator term $S_{22}L_{11}$. This analysis is valid for each interconnected system type independent on the terminal characteristics. The parameters S_{22} and L_{11} depend on the internal dynamics of the converter, determined by the applied feedback and the terminal characteristics of the system as explained in detail in (Leppaaho, 2008).

In the case of traditional voltage-fed converter, the parameters describing the internal converter dynamics are called G-parameters (Arnedo et al., 2008; Maranesi et al., 1988; Valdivia et al., 2009). Therefore, by inserting the set of G-parameters to characterize the dynamics of both source and load subsystems, the term $S_{22}L_{11}$ determining the stability of the interconnected system equals $Z_{\mathrm{o\_S}}/Z_{\mathrm{in\_L}}$, which is the traditional minor-loop gain obtained in (1.1). Whereas for the current-fed interface, typically encountered in photovoltaic applications (Leppaaho et al., 2011; Suntio et al., 2010), the term $S_{22}L_{11}$ equals $Z_{\mathrm{in\_L}}/Z_{\mathrm{o\_S}}$, which is the inverse of the minor-loop gain. Therefore, in order to correctly predict the stability of an arbitrary interconnected system, the numerator impedance has to be the internal impedance of the subsystem containing the voltage source or sink, and the denominator impedance the internal impedance of the subsystem containing the current sink or source, respectively.

In this thesis, the stability and performance analysis are focused on the traditional voltage-fed distributed system applications and only the G-parameters are applied. However, the presented analysis methods are equally valid for other types of systems as long as the correct terminal characteristics of each particular interface are considered.

1.2.2 Origin of stability problems in distributed system

The coupling within the system occurs through the input and output impedances of two cascaded subsystems as previously discussed. Therefore, the stability depends on the characteristics of the source and the load impedances. Instability occurs if the minor-loop gain $Z_{\text{o\_S}}/Z_{\text{in\_L}}$ equals -1, meaning that the input and output impedances have equal magnitudes with a phase shift of 180°. In the case of an ideal source (zero output impedance) or ideal load (infinite input impedance), it is obvious that no coupling would occur. In addition, if the condition $Z_{\text{in\_L}} \gg Z_{\text{o\_S}}$ (Middlebrook, 1976) is valid, the impedances are never overlapping and the stability is guaranteed. However, these conditions are not necessary in order to guarantee the system stability, and less conservative stability analysis criterion are generally applied in the design of distributed systems. These methods are reviewed in the following section.

The dc-dc converter is a problematic component within interconnected system, because it introduces destabilizing effects due to its negative resistance behavior at its input terminals (Cespedes et al., 2011; Kwasinski and Onwuchekwa, 2011; Middlebrook, 1976; Sokal, 1973). This behavior originates from its main functionality: supply constant and well regulated power to the load independent of the bus voltage variations. If the bus voltage increases, then the converter input current decreases to maintain the power level constant thus introducing negative incremental resistance characteristics at the converter input (Cespedes et al., 2011). This impedance is operating-point dependent and it is defined for certain input voltage and output current. The most critical condition for the system stability occurs at the lowest input impedance, i.e. maximum load current at the minimum input voltage. In practice, the converter's input impedance appears as a negative resistance only at low frequencies. This negative resistance behavior is illustrated in Fig. 1.5 showing measured input impedance of commercial converter TSR-1 Traco Power (Tracopower, 2009) obtained at three different operating points:

- $Z_{\text{in-load1}}$: $U_{\text{in}} = 5V$, $I_{\text{o}} = 0.5A$
- $Z_{\text{in-load2}}$: $U_{\text{in}} = 5V$, $I_{\text{o}} = 1A$
- $Z_{\text{in-load3}}$: $U_{\text{in}} = 12V$, $I_{\text{o}} = 0.5A$

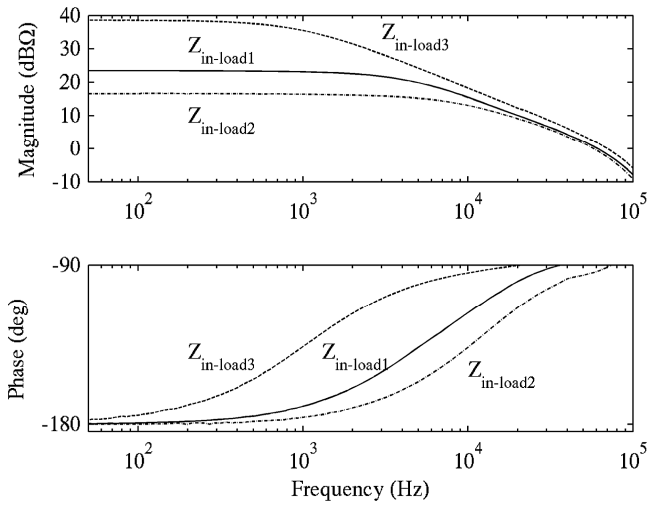

Fig. 1.5: Measured input impedances $Z_{\text{in-load1}}$, $Z_{\text{in-load2}}$, $Z_{\text{in-load3}}$ of a commercial module at the operating points U_{in}: 5V, I_{o}: 0.5A, U_{in}: 5V, I_{o}: 1A and U_{in}: 12V, I_{o}: 0.5A, respectively.

1.2.3 Small-signal stability analysis

Small-signal assessment refers to analysis performed at a certain operating point under small perturbations. Therefore, the utilized converter models are linearized around a specific operating point as will be explained in detail in the next section. The conventional method for assessing the small-signal stability of interconnected system is to apply the Nyquist criteria on the impedance-based minor-loop gain. In addition to ensure the system stability, it is important to know the stability margins indicating how close a stable system is to instability. Typically the results of the applied impedance-ratio-based stability assessment are presented as a certain forbidden region in the complex plane out of which the minor-loop gain shall stay for robust stability to exist (Sudhoff et al., 2000; Wildrick et al., 1995; X.Feng et al., 2002). These different forbidden regions provide certain gain (GM) and phase (PM) margins for the stability.

Middlebook's stability criterion $Z_{\text{in\_L}} \gg Z_{\text{o\_S}}$, can be considered to produce a forbidden region in a complex plane, which locates outside a circle having a center at the origin and a radius of inverse of the gain margin (GM) as illustrated in Fig. 1.6. The application of this criterion refers that the two impedances are not overlapping each other with a minimum margin of 6dB. This criterion is design oriented and easy to apply in practice, because it guarantees stability without the need of considering the phase behavior. However, for general stability assessment, it is considered to be too conservative and cost inefficient (Sudhoff et al., 2000). As a consequence, other less conservative forbidden regions or criteria have been proposed such as, energy sources analysis consortium (ESAC)

(Sudhoff et al., 2000), gain margin and phase margin (GMPM) (Wildrick et al., 1995), and opposing argument (X.Feng et al., 2002) criteria. The ESAC and GMPM regions are shown in Fig. 1.6 in addition to the Middlebrook's criterion. These regions are applied to provide load impedance specifications for certain source output impedance in order to guarantee stability (Wildrick et al., 1995). If the minor-loop gain does not overlap with the applied forbidden region, certain minimum GM and PM are guaranteed. A comprehensive survey of forbidden regions can be found in (Riccobono and Santi, 2012a; Zhang et al., 2004).

Common for all the discussed forbidden regions is that they all prevent the minor-loop gain from circling the point -1,0 in the complex plane. Another less restrictive criterion was applied in (Wildrick et al., 1995; X.Feng et al., 2002) for online stability margin monitoring for a system that is known to be stable. This region is discussed in detail in Chapter 2 and its origin and proper application are presented together with the concept of robust stability.

An alternative method to assess system small-signal stability is proposed in (Riccobono and Santi, 2012a,b) and it is based on assessing passivity of overall bus impedance of an interconnected system. However, as will be demonstrated in Chapter 2, this method is very conservative and it does not provide any indication of the stability margins.

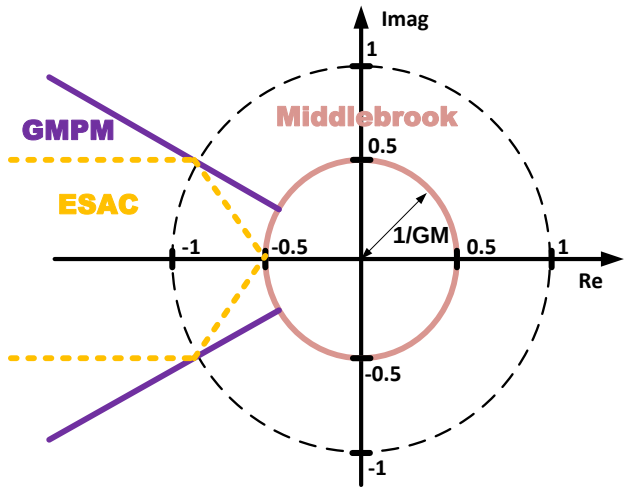

Fig. 1.6: Different forbidden regions on the complex plane (Sudhoff et al., 2000; Wildrick et al., 1995; X.Feng et al., 2002).

If the output impedance of the converter is altered (usually an increase in the magnitude) due to the impact of external impedances, the transient performance will be affected (Choi et al., 2005; Li and Lehman, 2005; Suntio et al., 2009; Wildrick et al.,

1995; Xing and Sun, 2012). Therefore, in order to guarantee the system stability as well as unaltered performance, reshaping of either the source or load impedances is required. In the case of cascade connection of a converter and an input filter, passive damping can be applied to reduce the peak output impedance of the filter (Middlebrook, 1976). However, depending on the application, different active damping methods exist to shape either the source or the load impedance (Rahimi and Emadi, 2009; Wand et al., 2014; Wang and Howe, 2009; Xing et al., 2011). In addition to shaping either of the impedances, in (Riccobono and Santi, 2012a,b) a method to design damping networks based on the passivity of the overall bus impedance to guarantee the stability of the interconnected system is introduced.

The small-signal stability analysis is operating point dependent, and therefore, valid only under certain condition whereas large-signal stability refers to analysis under large perturbations i.e. varying operating points. Different methods have been developed in order to assess the stability under changing operating points (B. Cho, 1990; D. Marx, 2008; Griffo et al., 2008; M. Belkhayat, 1995). However, the large-signal stability analysis lacks insight and is impractical due to circuit nonlinearity and system complexity (Sun, 2013). In addition, instability might occur due to some system features such as start-up, remote on-off or different protections (Oliver et al., 2009; Vesti et al., 2010). In order to include these features, behavioral converter models are required (Oliver et al., 2006; Prieto et al., 2009).

1.3 Converter modeling

There are various ways to model the dc-dc converters and different techniques can be used depending on the analysis purposes. The most utilized modeling method for dc-dc converters is averaging approach (Middlebrook and Cuk, 1976; Tse and di Bernardo, 2002). It results in simple non-linear models, which are then typically linearized around a certain operating point. This kind of modeling method is used for the design of the converter and the control-loop and typically information regarding the internal components and the applied topology is required.

As previously discussed, distributed systems often consist of commercial converters from various manufacturers. The system-level analysis becomes challenging due to unknown dynamics introduced by these converters. The manufacturers typically provide limited information on the internal structure of the converter, and therefore, the traditional modeling approaches are not applicable. In order to obtain models for commercial converters the following requirements need to be considered:

- Simple
- Black-box

- Obtainable through measurements or available information

In order to analyze the overall distributed system, the models need to be simple enough to allow the analysis of large systems consisting of various components. Even if detailed converter models are available, the simulations of large systems would become excessive. Therefore, trade-offs between the model accuracy, fast execution time and simplifications are necessary in order to obtain reasonable simulation times of large power architectures (Laguna et al., 2010, 2009).

Black-box approach refers to modeling a converter when its internal structure is unknown. Therefore, the models are required to be obtained based on the available information from the datasheet or by performing measurements (Arnedo et al., 2009; Bilberry et al., 2012; Cvetkovic et al., 2013; Prieto et al., 2009; Valdivia et al., 2010). Different structures such as Wiener-Hammerstein (Cvetkovic et al., 2013; Oliver et al., 2006; Prieto et al., 2009) or two-port (Arnedo et al., 2009; Bilberry et al., 2012; Valdivia et al., 2010) have been applied to obtain models for commercial converters for different purposes.

1.3.1 Two-port model

This section concentrates on introducing two-port model structure, which is utilized throughout this thesis for both commercial and custom designed converters. The identification of the parameters required for this model is discussed in detail as well, introducing methods to obtain the relevant parameters for this model.

The internal converter dynamics of any dc-dc converter, independent on the topology, applied control method or conduction mode, can be represented by means of a two-port network (Maranesi et al., 1988; Suntio, 2010). Therefore, it is suitable for modeling of commercial converters. The model consists of a set of transfer functions known as G-parameters for traditional voltage-input-voltage-output converter. However, depending on the terminal characteristics, different converter types can be equally characterized by this network applying a correct set of parameters (Leppaaho, 2008). The two-port network illustrated in Fig. 1.7 and given in (1.5) is constructed applying the traditional G-parameters.

$$\begin{aligned} \hat{i}_{\mathrm{in}} &= Y_{\mathrm{in}}\hat{u}_{\mathrm{in}} + T_{\mathrm{oi}}\hat{i}_{\mathrm{o}} \\ \hat{u}_{\mathrm{o}} &= G_{\mathrm{io}}\hat{u}_{\mathrm{in}} - Z_{\mathrm{o}}\hat{i}_{\mathrm{o}} \end{aligned} \tag{1.5}$$

This representation describes the closed-loop dynamics of the converter consisting of the following internal transfer functions:

- Audio susceptibility $G_{\mathrm{io}} = \hat{u}_{\mathrm{o}}/\hat{u}_{\mathrm{in}}|_{\hat{i}_{\mathrm{o}}=0}$

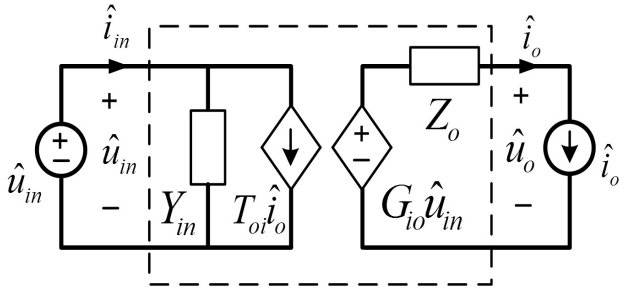

Fig. 1.7: Two-port structure of the converter with ideal source and load.

- Input admittance $Y_{\mathrm{in}} = \hat{i}_{\mathrm{in}}/\hat{u}_{\mathrm{in}}|_{\hat{i}_{\mathrm{o}}=0}$
- Reverse transfer function $T_{\mathrm{oi}} = \hat{i}_{\mathrm{in}}/\hat{i}_{\mathrm{o}}|_{\hat{u}_{\mathrm{in}}=0}$
- Output impedance $Z_{\mathrm{o}} = \hat{u}_{\mathrm{o}}/\hat{i}_{\mathrm{o}}|_{\hat{u}_{\mathrm{in}}=0}$

The two-port model is a linearized representation of the dc-dc converter, and therefore, the transfer functions are obtained at a single operating point. In case of a commercial power module these four transfer functions are measurable from the input and output terminals. Additionally, if the internal structure of the converter is known the transfer functions can be found analytically. The two-port model can be used to represent the open-loop dynamics by including additional input for the control signal, introducing two more transfer functions:

- Control-to-output $G_{\mathrm{co}} = \hat{u}_{\mathrm{o}}/\hat{d}|_{\hat{i}_{\mathrm{o}}=0,\hat{u}_{\mathrm{in}}=0}$
- Control-to-input $G_{\mathrm{ci}} = \hat{i}_{\mathrm{in}}/\hat{d}|_{\hat{i}_{\mathrm{o}}=0,\hat{u}_{\mathrm{in}}=0}$

In the analysis, the source and load are assumed ideal thus obtaining the internal dynamics of the converter. However, when the converter is interconnected to a real system, its dynamics can change due to the impedance-based interactions as previously discussed. These interactions can be analyzed based on this two-port model, deriving analytical equations to assess the influence of the source or the load side impedance to the internal transfer functions. This analysis methodology is discussed in detail in Chapter 2 and Chapter 3. The two-port network can be also used to represent input filters, both commercial (Hentunen et al., 2004) and design optimized (Hensgens et al., 2013), based on measurements and analytic expressions, respectively.

1.3.2 Parameter identification

The two-port structure is used as a basis for various dc-dc converter models intended for system-level simulations (Arnedo et al., 2009; Bilberry et al., 2012; Cvetkovic et al., 2013;

Valdivia et al., 2009, 2010). Common to the all models is that the internal parameters of the converter need to be identified. Different methods for obtaining the relevant dynamics have been proposed. In (Valdivia et al., 2009, 2010) the objective is to obtain large-signal behavioral models for system level simulations i.e. models that are valid under varying operating point. A time-domain based identification method is proposed, where the necessary transfer functions are identified by analyzing step responses performed either at the input or the output terminal of the converter. Parameter identification based on transient responses is also used in (Bilberry et al., 2012), where the transfer function descriptions are generated from the time-domain responses by processing the data with parameter estimation algorithm.

Frequency domain identification is the most straightforward method to obtain directly the required transfer functions without the need of post-processing the obtained data. Various manufacturers provide equipment to perform these measurements in a simple way. As an alternative to the commercial equipment, different low cost circuits have been proposed in order to obtain the necessary transfer functions (Arnedo et al., 2008; Fernandez-Herrero et al., 2012; Panovo and Jovanovic, 2005).

A typical measurement setup using commercially available equipment for measuring the input side transfer functions Y_{in} and G_{io} is illustrated in Fig. 1.8. Correspondingly, the setup for the output side parameters Z_{o} and T_{oi} is shown in Fig. 1.9.

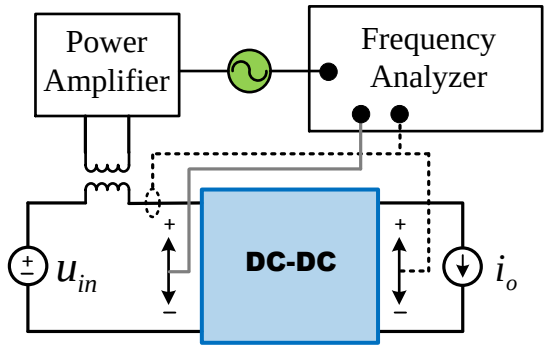

Fig. 1.8: Input side measurements (Y_{in}, and G_{io}).

The input-side transfer functions are obtained injecting a perturbation through the isolation transformer to the input voltage as illustrated in Fig. 1.8. In addition to measuring the perturbed input voltage, the input current measurement is required for the input admittance and the output voltage measurement is needed for the audiosusceptibility. Correspondingly, the output side transfer functions are obtained by injecting a perturbation at the output current through the isolation transformer, which is connected in parallel with the load as illustrated in Fig. 1.9. A dc blocking capacitor is connected in

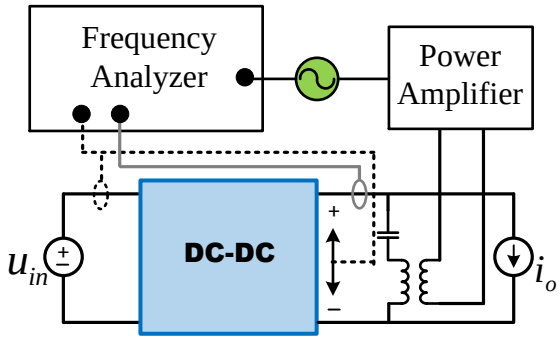

Fig. 1.9: Output side measurements (Z_o, and T_{oi}).

series with the transformer in order to avoid the dc current from circulating. In addition to measuring the perturbed output current, the output voltage is required for the output impedance and the input current for the reverse transfer function, as illustrated in the figure.

As previously discussed, the identified transfer functions are valid at a certain operating point. In (Cvetkovic et al., 2013), the two-port structure is used as a basis for modular black box models, which are valid under a range of operating points. Therefore, the four transfer functions are measured at various operating points in order to capture the changes in the dynamic behavior when the operating condition alters. The required parameters for the two-port model can be also represented analytically using circuit elements. However, the analytical method is valid only when the internal parameters, topology as well as the control method are known.

In this thesis, the required parameters for the two-port model for commercial converters are obtained based on the frequency domain measurements. All measurements are obtained using Venable Industries' frequency response analyzer model 3120 with an impedance measurement kit. The measurement setup is shown in Appendix A. For more detailed control-method-dependant interactions analysis, analytical models based on the circuit parameters are needed as will be presented in Chapter 3.

1.4 Motivation of the thesis

The analysis and design of dc-distributed power systems can be very challenging due to complex architecture structure and interactions that are a consequence of the system integration. Therefore, the overall motivation for this thesis is to facilitate the design and analysis of the dc-distributed systems consisting of commercial converters.

1.4.1 System optimization

The amount of available dc-dc converters from various manufacturers is large and the selection of proper converter modules and their connections to form system architecture can be a complex and time-consuming task. In order to comply with various system specifications as well as to meet the different load requirements, the architecture of the distributed system can be extremely complicated (D.Boroyevic et al., 2010). Fig. 1.10 illustrates supply requirements of a power system architecture for a wireless sensor network application, where the architecture block represents a distributed system that supplies the loads according to their needs from the source voltage. Therefore, the optimization of the power architectures is a complex problem due to the plethora of different ways to connect various system components.

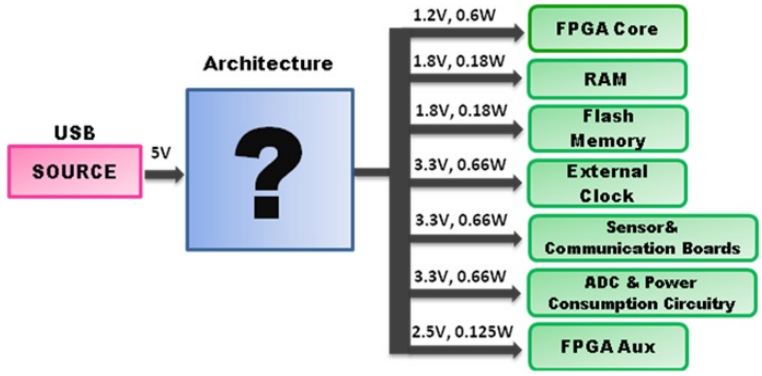

Fig. 1.10: Example of a distributed system architecture for application of a wireless sensor network node.

To facilitate the architecture optimization problem, a methodology is developed to design and optimize power architectures in terms of the most fundamental system features: size, cost and efficiency. It is based on complex optimization algorithms (Laguna et al., 2010), and therefore, in order to analyze large number of design options, simplified converter models considering only the static features are utilized (Oliver et al., 2009; Prieto et al., 2009). These simple models enable fast analysis of various architectural solutions and based on these models, an architecture generation algorithm searches all suitable ways to connect these components according to the system specifications. The optimization process selects the most appropriate converters and provides a list of architectural solutions including options with the smallest size, cost and losses as well as the best trade-offs within these features.

The overall optimization methodology assists the design of distributed power systems as multiple options can be assessed in a short time and the best architecture solution for

a specific system application can be selected. However, during the process various features are neglected regarding the dc-dc converters: the optimized solutions are obtained without considering the stability and the dynamic performance of the converters.

As previously discussed, adverse interactions might occur due to the converter sensitivity to the external impedances possibly leading to degraded converter transient performance or even instability. Therefore, it is obvious that the converters cannot be merely cascaded to form system architecture without considering the interactions. Thus the stability of the obtained optimized architectural solutions needs to be assessed. In addition, it is of interest to be able to compare different architectural solutions in terms of robust stability for the selection of the proper structure for the system.

1.4.2 Dynamic representation of commercial converter

Practical distributed systems consist of multiple commercial converters which are designed guaranteeing specific standalone performance. The available information in the datasheet varies depending on the manufacturer (TexasInstruments, 2000; Tracopower, 2009) and is typically rather limited. Therefore, the commercial converters introduce unknown dynamics to the system. This complicates the overall design of the distributed systems since the converters are expected to work in a real system without degradations in the performance.

Each converter has specific internal dynamics, which are determined by the circuit elements as well as the applied control method. This dynamic profile defines the converter sensitivity to the external impedances. Comprehensive dynamical analysis regarding different control methods and their influence on the open-loop dynamics of the converter are presented in (Hankaniemi et al., 2006a,b,c; Karppanen et al., 2007a,b; Suntio et al., 2009) with the objective to provide recommendations for a converter which is highly invariant to source and load interactions. However, the analysis concentrated on the assessment of a custom designed converter utilizing analytical expressions based on circuit parameters.

In the case of commercial converters, only four transfer functions are measurable from the input and output terminals. Therefore, the stability and performance analysis need to be based on that information. Complete description of both source and load-side interactions parameters is still missing and the set of equations describing the interactions sensitivity is incomplete especially with the objective of applying the analysis to commercial converters.

1.5 Structure of the thesis

The main content of this thesis is divided into the following three parts:

- Robust stability analysis
- Detailed interactions analysis
- System stability analysis and metrics

The first part is covered in Chapter 2. It concentrates on defining the least conservative margins for the small-signal stability. In addition, the concept of robust stability and its application in practice is explained in detail. The second part is discussed in Chapter 3. It focuses on detailed impedance-based interactions within the system due to the internal converter dynamics. The converter control method influence on the interactions is discussed providing comprehensive formulas to assess the source and load-side interactions. Chapter 4 discusses the third part, where the presented concept for the robust stability is applied for a practical system introducing performance metrics to state the overall system stability. Finally, Chapter 5 concludes the thesis and proposes future research topics.

1.6 Objectives

The main purpose of this thesis is to contribute to the development of analysis methodologies and tools to facilitate the overall design and selection of proper dc-distributed system architecture. The research questions are stated as follows:

- How to guarantee robust stability?
- How to define the dynamics and performance of a dc-distributed system consisting of commercial converters?
- How to systematically assess the small-signal stability of a distributed system and compare different architectures in terms of stability?

Thus based on these questions regarding the dc-distributed system consisting of commercial modules, the main objectives for this thesis can be summarized as:

- Obtaining a methodology to assess complex interactions of a dc-distributed system without knowing the detailed inner properties of the utilized dc-dc converters.
- Stating the stability of a given system architecture and comparing different architectural structures in terms of robust stability.

1.6.1 Main contributions

The main contributions of this thesis can be divided into scientific and industrial. The main scientific contributions are summarized as:

- It is shown that based on frequency response measurements, the stability and performance of a commercial-power-module-based system can be predicted and analyzed. The converter sensitivity to external interactions depends on the internal dynamics and is best assessed according to impedance-type special parameters.
- It is shown that in order to correctly predict the robust stability within an interconnected system, the minor-loop gain is to be determined at the very input or output terminal of the converter. The origin of the MPC-based forbidden region is provided.
- Systematic small-signal stability analysis of a given system structure is proposed introducing a performance metrics to determine the overall system stability enabling the comparison of various architecture solutions in terms of robust stability.

In addition, the results of this thesis have been applied in the following industrial projects:

- Design and analysis of dc-distributed power systems for avionic application based on simulations using behavioral dc-dc converter models, funded by Indra.
- Fast equivalent models for the management of efficient electronic networks, funded by Ministerio de Ciencia e Innovacion of Spain through the project (MOREGREEN) Modelos Rapidos Equivalentes para Gestion de Redes Electronicas de Energia (DPI2010-17466).
- Optimization tool for the design of distributed power architectures.

1.6.2 Publications

The following papers are published within the topic area which are mainly contributed by the author.

[P1] Vesti, S., Suntio, T., Oliver, J.A., Prieto, R., and Cobos, J.A. (2013). "Impedance-based stability and transient-performance assessment applying maximum peak criteria," in *IEEE Trans. Power Electron.*, Vol. 28, No. 5, pp. 2099–2104.

[P2] Vesti, S., Suntio, T., Oliver, J.A., Prieto, R., and Cobos, J.A. (2013). "Effect of control method on impedance-based interactions in a buck converter," in *IEEE Trans. Power Electron.*, Vol. 28, No. 5, pp. 5311–5322.

[P3] Vesti, S., Oliver, J.A., Prieto, R., Cobos, J.A., and Suntio, T. (2013). "Simplified small-signal stability analysis for optimized power system architecture," in *Proc. IEEE APEC*, pp. 1702–1708.

[P4] Vesti, S., Oliver, J.A., Prieto, R., Cobos, J.A., and Suntio, T. (2013). "Performance metrics for small-signal stability assessment of dc-distributed power-system-architecture comparisons," in *Proc. IEEE ECCE*, pp. 5403–5409.

[P5] Vesti, S., Oliver, J.A., Prieto, R., Cobos, J.A., Huusari, J., and Suntio, T. (2012). "Practical characterization of input-parallel-connected converters with a common input filter," in *Proc. IEEE APEC*, pp. 1845–1852.

[P6] Vesti, S., Oliver, J.A., Prieto, R., Cobos, J.A., and Suntio, T. (2011)."Stability and transient performance assessment in a COTS-module-based distributed DC/DC system," *Proc. IEEE IINTELEC*, pp. 1–9.

[P7] Vesti, S., Alou, P., Oliver, J.A., Garcia, O., Prieto R., and, Cobos, J.A.,(2010). "Modeling and simulation of a distributed power system for avionic application," in *Proc. IEEE ECCE*, pp. 4421–4427.

2 ROBUST STABILITY

In this chapter, the original contribution is to provide the least conservative stability margins as a single number for the minor-loop gain, guaranteeing robust stability. The presented methodology provides information, whether the internal converter dynamics is altered due to the system interconnection. Furthermore, it is shown that the robustness of stability can be determined most reliably at the input and output terminals of the converter and that the validity of the extractable robustness information regarding the minor-loop gain is interface-dependent. In addition, explicit revelation of the basis for the least conservative forbidden region based on maximum peak criteria (MPC) is provided.

The passivity-based stability analysis method is first discussed in more detail as an alternative method to provide information regarding the small-signal stability. Theoretical background for source and load-affected converter dynamics is presented, as well as the practical frequency domain characterization. Thereafter, the concept of maximum peak criteria is introduced, describing how to obtain the least conservative stability margins for a minor-loop gain guaranteeing robust stability. Both commercial and prototype converters as well as simulations are used for the analysis in order to demonstrate the presented concepts.

2.1 Introduction

Traditionally the small-signal stability of two interconnected subsystems is assessed based on the minor-loop gain, as discussed in the previous chapter. An alternative method is passivity-based stability criterion (PBSC) (Riccobono and Santi, 2012a,b). It is based on analyzing the passivity of a bus impedance, which is a parallel connection of the input and the output impedances in the interconnected subsystems. The PBSC concept provides a different way to state the stability, eliminating the necessity of analyzing the encirclement of the point (-1,0) in the complex plane. If passivity is satisfied for the total bus impedance, the system is stable. The conditions for passivity (Riccobono and Santi, 2012a,b) are:

- No RHP poles in Z_{bus}
- $\text{Re}\{Z_{\text{bus}}(j\omega)\} \geq 0$

The Nyquist contour of the bus impedance is required to lie wholly on the right half of the complex plane (RHP). Thus the real part of the bus impedance is required to be always positive, referring that the phase is always between ± 90°. The PBSC provides a sufficient condition for stating the stability. However, unlike the Nyquist criterion it is not a necessary condition for stability, and therefore, the application of this concept in a general stability analysis might lead to a conservative design and thus discarding a valid solution. This is illustrated by the following example of cascaded converters in Fig. 2.1: Converter A is a designed voltage-mode-controlled synchronous buck converter ($U_{\text{in}} = 12\text{V}$, $U_{\text{o}} = 5\text{V}$, $I_{\text{o}} = 0.5\text{A}$, $f_{\text{sw}} = 200\text{kHz}$) and Converter B operates as a constant power load (R = -10Ω, $C_{\text{in}} = 17\mu\text{F}$). The bus impedance of this interconnected system is defined in (2.1).

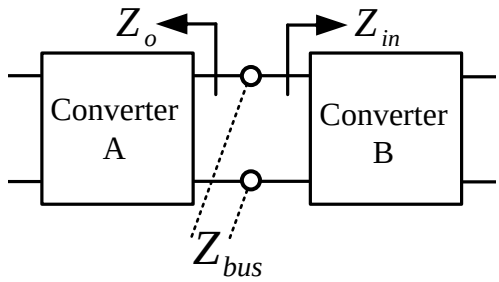

Fig. 2.1: The bus impedance of two cascaded converters.

$$Z_{\text{bus}} = Z_{\text{in}} \parallel Z_{\text{o}} = \frac{Z_{\text{o}}}{1 + Z_{\text{o}}/Z_{\text{in}}} \tag{2.1}$$

The measured output impedance of Converter A (solid line) and the simulated input impedance (dashed line) of the Converter B are shown in Fig. 2.2. It can be observed that $Z_{\text{o}} \ll Z_{\text{in}}$ almost throughout the whole frequency range, and therefore, the bus impedance is equivalent to the output impedance of the buck converter. Based on the measured output impedance, it can be observed that the phase exceeds 90° approximately at 200Hz. This phase behavior is typical for voltage-mode controlled buck converter. The stability analysis for this cascaded connection is then performed by analyzing the passivity of the bus impedance (solid line) as well as applying the traditional minor-loop gain (dashed line) as shown in the complex plane in Fig. 2.3.

According to the PBSC, the bus impedance is not passive, because its Nyquist contour does not fully lie on the RHP. Therefore, the information provided by the passivity-based criterion regarding the system stability is unclear and consequently a valid solution might be discarded. Whereas utilizing the traditional stability assessment methods, the system

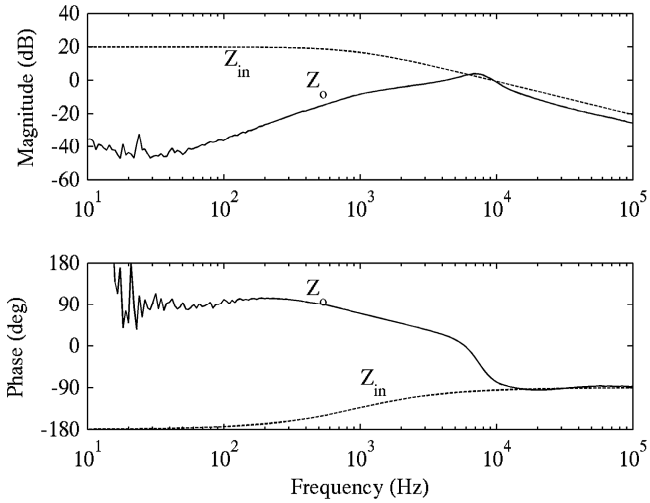

Fig. 2.2: Measured output impedance (Z_{o}), solid line, of a synchronous buck converter and simulated input impedance (Z_{in}), dashed line, of a cascaded connected converter.

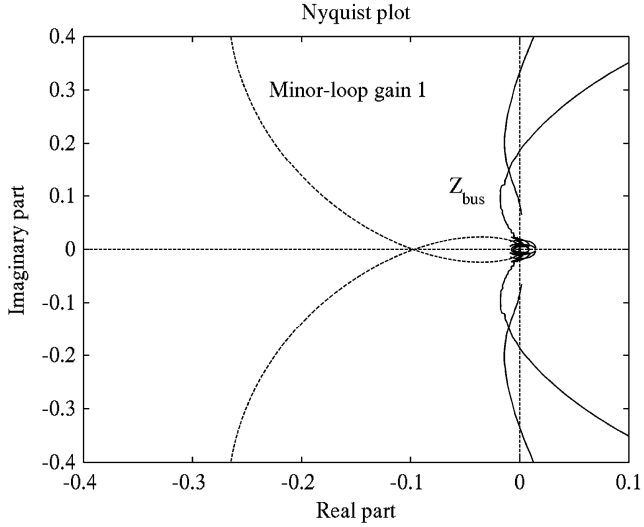

Fig. 2.3: Nyquist contour of the bus impedance, solid line, and the minor-loop gain, dashed line.

is stable with good gain and phase margins. Therefore, PBSC is a poor method for general small-signal stability analysis of distributed systems. It is mainly used in applications where active damping is applied to shape the converter impedance based on the passivity information and thus guaranteeing the stability (Riccobono and Santi, 2012a,b). In this thesis, only the minor-loop gain based stability assessment method is utilized.

2.2 System modeling

Proper modeling of the commercial converters is essential in order to predict the robust stability and performance of the distributed systems. For the system small-signal stability assessment, the two-port model described in Chapter 1 is applied to analyze the interactions. The analytical formulation to assess the source and load-side impedance influence to the converter dynamics is presented focusing on the small-signal stability whereas the detailed interactions analysis is presented in Chapter 3.

2.2.1 Source and load-affected system

A converter with interconnected source and load is illustrated in Fig. 2.4, where the Z_s refers to the source and Z_L to the load impedance as well as Z_in^c and Z_o^c are the input and output impedances of the converter that is analyzed. This interconnected system can be represented as a two-port structure, shown in Fig. 2.5 where the source is represented as its output impedance Z_s and the load as its input admittance Y_L. The influence of these external impedances to the converter dynamics (inside the dashed line) can be analytically obtained. This model represents the dynamics of a closed-loop converter, i.e. a commercial converter, but the same model representation can be used for open-loop dynamics by including the control variable as an additional input to the system, as will be discussed in detail in Chapter 3.

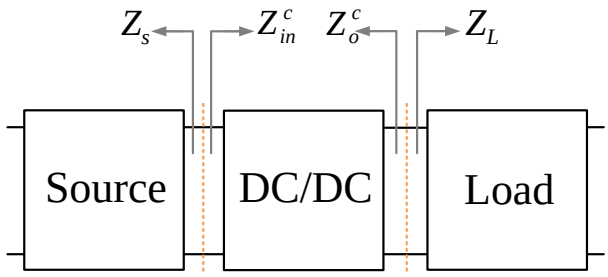

Fig. 2.4: Interconnected system with source and load-side impedances.

The source-side impedance influence can be obtained by representing the input voltage as given in (2.2) and including the source impedance Z_s as a part of the converter dynamics.

$$\hat{u}_\mathrm{in} = \hat{u}_\mathrm{ins} - Z_\mathrm{s}\hat{i}_\mathrm{in} \tag{2.2}$$

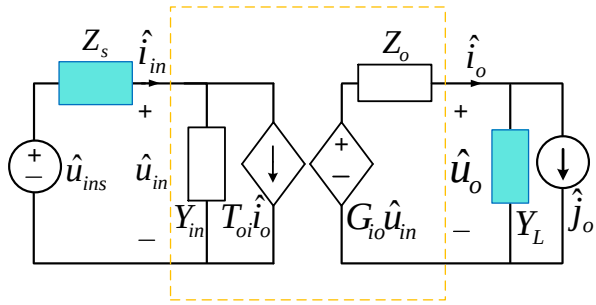

Fig. 2.5: Internal converter dynamics including the source- and load side impedances.

By replacing this input voltage representation to the original set of equations (1.5) provided in the previous chapter, the source-affected dynamics are obtained as given in (2.3). The implicit parameter $Y_{\text{in-sco}}$ is a short-circuit input admittance, defined in (2.4). It is dependent on the applied control method and its detailed application on the interactions analysis is discussed in Chapter 3.

$$\begin{aligned}\hat{i}_{\text{in}} &= \frac{Y_{\text{in}}}{1+Z_{\text{s}}Y_{\text{in}}}\hat{u}_{\text{ins}} + \frac{T_{\text{oi}}}{1+Z_{\text{s}}Y_{\text{in}}}\hat{i}_{\text{o}} \\ \hat{u}_{\text{o}} &= \frac{G_{\text{io}}}{1+Z_{\text{s}}Y_{\text{in}}}\hat{u}_{\text{ins}} - \frac{1+Z_{\text{s}}Y_{\text{in-sco}}}{1+Z_{\text{s}}Y_{\text{in}}}Z_{\text{o}}\hat{i}_{\text{o}}\end{aligned} \tag{2.3}$$

$$Y_{\text{in-sco}} = Y_{\text{in}} + \frac{G_{\text{io}}T_{\text{oi}}}{Z_{\text{o}}} \tag{2.4}$$

In a similar way, the load impedance influence can be assessed by including the load admittance Y_{L} as a part of the converter dynamics, representing the output current as (2.5). The corresponding load-affected equations are given in (2.6) and the implicit parameter $Z_{\text{o-oci}}$ is the open-circuit output impedance, defined in (2.7). Its detailed meaning for interactions analysis is discussed in the following chapter. The source and load-side minor-loop gains in (2.3) and (2.6) are $Z_{\text{s}}Y_{\text{in}}$ and $Z_{\text{o}}Y_{\text{L}}$, respectively. It can be observed that stability of the original transfer functions depends on the minor-loop gains and can be assessed applying the Nyquist stability criterion.

$$\hat{i}_{\text{o}} = \hat{j}_{\text{o}} + Y_{\text{L}}\hat{u}_{\text{o}} \tag{2.5}$$

$$\begin{aligned}\hat{i}_{\text{in}} &= \frac{1+Z_{\text{o-oci}}Y_{\text{L}}}{1+Z_{\text{o}}Y_{\text{L}}}Y_{\text{in}}\hat{u}_{\text{in}} + \frac{T_{\text{oi}}}{1+Z_{\text{o}}Y_{\text{L}}}\hat{j}_{\text{o}} \\ \hat{u}_{\text{o}} &= \frac{G_{\text{io}}}{1+Z_{\text{o}}Y_{\text{L}}}\hat{u}_{\text{in}} - \frac{1+Z_{\text{o}}}{1+Z_{\text{o}}Y_{\text{L}}}\hat{j}_{\text{o}}\end{aligned} \tag{2.6}$$

$$Z_{\text{o-oci}} = Z_{\text{o}} + \frac{G_{\text{io}}T_{\text{oi}}}{Y_{\text{in}}} \tag{2.7}$$

2.2.2 Converter characterization

The small-signal stability of an interconnected system is assessed based on the impedance ratio. These impedances need to be identified at a correct operating point in order to analyze of an actual system consisting of commercial components. Different parameter identification methods were reviewed in the first chapter but in this thesis the converters are solely characterized based on the frequency domain measurements.

The transfer functions utilized in the theoretical analysis are assumed unterminated, i.e. independent of the source and load dynamics. Therefore, while performing the frequency response measurements neither the source nor the load should couple with the internal converter dynamics. Two examples to demonstrate the practical characterization of commercial converters are provided:

- Commercial POL converter PT78ST100 (TexasInstruments, 2000)
- Commercial bus converter evaluation board IB048E120T40N1 (Vicor, 2013)

The four transfer functions of the POL converter are measured at the operating point: $U_{\text{in}} = 12\text{V}$, $U_{\text{o}} = 5\text{V}$, $I_{\text{o}} = 1.5\text{A}$, showing input ($Z_{\text{in}}$) and output ($Z_{\text{o}}$) impedances in Fig. 2.6 and the audiosusceptibility (G_{io}) as well as the reverse transfer function (T_{oi}) in Fig. 2.7. These transfer functions are well-behaving, i.e. no unintentional resonance peaks are observable.

The second characterization example demonstrates the source-side couplings. The measurements are performed with an evaluation board, shown in Fig. 2.8. The board contains a dc-dc converter, a discrete LC-filter as well as additional connectors and other components. The converter output impedance is first measured by connecting the source and load to the input and output connectors of the evaluation board, illustrated in Fig. 2.8 with number '1'. The same measurement is then repeated at the direct input and output terminals of the converter, indicated as number '2', removing or disconnecting the additional components. The measured output impedances Z_{o1}, obtained from the first measurement point, and Z_{o2} at the second measurement point are shown in Fig. 2.9.

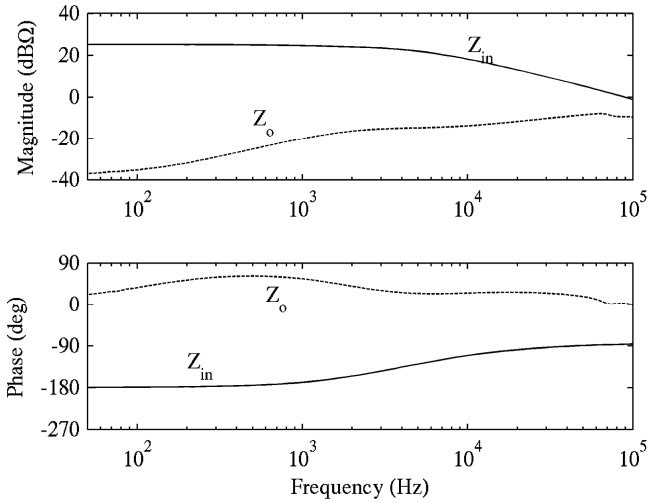

Fig. 2.6: Characterized input and output impedances of the commercial converter.

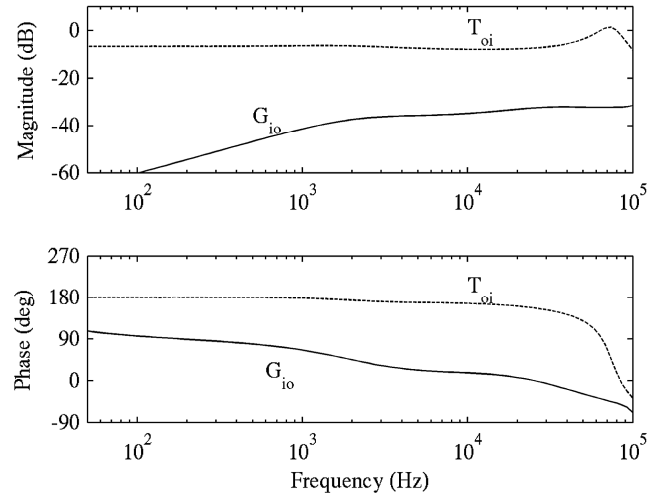

Fig. 2.7: Measured audiosusceptibility and reverse transfer function of the commercial converter.

Based on the measured output impedances, the source-side coupling is clearly observable from the first output impedance Z_{o1} as a comparison to Z_{o2}, where the additional source-side impedance is removed. Therefore, in order to characterize the internal converter dynamics, the measurements should be performed at the direct input and output terminals of the converter removing all additional components, which are not part of the converter power stage. However, in case it is of interest to observe how a certain

Fig. 2.8: Different measurement points on the evaluation board of a commercial converter (Vicor, 2013)

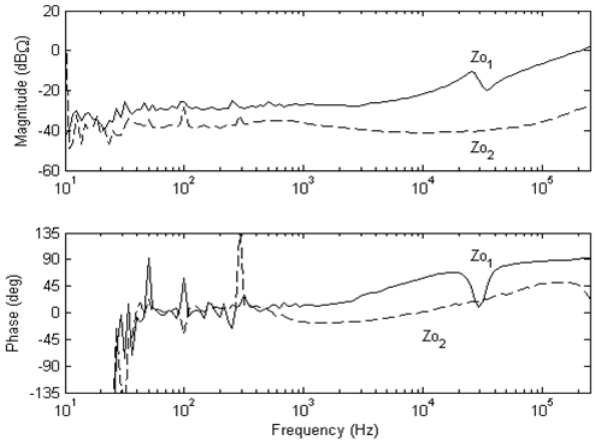

Fig. 2.9: Measured Z_{o1} and Z_{o2} obtained at measurement points one and two, respectively.

input filter might alter the converter dynamics, according to (2.3), the internal transfer functions can be measured together with a discrete filter.

2.3 Least conservative margins for stability

In control engineering, robust stability refers to a system that is stable under certain parameter variations. In order to ensure it, a concept of maximum peak criteria (MPC) is used in the design of feedback systems (Skogestad and Postlethwaite, 2001). This concept is also applicable in the analysis of distributed systems to state the robustness of stability for a well-defined minor-loop gain (Vesti et al., 2013b).

While integrating the system, it is of interest to know whether two components can be cascaded, guaranteeing stability and unaltered performance. However, since one of the main design objectives of distributed systems is to optimize the size, it is of interest to obtain the minimum stability margins, to avoid conservative designs. The concept of sensitivity function and its application on extracting the stability margins is provided in the following section, as well as the origin for the least conservative circular forbidden area.

2.3.1 Maximum peak criteria

Maximum peak criteria (MPC) is a well-known method to state robust stability of a closed-loop system (Skogestad and Postlethwaite, 2001). It is based on the frequency domain analysis of the maximum peak values of the sensitivity (S) and the complementary sensitivity (T) functions, defined in (2.8), where L is the loop-gain, i.e. transfer function around the loop as seen from the output.

A dc-dc converter is a closed loop-system and its output voltage can be represented as in (2.9) (Erickson and Maksimovic, 2001), where $\hat{c}$ represents the general control variable of the system and G_{se} is the sensor gain. The transfer functions representing the internal dynamics are indicated by subscript extension "-o" which indicates open-loop. This output voltage expression illustrates how the sensitivity and complementary sensitivity, defined in (2.8), are related to the closed-loop dynamics of a dc-dc converter.

$$\begin{aligned} S &= \frac{1}{1+L} \\ T &= \frac{L}{1+L} \end{aligned} \tag{2.8}$$

$$\hat{u}_{\text{o}} = \frac{G_{\text{io-o}}}{1+L}\hat{u}_{\text{in}} - \frac{Z_{\text{o-o}}}{1+L}\hat{i}_{\text{o}} + \frac{L}{G_{\text{se}}(1+L)}\hat{c} \tag{2.9}$$

The loop gain L is typically designed guaranteeing certain gain and phase margins to provide appropriate trade-off between closed-loop performance and stability. These

margins are illustrated in Fig. 2.10 in the complex plane and defined in (2.10) (Skogestad and Postlethwaite, 2001). The phase crossover frequency ω_{180} for the gain margin is the point where the Nyquist contour of the loop gain crosses the negative real axes. Correspondingly for the phase margin, the gain crossover frequency ω_c is defined as the point, where the loop gain first crosses the unity circle.

$$\begin{aligned} GM &= \frac{1}{L(j\omega_{180})} \\ PM &= \angle L(j\omega_c) + 180^\circ \end{aligned} \tag{2.10}$$

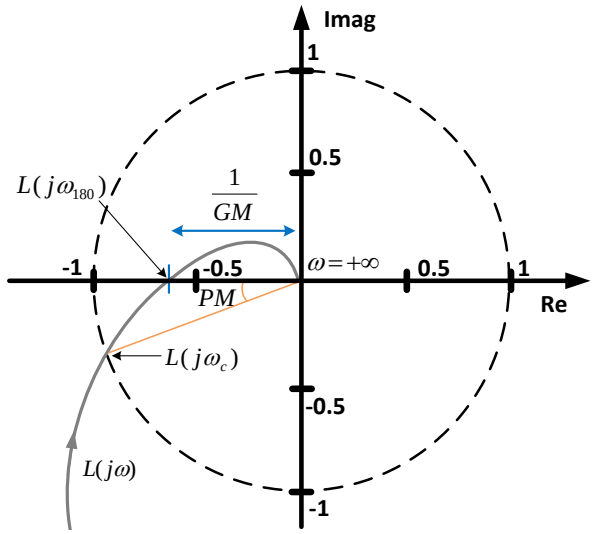

Fig. 2.10: . Nyquist plot of a loop gain L(jω), indicating PM and GM.

The robustness of stability, however, is determined by the critical area in the vicinity of the point (-1,0), (Basso, 2012; Skogestad and Postlethwaite, 2001). Therefore, the closed-loop performance is best assessed according to the closeness of the loop gain L($j\omega$) to the critical point (-1,0). This distance is illustrated as 'x' in Fig. 2.11 and throughout the frequency range it is given as (2.11) (Basso, 2012).

$$x = |1 + L(j\omega)| \tag{2.11}$$

From this expression, it can be observed that the distance 'x' is the inverse of the

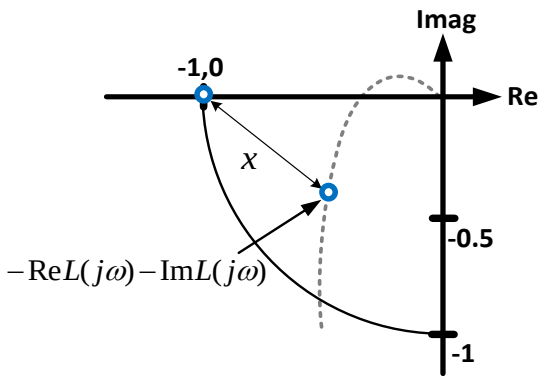

Fig. 2.11: Distance 'x', between the loop gain and the critical point -1 on a complex plane (Basso, 2012).

sensitivity function (2.8), and therefore, this distance has its critical minimum value when the sensitivity function is the highest. Thus the maximum value of the sensitivity function, $S_{\max}$, can be utilized as a robustness measure for the loop-gain. Large peak value indicates poor closed-loop performance and robustness. In control engineering, the recommendation is to have $S_{\max}$ less than 2 (6dB), whereas a value larger than 4 (12dB) refers to poor robustness. According to the maximum peak of the sensitivity function, corresponding gain (GM_{MPC}) and phase (PM_{MPC}) margins to guarantee robustness can be obtained as defined in (2.12) (Skogestad and Postlethwaite, 2001).

$$\begin{aligned} PM_{\text{MPC}} &\geq 2arcsin(\frac{1}{2|S_{\max}|}) \\ GM_{\text{MPC}} &\geq \frac{1}{1-1/S_{\max}} \end{aligned} \tag{2.12}$$

Even if the traditional gain and phase margins (2.10) illustrated in Fig. 2.10, would guarantee stability, the performance might be jeopardized because these margins will not ensure robustness (Aström and Murray, 2008; Skogestad and Postlethwaite, 2001). This is illustrated by a following analytical example of a closed-loop system with a loop-gain as (2.13) according to (Aström and Murray, 2008).

$$L(s) = \frac{0.38(s^2+0.1s+0.55)}{s(s+1)(s^2+0.06s+0.5)} \tag{2.13}$$

Traditional stability analysis of this loop-gain would provide a phase margin of approximately 70° as can be seen from the Nyquist diagram in Fig. 2.12. However, the computed phase margin according to the minimum distance of the loop-gain and the critical point (-1,0) results 17° implying performance degradation.

The inability of the Bode-plot-based analysis to guarantee robust stability of a closed-loop dc-dc converter is also observed in practice (Basso, 2012; Sandler, 2014; Sandler et al., 2012). Therefore, the closeness of the loop gain and the point (-1,0) in the complex plane provides proper method to assess the robustness of a closed-loop system and should be considered while designing the feedback for the dc-dc converters.

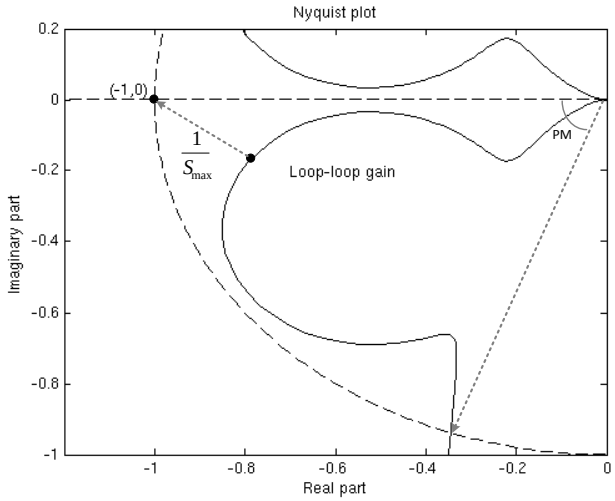

Fig. 2.12: Loop-gain with good traditionally defined gain and phase margins, but poor robustness (Aström and Murray, 2008)

2.3.2 Minor-loop gain based sensitivity function

The MPC concept can be also applied in the analysis of distributed systems to provide margins for robust stability (Vesti et al., 2013b; Vestii et al., 2013). The influence of the interconnected system to the converter dynamics was provided in (2.3) for the source-side and in (2.6) for the load-side interactions. Based on these equations it can be observed that the minor-loop gains, $Y_{\mathrm{in}}Z_{\mathrm{s}}$ for the source-side or $Z_{\mathrm{o}}Y_{\mathrm{L}}$ for the load-side, form a similar sensitivity function, S (2.14), as the loop gain L in (2.8).

$$S = \frac{1}{1 + ML} \tag{2.14}$$

A large peak value of this sensitivity function would cause peaking in the internal transfer functions. This influence can be observed analytically by expressing the source- and load-affected converter dynamics of (2.3) and (2.6) as (2.15) and (2.16), respectively. All internal transfer functions are influenced by the sensitivity function. However, in the case of the output impedance in (2.15) and the input admittance in (2.16), two control-method-dependent parameters influence additionally on these transfer functions.

$$\begin{aligned}\hat{i}_{\mathrm{in}} &= SY_{\mathrm{in}}\hat{u}_{\mathrm{in}} + ST_{\mathrm{oi}}\hat{i}_{\mathrm{o}} \\ \hat{u}_{\mathrm{o}} &= SG_{\mathrm{io}}\hat{u}_{\mathrm{in}} - S(1 + Z_{\mathrm{s}}Y_{\text{in-sco}})Z_{\mathrm{o}}\hat{i}_{\mathrm{o}}\end{aligned} \tag{2.15}$$

$$\begin{aligned}\hat{i}_{\mathrm{in}} &= S(1 + Z_{\text{o-oci}}Y_{\mathrm{L}})Y_{\mathrm{in}}\hat{u}_{\mathrm{in}} + ST_{\mathrm{oi}}\hat{i}_{\mathrm{o}} \\ \hat{u}_{\mathrm{o}} &= SG_{\mathrm{io}}\hat{u}_{\mathrm{in}} - SZ_{\mathrm{o}}\hat{i}_{\mathrm{o}}\end{aligned} \tag{2.16}$$

The influence of high source-side $S_{\max}$ to the converter dynamics (2.15) is demonstrated in practice for an interconnected system shown in Fig. 2.13, where the commercial converter (TexasInstruments, 2000) is operating at 1A load.

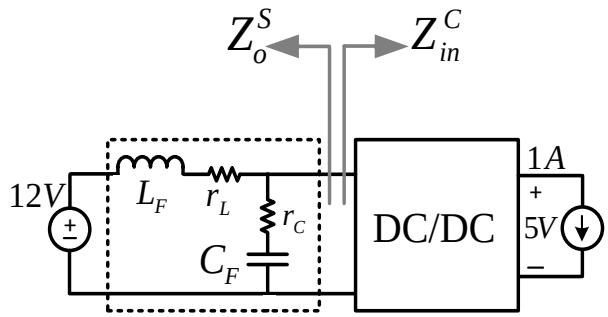

Fig. 2.13: Interconnected input filter and a commercial dc-dc converter.

The input filter is designed so that its output impedance is high enough in order to obtain a large peak value in the source-side sensitivity function, however, guaranteeing the stability. Therefore, the values for the filter components are chosen as $L_{\mathrm{F}} = 400\mu\mathrm{H}$, $C_{\mathrm{F}} = 100\mu\mathrm{F}$, $r_{\mathrm{L}} = 80\mathrm{m}\Omega$, $r_{\mathrm{C}} = 100\mathrm{m}\Omega$. The measured input impedance of the converter, $Z_{\text{in-c}}$, as well as the simulated filter output impedance, $Z_{\text{o-s}}$, are shown in Fig. 2.14 and the corresponding minor-loop gain is illustrated in the complex plane in Fig. 2.15. It can be observed that the minimum distance between the minor-loop gain and the point (-1,0) in the complex plane is small, and therefore, the corresponding sensitivity function has

a high peak value of approximately 14dB as shown in Fig. 2.16.

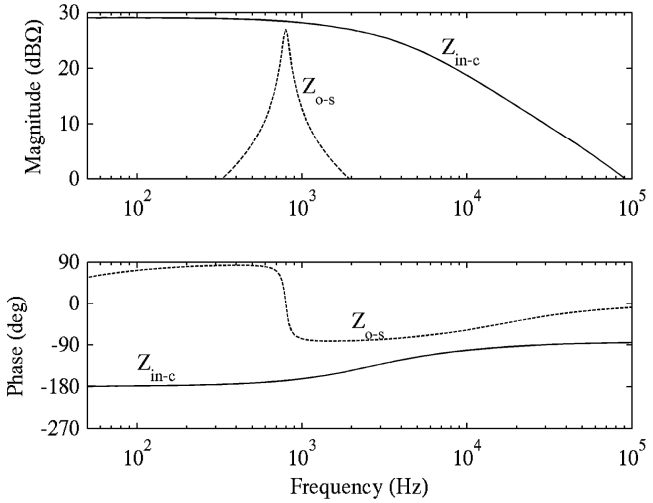

Fig. 2.14: Measured input impedance of a commercial dc-dc converter and simulated output impedance of an input filter.

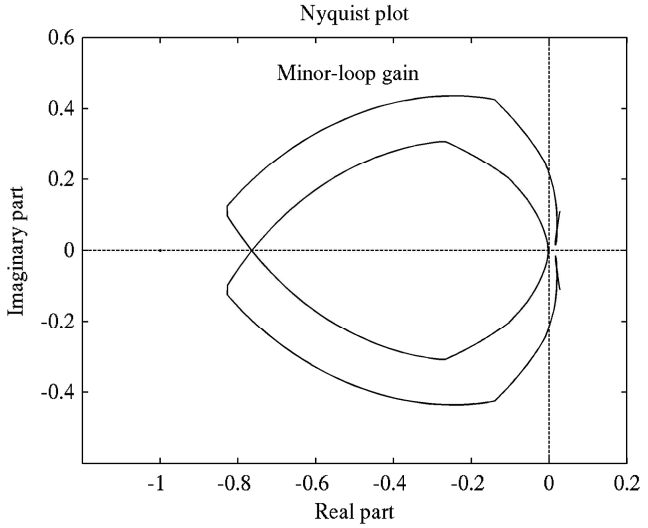

Fig. 2.15: Nyquist contour of the source-side minor-loop gain.

This peaking in the source-side sensitivity function alters all the converter dynamics according to (2.15) where the transfer functions, except the output impedance, are multiplied directly by the sensitivity function. The source impedance influence to the level

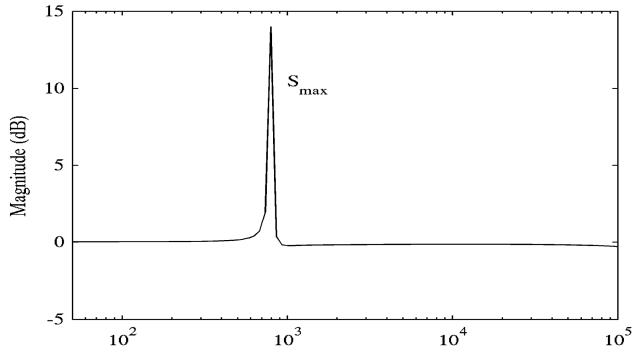

Fig. 2.16: Frequency domain plot of the sensitivity function.

of degradation in the converter output impedance depends on $Y_{\text{in-sco}}$ (2.4), which is a control-method-dependent parameter as will be discussed in more detail in Chapter 3.

The source-affected transfer functions are computed based on the measurements and are shown in Figs. 2.17- 2.20 together with the original transfer functions. It can be observed that the converter dynamics is significantly altered due to the high peak in the sensitivity function. Altered converter dynamics might degrade the converter performance or even cause instability. The output voltage transient response is typically the most important performance specification in time-domain and the deviation in the output voltage due to a load step can be approximated as in (2.17).

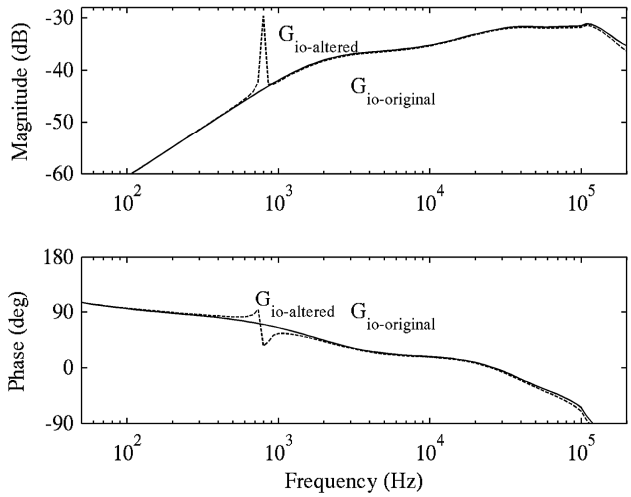

Fig. 2.17: Original and source-affected audiosusceptibility.

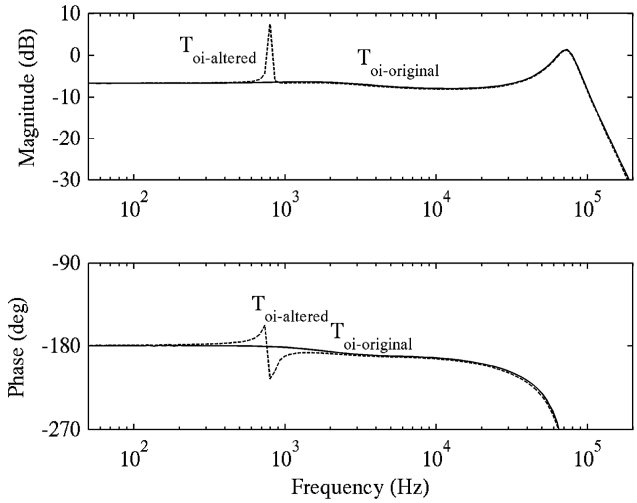

Fig. 2.18: Original and source-affected reverse transfer function.

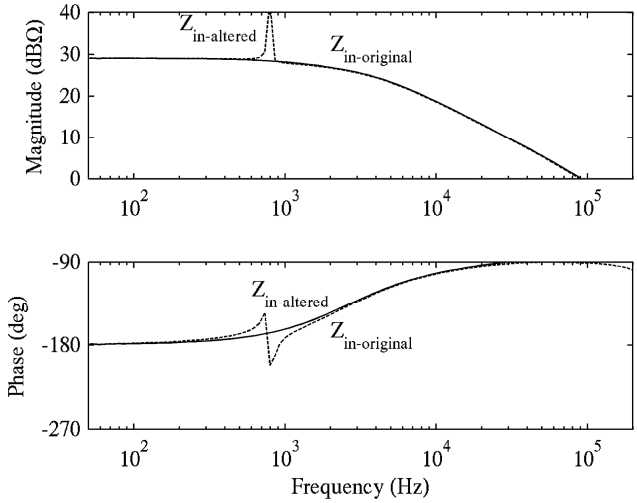

Fig. 2.19: Original and source-affected input impedance.

$$\triangle v_{\mathrm{o}} = Z_{\mathrm{o}} \triangle i_{\mathrm{o}} \tag{2.17}$$

Therefore, it is obvious that if the converter output impedance is altered due to the peaking in the source-side sensitivity function, the transient response might be degraded.

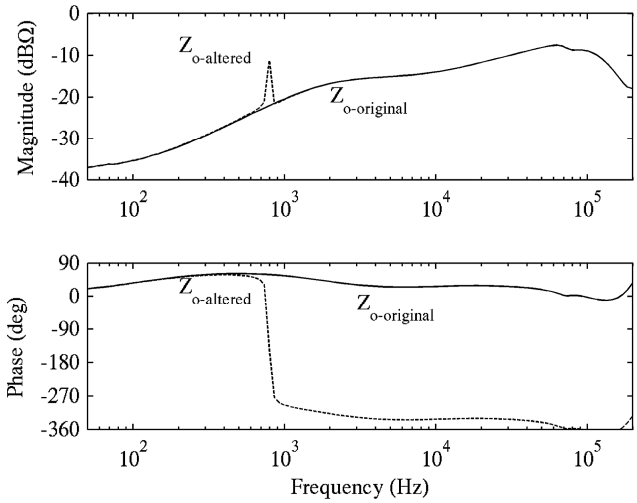

Fig. 2.20: Original and source-affected output impedance.

The maximum value of the sensitivity function can be considered as an important indicator of the altered converter dynamics within interconnected system (Vesti et al., 2013b; Vestii et al., 2013). If the recommended maximum peak value of 2 (6dB) is complied with, the changes in the internal dynamics are considered insignificant and would not impact on the time-domain performance.

2.3.3 MPC-based forbidden region

Applying the presented concept of the maximum peak criteria and the minor-loop gain based sensitivity function, the least conservative circular forbidden area to assess robust stability of distributed system can be defined (Vesti et al., 2013b). This forbidden area is a circle-like region in the complex plane, applied previously in (Wildrick et al., 1995; X.Feng et al., 2002) for online stability margin monitoring and in (Acevedo and Molinas, 2011) to assess the stability of a renewable energy-based microgrid. However, the origin of this forbidden region and proper application to guarantee robust stability in distributed systems was provided later in (Vesti et al., 2013b).

As previously discussed, the distance between the point (-1,0) and the loop-gain L(jω) in the complex plane was defined in (2.11) and in Fig. 2.11. By denoting $|S_{\max}| = M_s$ and L(jω) = α+jβ, a circle can be defined in the complex plane with the center at (-1,0)

and the radius of $1/M_s$ according to (2.18).

$$(1+\alpha)^2 + (\beta)^2 = \frac{1}{M_s^2} \tag{2.18}$$

This circle defines a forbidden region for the minor-loop gain out of which it shall stay for the robust stability to exist. Depending on the required level of robustness, by selecting the value for the maximum peak sensitivity function, the corresponding forbidden region can be specified. In Fig. 2.21, the MPC-forbidden region with the maximum peak of 2 (6dB) is highlighted and compared to the regions in (Middlebrook, 1976; Sudhoff et al., 2000; Wildrick et al., 1995). It can be clearly observed that this forbidden region occupies much less space in the complex plane than the previous criteria but maintaining the same level of robustness or even better.

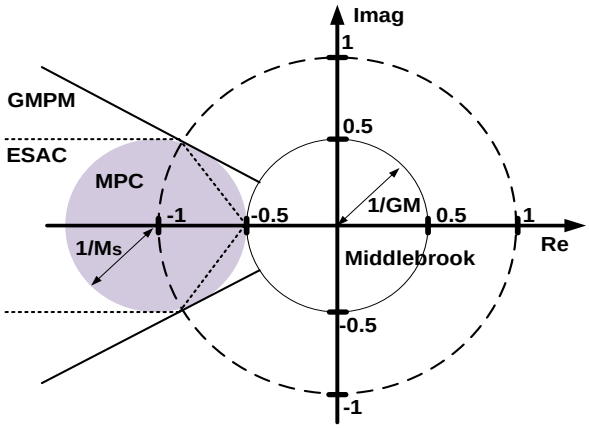

Fig. 2.21: The MPC-based forbidden region with the ESAC and GMPM regions.

It is worth noting that the stability and well-defined transient behavior are guaranteed if the minor-loop gain stays out of the MPC region as well as complies with the Nyquist criterion. The minimum margins provided by the MPC-region can be obtained according to (2.12) based on the selected maximum peak value of the sensitivity function. The MPC-region in Fig. 2.21 guarantees the minimum margins of GM_{MPC} 6dB and PM_{MPC} 29° based on the chosen $S_{\max}$ value of 2.

2.4 Application of the MPC-concept

Having defined the new forbidden region, it is necessary to discuss the proper application of the MPC-concept and validity of the information extractable from the minor-loop gain in terms of robust stability. The state of the small-signal stability in distributed systems is given based on the behavior of the minor-loop gain and it is invariant to component grouping as discussed in (Sudhoff et al., 2000). However, the robustness of stability depends on the interface at which the minor-loop gain is determined (Vesti et al., 2013b). This is due to the basic assumption behind the MPC theory: the robustness and closed-loop performance are defined only for the internal converter transfer functions. Therefore, the minor-loop gain should be obtained at the interface closest to the converter input or output terminal.

2.4.1 Interface for robustness analysis

The MPC-concept can be utilized to assess the influence of the external impedances on the internal transfer functions. In case of excessive peak value of the sensitivity function, as depicted in Fig. 2.16, the robustness is reduced referring that the converter performance might be degraded. Therefore, the robust stability for the defined minor-loop gain is guaranteed by a sufficiently low peak value. However, arbitrarily determined minor-loop gain within the system does not necessarily provide the required information based on which the robustness of stability and the state of transient performance can be assessed.

An experimental prototype system composing of a bus converter supplying two point-of-load converters is shown in Fig. 2.22. The converters are all voltage-mode controlled, non-isolated synchronous buck converters, with switching frequencies of 400kHz and control bandwidths of 100kHz. The main component values of the converter power stages are shown in the figure. The nominal operating condition for the system is defined as:

- Bus converter: $U_{\mathrm{in}} = 20\mathrm{V}$, $U_{\mathrm{o}} = 12\mathrm{V}$ and $I_{\mathrm{o}} = 2.25\mathrm{A}$
- POL 1 converter: $U_{\mathrm{in}} = 12\mathrm{V}$, $U_{\mathrm{o}} = 5\mathrm{V}$ and $I_{\mathrm{o}} = 1\mathrm{A}$
- POL 2 converter: $U_{\mathrm{in}} = 12\mathrm{V}$, $U_{\mathrm{o}} = 5\mathrm{V}$ and $I_{\mathrm{o}} = 4\mathrm{A}$

The robust stability of the POL 2 converter is desired to be analyzed, i.e. to determine the influence of the interconnected system to the internal dynamics of this converter. In order to illustrate the proper application of the presented MPC-concept and the importance of the interface at which the minor-loop gain is determined for robustness analysis, parasitic inductances of different values are connected to the system to create additional interfaces. The system analysis is performed based on measurements and theoretical equations.

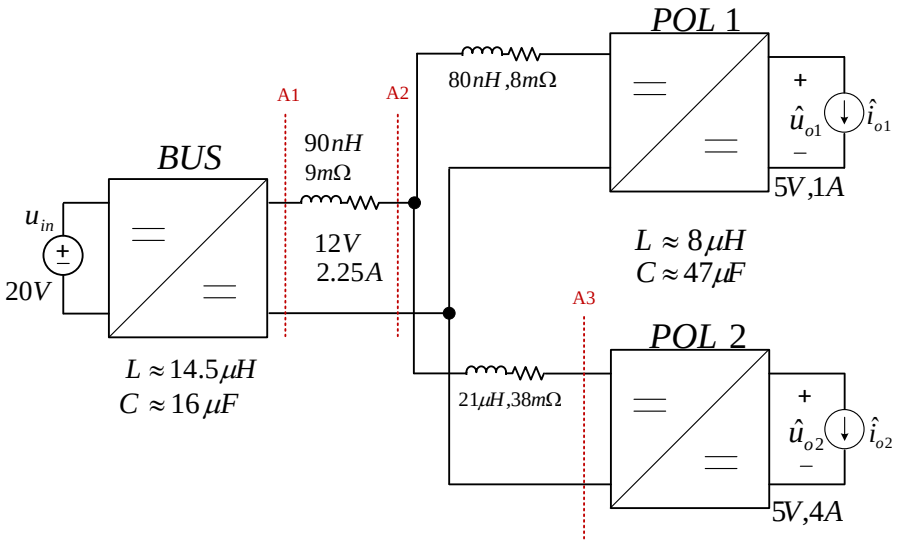

Fig. 2.22: Prototype system structure including additional parasitics.

Three interfaces, (A_1, A_2, A_3) are defined for the system where the corresponding minor-loop gains $Z_{\mathrm{o}}^{\mathrm{S}}/Z_{\mathrm{in}}^{\mathrm{L}}$ are determined. Based on these minor-loop gains, the aim is to analyze the information regarding the robust stability of the POL 2 converter. In order to compute the minor-loops gains at every interface, the following source and load side impedances are required to be measured:

- A_1: $Z_{\text{o-A1}}^{\mathrm{S}}$ is the output impedance of the bus converter, $Z_{\text{o-bus}}$, and $Z_{\text{in-A1}}^{\mathrm{L}}$ is the impedance to the system
- A_2: $Z_{\text{o-A2}}^{\mathrm{S}}$ is the $Z_{\text{o-bus}}$ with the influence of the parasitic inductor and $Z_{\text{in-A2}}^{\mathrm{L}}$ is the impedance to the system after the first parasitic inductor
- A_3: $Z_{\text{o-A3}}^{\mathrm{S}}$ is the impedance seen from the input terminal of POL 2 and $Z_{\text{in-A3}}^{\mathrm{L}}$ is the input impedance of POL2

These impedances at each interface are required to be measured avoiding the rest of the system to couple with the measurements. Therefore, while measuring the source-side output impedance, the load-side of the interface is replaced by an ideal current source maintaining the defined operating condition. Correspondingly, the load-side input impedance is measured replacing the input-side of the interface by an ideal voltage source with the correct operating point.

Based on the measured impedances, the three minor-loop gains A_1, A_2, and A_3 are computed and presented in Fig. 2.23 as Bode plots and in Fig. 2.24 as polar plots, where the MPC-forbidden region corresponds to 6dB peaking. From Fig. 2.24 it can be

observed that every minor-loop gain complies with the Nyquist criterion for stability. The information provided by the minor-loop gains at the interfaces A_1 and A_2 indicates good margins for stability whereas the behavior of the minor-loop gain at the third interface implies that the margins are low due to the short distance between the point (-1,0) and the minor-loop gain.

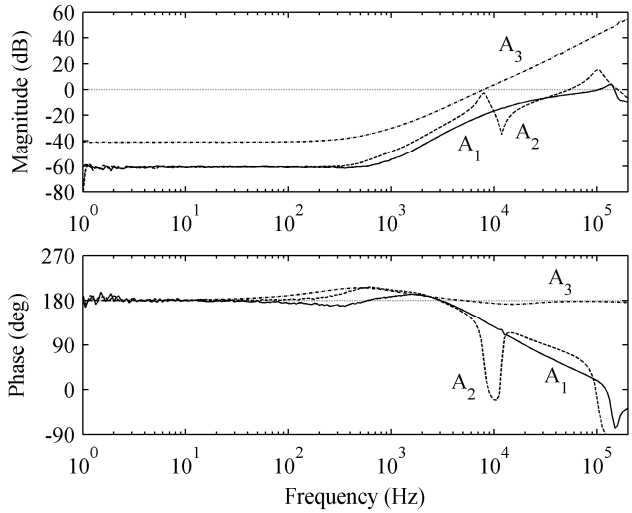

Fig. 2.23: Measured minor-loop gains at the interfaces A1 (solid line), A2 (dashed line) and A3 (dash-dotted line) of the distributed system shown in Fig. 2.22 as a Bode plots.

The behavior of the minor-loop gain A_3 is analyzed in detail at the following operating points:

- 1: POL1 $i_{\mathrm{o1}} = 1\mathrm{A}$ and POL2 $i_{\mathrm{o2}} = 4\mathrm{A}$
- 2: POL1 $i_{\mathrm{o1}} = 4\mathrm{A}$ and POL2 $i_{\mathrm{o2}} = 1\mathrm{A}$

The Nyquist plots of the minor-loop gain A_3 at these operating points are given in Fig. 2.25 where the ESAC and MPC-based forbidden regions are shown. It can be observed that both minor-loop gains are overlapping with the forbidden regions but this violation does not lead to instability, because the Nyquist criterion is complied with. Based on the minimum distance with the point (-1,0) and the minor-loop gain in the operating condition 1, the maximum peak of the sensitivity function is 23.7dB. This corresponds to GM_{MPC} and PM_{MPC} of 0.6dB and 4° according to (2.12).The smaller load current of POL2 in the operating point 2 increases the converter input impedance thus reducing the peaking of the corresponding sensitivity function.

The large $S_{\max}$ value of the operating condition 1 indicates that the internal transfer functions of the POL2 are altered. The output impedance of POL2 is measured while

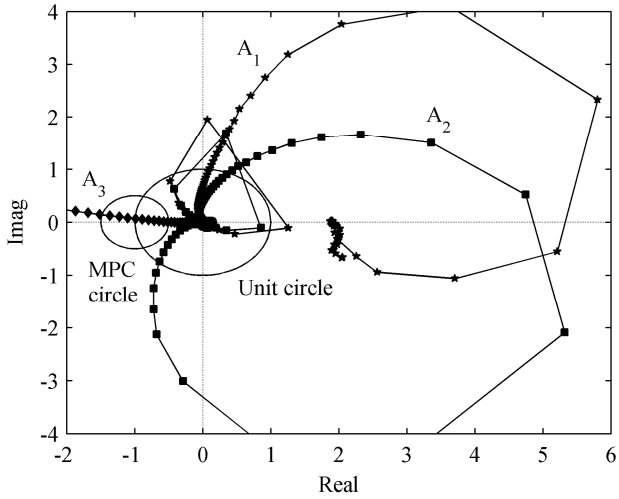

Fig. 2.24: The minor-loop gains as polar plot at the interfaces A_1 (star), A_2 (square) and A_3 (diamond).

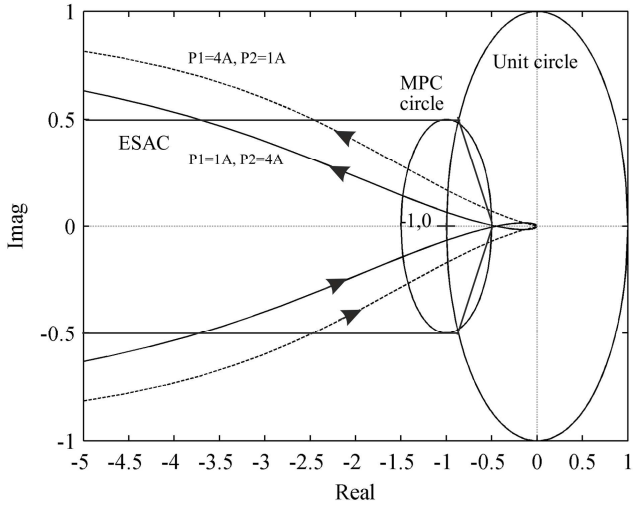

Fig. 2.25: Nyquist plots of the measured minor-loop gains at the interface A_3, where the solid line refers to operating point 1 $I_o = 4$A, and the dashed line refers to operating point 2 $I_o = 1$A).

the system is connected and shown in Fig. 2.26. The high resonance peak is due to the excessive peaking of the source-side sensitivity function of the POL2. This altered output impedance implies degraded converter performance, which is best observed in time-domain. Therefore, a load step from 0.5A to 4A is applied to the output of POL2 and its output voltage response is shown in Fig. 2.27. The decaying oscillatory response

is caused by the resonance in its output impedance which lies within the bandwidth (100kHz) of its voltage-loop gain. Thus the transient response is not only determined by the control system but also by the resonant behavior of the output impedance.

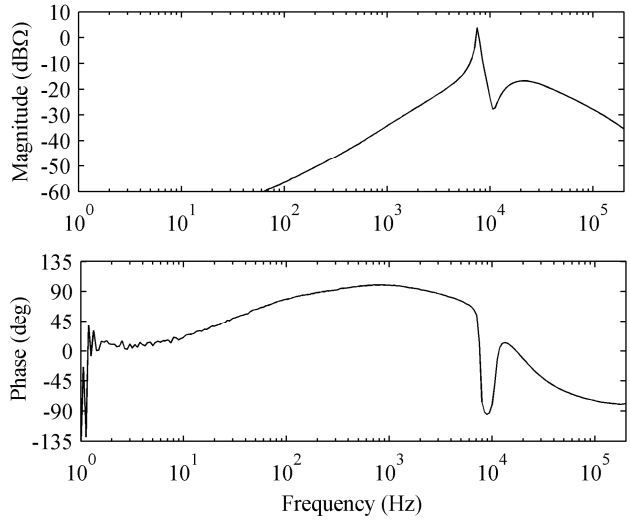

Fig. 2.26: Measured output impedance of the POL2 at the operating condition 1.

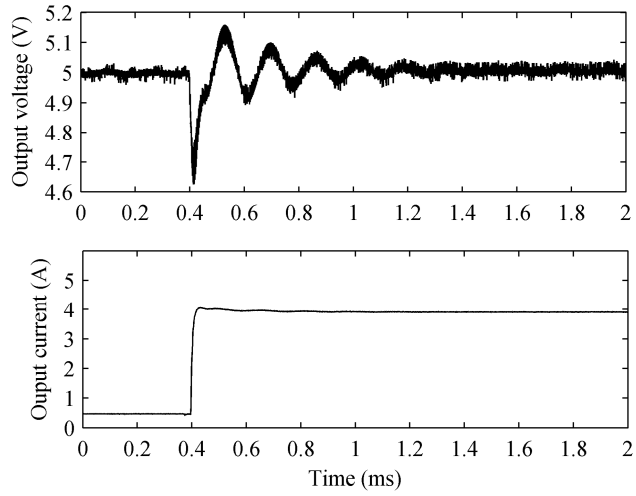

Fig. 2.27: Measured time-domain behavior of POL2 converter when a load step of 0.5A to 4A (250 mA/μs) is applied at the output of the POL2 converter.

The degraded performance of the POL2 influences on the rest of the system. This can be observed from the output voltage response of the bus converter shown in Fig. 2.28.

This repsonse is determined by the bus converter output impedance and the demanded output current. The measured bus converter output impedance is shown in Fig. 2.29 together with the measured output impedances of the POL2 converter under both operating conditions. It can be observed that the measured bus converter output impedance is unaltered by the system, and therefore, the observed degraded performance is due to the oscillatory behavior of the input current demanded by the POL2 and amplified by the bus converter output impedance value ($\approx 100\text{m}\Omega$) at the frequency of the oscillation, which is approximately 6kHz according to Fig. 2.27.

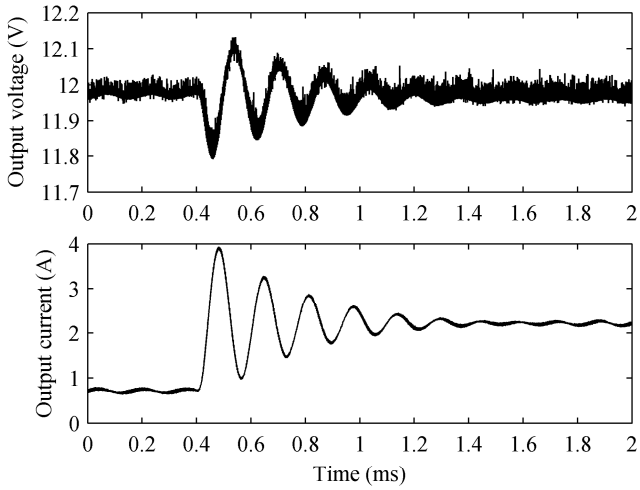

Fig. 2.28: Measured time-domain behavior of the bus converter when a step change in load current from 0.5 to 4 A (250 mA/μs) is applied at the output of the POL2 converter.

These experimental measurements clearly demonstrate that the interface, at which the minor-loop gain is measured, affects the validity of the robustness information. The interfaces A_1 and A_2 are not the direct interfaces with the POL2 converter power stage and do not provide valid data regarding robust stability. For the purpose of emphasizing the importance of the correct interface, an excessive parasitic inductance value was used to form the interface A_3. It can be concluded that the state of the stability can be determined from any of the measured minor-loop gains but in order to correctly predict the robustness, the minor-loop gain should be defined for each converter within the system at their very input or output terminals. In the case of predicting the robust stability for the POL1 converter, new minor-loop gain should be defined at the interface closest to its input terminal.

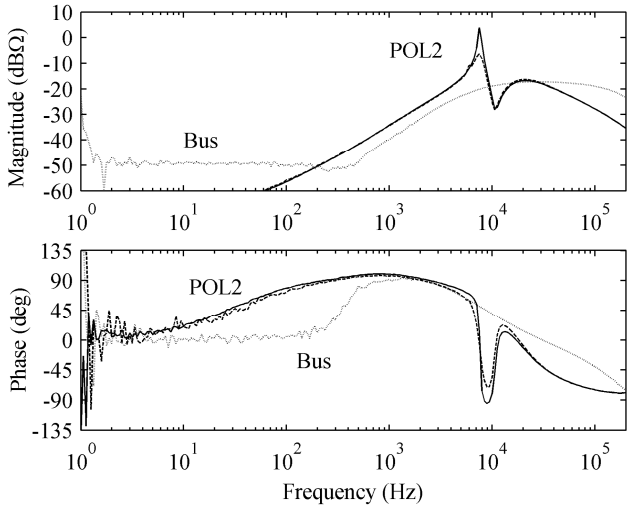

Fig. 2.29: Measured output impedance of the bus converter and the POL2 converter at both operating conditions.

2.4.2 $S_{\max}$-based stability margins

In this thesis, the MPC-concept is used to state the stability margins for a minor-loop gain. The advantage of this method is that a single parameter (value of the maximum peak of the sensitivity function) provides a margin to guarantee robust stability and performance. This parameter considers the combined effects of both gain and phase margins without the need for considering their relations to the frequency. From the $S_{\max}$ value, the GM_{MPC} and PM_{MPC} can be extracted according to (2.12) and for a well-defined minor-loop gain, the peak sensitivity function provides information of the stability margins: the lower the peak value, the better in the sense of robust stability.

The operating point at which the frequency response measurements are performed, influences the stability margins. This is illustrated with the following example of two cascaded dc-dc converters. DC/DC A is a voltage-mode-controlled synchronous buck converter and it supplies another converter which behaves as a constant power load as illustrated in Fig. 2.30. The stability margins are determined for the interface at two operating points.

The output impedance of DC/DC A is measured at: $U_{\mathrm{in}} = 12\mathrm{V}$, $U_{\mathrm{o}} = 5\mathrm{V}$ and $f_{\mathrm{sw}} = 200\mathrm{kHz}$ and the constant power load behavior of the cascaded converter is simulated at two operating conditions: R = -10Ω and R = -2.5Ω with Cin = 17μF, denoting them as first and second condition respectively. The minor-loop gains at both operating conditions are shown in Fig. 2.31 as Nyquist plots, where the MPC-based region is obtained with the maximum peak value of 2 (6dB). It can be observed that the minor-loop gains comply

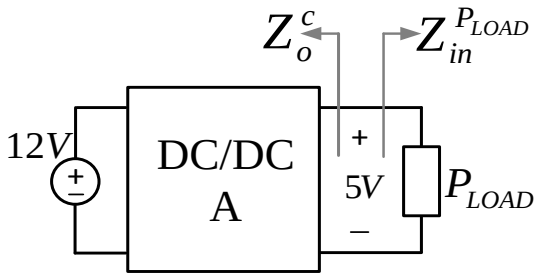

Fig. 2.30: Interconnection of cascaded converters.

with the Nyquist stability criterion without violating the MPC-forbidden region, thus guaranteeing the robust stability.

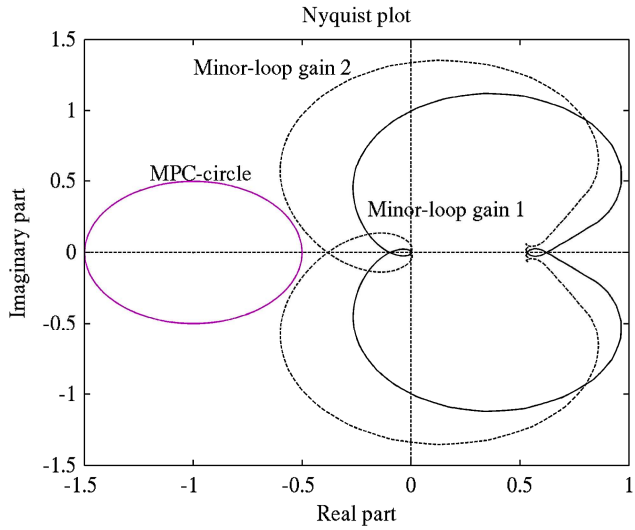

Fig. 2.31: Nyquist plot of the minor-loop gains at operating point 1 (solid line) and point 2 (dashed line)

The compliance with the MPC region provides the minimum stability margins, of GM_{MPC} 6dB and PM_{MPC} 29°. However, utilizing the MPC-concept, specific margins for each minor-loop gain can be computed based on $S_{\max}$ value. The obtained sensitivity functions are shown in Fig. 2.32. It can be observed that $S_{\max}$ values for the condition 1 and 2 are: 1.94dB (1.25) for sensitivity function 1 and 5.5dB (1.8) for sensitivity function 2. These peaks correspond to the minimum distance between the minor-loop gain and the point (-1,0) in Fig. 2.31. Therefore, the operating point at which the system is analyzed influences significantly on the obtained margins and the proper operating condition should be well considered for the stability analysis.

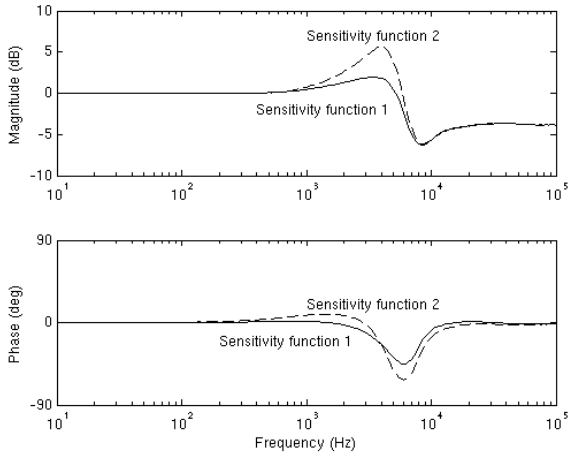

Fig. 2.32: Frequency domain plot of the sensitivity functions at both operating points.

As previously discussed, the objective of all forbidden regions is to provide less conservative stability margins than the original criterion from Middlebrook, where the forbidden region lies outside a circle with the center in the origin and the radius inverse of the GM of 6dB. However, Middlebrook's criterion was originally aimed to be applied in the input filter design, and therefore, a comparison of the least conservative MPC criteria and the Middlebrook's criterion is presented for a dc-dc converter with an input filter.

The input filter is typically designed so that it provides adequate attenuation while guaranteeing the stability. To obtain high enough attenuation, the filter resonant frequency is selected to be much less than the crossover frequency of the output-voltage loop. As a consequence, in order to ensure stability, the input filter has to be designed so that its output impedance peak does not intersect with the closed-loop input impedance of the converter. In addition, in order to avoid affecting the output impedance of the converter the GM of the minor-loop gain has to be large enough (typically 6dB). A dc-dc converter with cascaded input filter is shown in Fig. 2.33, where the converter is a commercial point-of-load converter (TexasInstruments, 2000) operating at $U_{\mathrm{in}} = 12\mathrm{V}$, $U_{\mathrm{o}} = 5\mathrm{V}$ and $I_{\mathrm{o}} = 1.5\mathrm{A}$.

A simple single stage input filter is designed according to the Middlebrook criteria $Z_{\mathrm{o}}^{\mathrm{F}} \ll Z_{\mathrm{in}}^{\mathrm{C}}$ and guaranteeing the minimum GM of 6dB without considering the attenuation features. The parameters of input filter in Fig. 2.33 are: $L_{\mathrm{F}} = 400\mu\mathrm{H}$, $C_{\mathrm{F}} = 220\mu\mathrm{F}$, $r_{\mathrm{L}} = 160\mathrm{m}\Omega$ and $r_{\mathrm{C}} = 50\mathrm{m}\Omega$, resulting to a resonant frequency of approximately 540 Hz. In order to provide more comprehensive comparison of the two stability analysis methods, another filter with different output capacitor: $C_{\mathrm{F2}} = 180\mu\mathrm{F}$ is utilized resulting

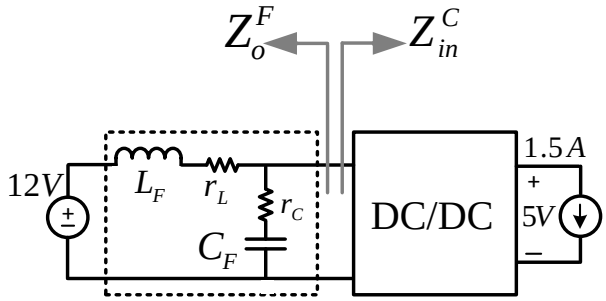

Fig. 2.33: Interconnected filter and a commercial point-of-load converter (TexasInstruments, 2000).

to resonant frequency of approximately 600Hz. The measured converter input impedance and the simulated filter output impedances Z_{o1}^{F} and Z_{o2}^{F} are illustrated in Fig. 2.34.

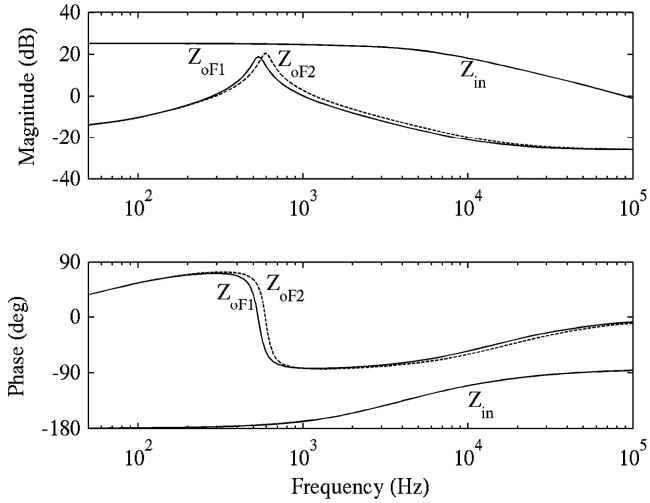

Fig. 2.34: Measured input impedance of the commercial converter and the simulated output impedances of both filters.

In the case of the first filter, Middlebrook's criterion is complied with a margin of 6.2dB. However, for the second filter the margin is only 4.4dB. The computed minor-loop gain based sensitivity functions, S_{F1} (solid line) and S_{F2} (dashed line), are shown in Fig. 2.35. The corresponding peak values are approximately 5.4dB for the first filter and 7.7dB for the second. The computed minor-loop gains are presented in the complex plane in Fig. 2.36. It can be observed that the first minor-loop gain ML_{F1} (solid line) lies inside

the circle defined by Middlebrook's design criterion, and therefore, it also complies with the MPC-forbidden region. However, the second minor-loop gain ML_{F2} (dashed line) does not comply with the Middlebrook criterion and it overlaps with the MPC region.

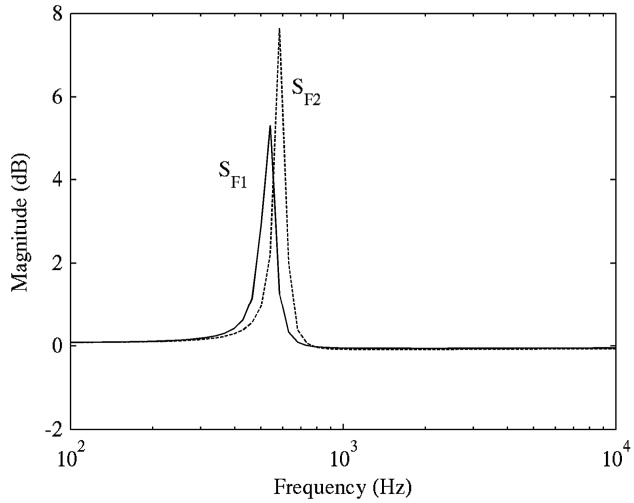

Fig. 2.35: Computed sensitivity functions S_{F1} (solid line) in the case of the first filter and S_{F2} (dashed line) for the second filter.

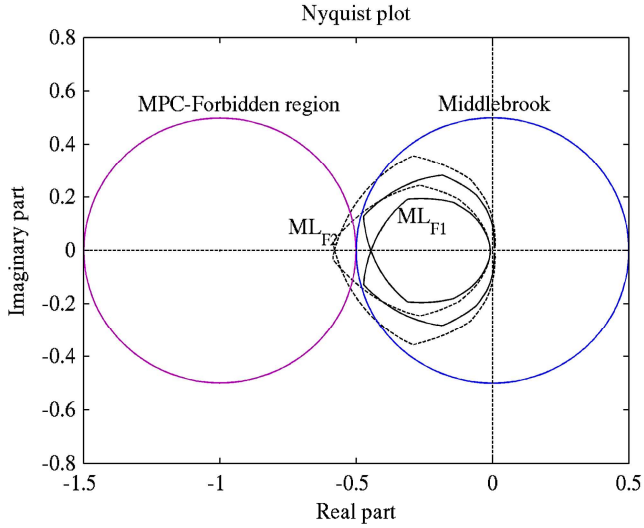

Fig. 2.36: Computed minor-loop gains ML_{F1} (solid line) in the case of the first filter and ML_{F2} (dashed line) in the case of the second filter.

Based on the comparison of these two stability criterion, both methods provide similar

information regarding the robustness of the stability. Therefore, it is stated that even though Middlebrook criterion is too restrictive for the general stability analysis within distributed system, it is quite proper for the input-filter design. Middlebrook's design rules for input filters are practical as well as easily applicable in the actual design and they provide similar margins for stability than the least conservative stability assessment method. Detailed analysis of any possible input filter design option where the minor-loop gain would comply with the MPC but not the Middlebrook, lies outside the scope of this thesis.

2.5 Conclusion

The small-signal stability assessment, based on the impedance ratio known as minor-loop gain, was addressed in this chapter. It was demonstrated that the alternative method, passivity-based criterion, is not appropriate for general stability assessment of a distributed systems. It is very conservative and might lead to discarding a valid design as was demonstrated. In addition, it does not provide margins for stability.

The critical area in the vicinity of the point (-1,0) was shown to determine the robustness of the stability i.e. adequate gain (GM) and phase (PM) margins. Therefore, the smallest distance between the minor-loop gain and the critical point (-1,0) provides the minimum stability margins. The origin and justification for the corresponding least conservative forbidden region was provided, showing that a criterion based on the allowed peaking in the associated sensitivity function forms a circle in the complex plane with the center at (-1,0) and the radius of inverse of the allowed maximum peaking value. This area is sufficient to guarantee robust stability and the value for the peaking can be freely chosen according to the specific robustness requirements for an indented application. This chapter illustrated that presented concept considers the combined effects of both gain and phase margins thus providing a single number for stating robust stability. The sensitivity function was demonstrated to be an important indicator regarding the converter dynamics within interconnected systems.

It was explicitly shown that an arbitrarily measured minor-loop gain within the system might be insufficient to predict correctly the robustness of stability and the state of transient performance. Therefore, well-behaving minor-loop gain alone does not necessarily ensure robust transient performance if it is not correctly defined. In addition, the experiments clearly demonstrate that the minor-loop gain should be defined at the interface closest to the internal terminals of the converter for maximizing the value of the measured information. It was shown that the previously defined forbidden regions are all developed to ensure stability as well as to maintain the changes in the transient performance acceptable. In addition, it was demonstrated that even though the Middlebrook criterion is too conservative for general stability analysis, in the case of input filter

design it provides similar margins than the least conservative stability criterion.

3 INTERACTIONS ANALYSIS

The main contribution of this chapter is to provide a complete set of impedance / admittance parameters, which describe the sensitivity of a switched-mode converter to the source and load interactions. The presented methodology is applicable to any dc-dc converter based on either measured frequency responses or analytic models consisting of circuit parameters. In addition, theoretical formulations for the system-level interactions are provided introducing mechanism for cross-couplings as well as increased source-side interactions sensitivity.

In the previous chapter, the assessment of the small-signal stability and the least conservative margins for the minor-loop gain were provided. However, the impedance based interactions can be more complex as will be described in this chapter. For the stability analysis, the dc-dc converters can be considered as black boxes characterized by their input and output impedances. In this chapter, the dynamical features contributing on the converter interactions sensitivity are analyzed in detail. Therefore, converter models based on their internal components are utilized but the analysis is presented in such a way that it is applicable to commercial converters. The stability and robustness are conveniently assessed utilizing the Nyquist plots, however, these plots are not valid for the assessment of other kind of interactions. Therefore, the analysis presented in this chapter is based on the utilization of the Bode plots, providing a practical approach for the interactions characterization also in the case of commercial converters.

This chapter first discusses the general interactions analysis based on the internal converter transfer functions at open and closed-loop. Thereafter, the main interactions formulations valid for every converter, are presented. From these formulas, special parameters i.e. theoretical impedances are extracted. They describe the converter interactions sensitivity and facilitate the understanding of the interactions phenomena in distributed systems. They are not directly measurable from the converter but are computed based on the measured frequency responses or obtained theoretically based on the circuit parameters according to the analytical equations as will be shown in this chapter. The special parameters are dependent on the applied control method, and therefore, detailed analysis of certain feedback/feedforward arrangements and their influence on interactions is provided based on analytical models. The system-level interactions are assessed in the final section for a system consisting of input-parallel connected converters with a common

input filter. All theoretical discussions and formulations are validated experimentally at the end of each section.

3.1 Introduction

The converter sensitivity to the impedance-based source and load interactions can be characterized by specific impedance or admittance parameters (Choi et al., 2005; Middlebrook, 1989; Suntio, 2010). The existence of such parameters was first established by Middlebrook (Middlebrook, 1976, 1978), when he published the theoretical formulation for the source interactions analysis based on the extra element theorem (EET) (Middlebrook, 1989). The EET is an analytical tool for linear systems to assesses the influence of additional impedance to the original transfer function by employing a correction factor.

The correction factor consists of given extra element Z(s) as well as two impedances, with direct physical interpretation in the system, seen by this extra element. The impedances are theoretical and can be obtained by analyzing the system under different conditions at the port where the extra element is connected as illustrated in Fig. 3.1(Erickson and Maksimovic, 2001; Middlebrook, 1989).

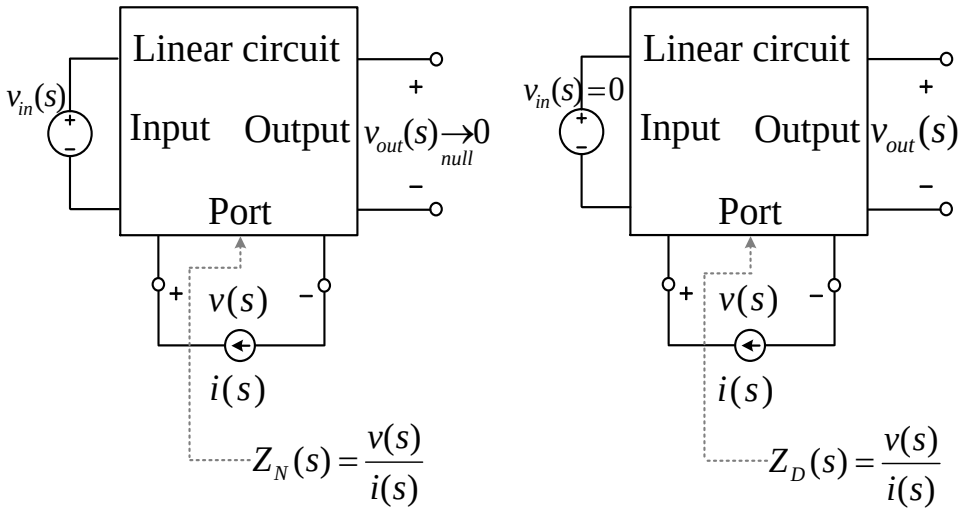

Fig. 3.1: The definition of the two driving point impedances Z_{N} on the left and Z_{D} on the right when the output is nulled and when the input is set to zero, respectively (Erickson and Maksimovic, 2001).

The impedance Z_{N}, illustrated by the system on the left side, is seen from the port when the output is nulled i.e. no current is flowing at the output. The second impedance

Z_{D} is obtained when the input is set to zero (Erickson and Maksimovic, 2001; Middlebrook, 1989). Based on these impedances, the EET is provided in (3.1) where $G_{\mathrm{old}}(s)$ is initially known under the condition that the port is open-circuited and in (3.2) when the port is short-circuited. The right most term in both equations is the correction factor consisting of the extra element Z(s) and the defined impedances.

$$G(s) = G_{\mathrm{old}}(s)|_{\mathrm{Z(s)}\rightarrow\infty}\frac{1 + Z_{\mathrm{N}}(s)/Z(s)}{1 + Z_{\mathrm{D}}(s)/Z(s)} \tag{3.1}$$

$$G(s) = G_{\mathrm{old}}(s)|_{\mathrm{Z(s)}=0}\frac{1 + Z(s)/Z_{\mathrm{N}}(s)}{1 + Z(s)/Z_{\mathrm{D}}(s)} \tag{3.2}$$

If the correction factor equals unity, the original transfer function would remain unaltered. Therefore, to comply with this condition, the EET leads to impedance inequalities which guarantee that the extra impedance does not change the original transfer function. This theorem is applied in the input filter design considering the filter output impedance $Z_{\mathrm{o\text{-}s}}$ as the extra element (Middlebrook, 1976, 1978). This provides a group of inequalities:

- $Z_{\mathrm{o\text{-}s}}(s) \ll Z_{\mathrm{in}}(s)$
- $Z_{\mathrm{o\text{-}s}}(s) \ll Z_{\mathrm{N}}(s)$
- $Z_{\mathrm{o\text{-}s}}(s) \ll Z_{\mathrm{D}}(s)$

which need to be complied with in order to avoid degrading the desirable system performance. The first inequality is obtained from the system minor-loop gain and it provides more than sufficient condition for stability. The other inequalities are obtained applying the extra element theorem and they guarantee unaltered loop gain (Erickson and Maksimovic, 2001). In addition, an independent inequality $Z_{\mathrm{o\text{-}s}}(s) \ll Z_{\mathrm{e}}(s)$, where Z_{e} is the short-circuited input impedance seen from the input when the output is short-circuited, guarantees unaltered converter output impedance (Erickson and Maksimovic, 2001; Middlebrook, 1989). Circuit element-based expressions for these special theoretical impedances are given in (Choi et al., 2005; Erickson and Maksimovic, 2001) for basic converter topologies. However, these expressions require that the internal structure is known, and therefore, they are not applicable for the analysis of commercial converters.

The basis for general interactions formalism, valid for any converter independent of the applied control method and the internal structure, was established in (Hankaniemi et al., 2006b, 2005a; Suntio et al., 2006). The influence of the external source and load-side impedances on the internal transfer functions is assessed based on the two-port structure.

This method enables to obtain general expressions for the source-side special impedances of (Middlebrook, 1976, 1978) based on internal transfer functions. It was identified, that a key dynamical feature contributing on these special parameters is audiosusceptibility G_{io}, which is dependent on the applied control method. By reducing it, the converter source invariance is increased (Hankaniemi et al., 2005a; Suntio et al., 2006, 2009).

Some control methods, such as peak-current-mode (PCM) control inherently provide increased input noise attenuation thus making the converter highly invariant to the source-side interactions (Karppanen et al., 2007b) whereas other traditional scheme, voltage-mode control (VM) or direct-duty-ratio (DDR), is known to have low input noise attenuation (Erickson and Maksimovic, 2001; Hankaniemi et al., 2006a). However, by applying input-voltage-feedforward (IVFF) to the VM-controlled converter the audiosusceptibility can be improved. In (Karppanen et al., 2007a), the dynamical characterization of this feedforwad is presented and the resulting input noise attenuation is comparable to the PCM converter.

The adverse effects of the load impedance to the converter loop-gain are well known (Choi et al., 2002; Peng and Lehman, 2004). Based on the general interactions analysis, the open-loop output impedance $Z_{\mathrm{o\text{-}o}}$ is identified as a critical parameter (Hankaniemi et al., 2005a,b). Therefore, ideally zero open-loop output impedance would guarantee invariance to the load-side interactions. The output impedance of voltage-mode-controlled converter has a low magnitude at low frequencies and peaking at the converter resonant frequency. Thus the loop gain is the most sensitive in the vicinity of the resonant frequency. However, the loop-gain of the PCM-controlled converter is sensitive to the load impedance at low frequencies, where its $Z_{\mathrm{o\text{-}o}}$ is high due to its current-source nature (Karppanen et al., 2007b). In order to reduce this sensitivity, output-current-feedforward (OCF) can be applied to the PCM-controlled converter and in (Karppanen et al., 2007b) the dynamical characterization of this converter is provided.

The dynamical characterization of the above-mentioned traditional control schemes and the feedforward arrangements is well known and reported (Hankaniemi et al., 2005a,b; Karppanen et al., 2007a,b). However, this previously presented interactions formalism is incomplete, because the special impedance parameters characterizing the load effect on the converter input dynamics are missing even though they are vital for the understanding of the full interaction mechanism (Vesti et al., 2012, 2011, 2013a). Comprehensive comparison between the interactions sensitivity under these control schemes in terms of both source and load side interactions is missing and provided in (Vesti et al., 2013a). In this thesis, a complete set of the special parameters with their analytical expressions is given. It is also shown that this interactions formalism can be applied to system-level interactions assessment (Vesti et al., 2012, 2011) demonstrating that the source interactions sensitivity might be slightly increased due to the system interconnection.

3.2 Theoretical interactions formulation

As previously discussed, the applied control method affects on the dynamical features which contribute on the interactions sensitivity. To better assess the control influence, the converter dynamics is represented as a two-port model including the general control variable $\hat{c}$ as an input as illustrated in Fig. 3.2 and in (3.3). In case of open-loop equations, the control variable refers to the duty cycle $\hat{d}$ and for closed-loop it is the reference voltage $\hat{u}_{\mathrm{ref}}$. The transfer functions G_{co} and G_{ci} are the control-to-output and control-to-input transfer functions utilized for the control design.

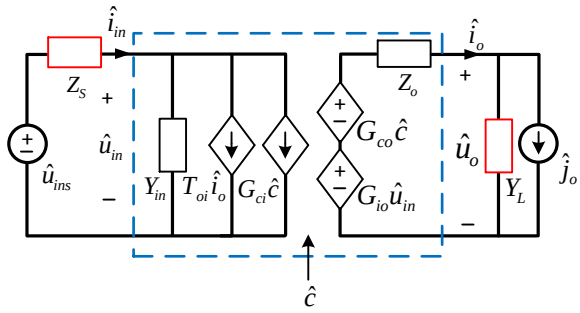

Fig. 3.2: Linear two-port model with nonideal source and load including the control variable.

$$\begin{bmatrix} \hat{i}_{\mathrm{in}} \\ \hat{u}_{\mathrm{o}} \end{bmatrix} = \begin{bmatrix} Y_{\mathrm{in}} & T_{\mathrm{oi}} & G_{\mathrm{ci}} \\ G_{\mathrm{io}} & -Z_{\mathrm{o}} & G_{\mathrm{co}} \end{bmatrix} \begin{bmatrix} \hat{u}_{\mathrm{in}} \\ \hat{i}_{\mathrm{o}} \\ \hat{c} \end{bmatrix} \tag{3.3}$$

The converter input and output dynamics are illustrated in Fig. 3.3 as a general control block-diagram under output-side-feedback and the corresponding closed-loop dynamics is provided in (3.4) (Suntio et al., 2006, 2010). From this representation, it can be clearly observed how the feedback alters the open-loop transfer functions and the stability is given by the loop-gain L_{out} (3.5), where G_{se} is the sensing gain, G_{a} the modulator gain, G_{cc} the controller transfer function and G_{co} the control-to-output transfer function of the converter. This closed-loop dynamics is used in the following sections to facilitate the interpretation of the special parameters describing the interactions sensitivity.

$$\begin{bmatrix} \hat{i}_{\text{in}} \\ \hat{u}_{\text{o}} \end{bmatrix} = \begin{bmatrix} \frac{Y_{\text{in-o}}}{1+L_{\text{out}}} + \frac{L_{\text{out}}Y_{\text{in-}\infty}}{1+L_{\text{out}}} & \frac{T_{\text{oi-o}}}{1+L_{\text{out}}} + \frac{L_{\text{out}}T_{\text{oi-}\infty}}{1+L_{\text{out}}} & \frac{G_{\text{ci-o}}}{G_{\text{se}}G_{\text{co-o}}}\frac{L_{\text{out}}}{1+L_{\text{out}}} \\ \frac{G_{\text{io-o}}}{1+L_{\text{out}}} & -\frac{Z_{\text{o}}}{1+L_{\text{out}}} & \frac{1}{G_{\text{se}}}\frac{L_{\text{out}}}{1+L_{\text{out}}} \end{bmatrix} \begin{bmatrix} \hat{u}_{\text{in}} \\ \hat{i}_{\text{o}} \\ \hat{u}_{\text{ref}} \end{bmatrix} \tag{3.4}$$

$$L_{\text{out}} = G_{\text{se}}G_{\text{a}}G_{\text{cc}}G_{\text{co}} \tag{3.5}$$

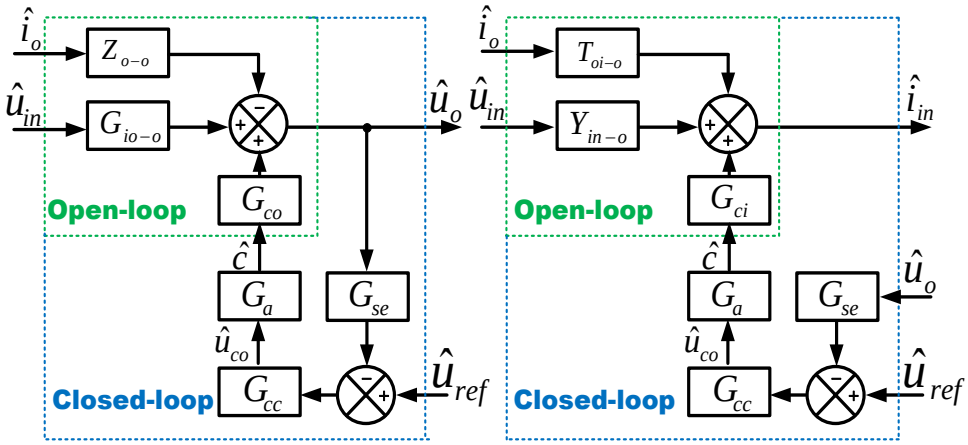

Fig. 3.3: The output and input side dynamics of a closed-loop converter with an output voltage feedback.

From this expression, two special transfer functions, ideal input admittance ($Y_{\text{in-}\infty}$) and ideal output-to-input transfer function ($T_{\text{oi-}\infty}$), are identified. They can be expressed according to the open-loop transfer functions as given in (3.6) and (3.7) respectively. However, in case input-current-feedback is applied, like in maximum-power-point tracking converters for photovoltaic applications, the resulting closed loop dynamics is different (Suntio et al., 2010).

$$Y_{\text{in-}\infty} = \frac{\hat{i}_{\text{in}}}{\hat{u}_{\text{in}}}|_{\hat{i}_{\text{o}}=0,\hat{u}_{\text{o}}=0} = Y_{\text{in-o}} - \frac{G_{\text{io-o}}G_{\text{ci-o}}}{G_{\text{co-o}}} \tag{3.6}$$

$$T_{\text{oi-}\infty} = \frac{\hat{i}_{\text{in}}}{\hat{i}_{\text{o}}}|_{\hat{u}_{\text{o}}=0,\hat{u}_{\text{in}}=0} = T_{\text{oi-o}} + \frac{Z_{\text{o-o}}G_{\text{ci-o}}}{G_{\text{co-o}}} \tag{3.7}$$

3.2.1 Source-side special parameters

The influence of external impedance to the converter loop gain is assessed utilizing the open-loop transfer functions, i.e. considering the control variable as an input to the system. The source-affected dynamics is obtained as described in Chapter 2 including the source-impedance as a part of the system. The resulting dynamics is provided in (3.8) including control-signal related transfer functions. Detailed derivation of the equations is given in Appendix B. The stability is now given by the minor-loop gain $Z_{\text{s}}Y_{\text{in}}$. From these equations, two special parameters influencing the control-to-output transfer function (G_{co}) and the output impedance (Z_{o}) can be identified:

- $Y_{\text{in-}\infty}$, ideal input admittance (3.6)
- $Y_{\text{in-sco}}$, input admittance at open-circuit output (3.9)

$$\begin{bmatrix} \hat{i}_{\text{in}} \\ \hat{u}_{\text{o}} \end{bmatrix} = \begin{bmatrix} \frac{Y_{\text{in}}}{1+Z_{\text{s}}Y_{\text{in}}} & \frac{T_{\text{oi}}}{1+Z_{\text{s}}Y_{\text{in}}} & \frac{G_{\text{ci}}}{1+Z_{\text{s}}Y_{\text{in}}} \\ \frac{G_{\text{io}}}{1+Z_{\text{s}}Y_{\text{in}}} & -\frac{1+Z_{\text{s}}Y_{\text{in-sco}}}{1+Z_{\text{s}}Y_{\text{in}}}Z_{\text{o}} & \frac{1+Z_{\text{s}}Y_{\text{in-}\infty}}{1+Z_{\text{s}}Y_{\text{in}}}G_{\text{co}} \end{bmatrix} \begin{bmatrix} \hat{u}_{\text{ins}} \\ \hat{i}_{\text{o}} \\ \hat{u}_{\text{ref}} \end{bmatrix} \tag{3.8}$$

$$Y_{\text{in-sco}} = \frac{\hat{i}_{\text{in}}}{\hat{u}_{\text{in}}}|_{\hat{c}=0,\hat{u}_{\text{o}}=0} = Y_{\text{in}} + \frac{G_{\text{io}}T_{\text{oi}}}{Z_{\text{o}}} \tag{3.9}$$

$Y_{\text{in-}\infty}$ represents the input admittance measured from the converter input terminal assuming ideal feedback controller and it is obtained from the small-signal model by nulling the output voltage (Erickson and Maksimovic, 2001; Middlebrook, 1976). The extraction of this special impedance (3.6) from the two-port model under the condition: $\hat{u}_{\text{o}} = 0$ and $\hat{i}_{\text{o}} = 0$, is illustrated in Appendix C. According to the closed-loop dynamic representation (3.4), the $Y_{\text{in-}\infty}$ characterizes the ohmic property of the closed-loop input admittance $Y_{\text{in-c}}$ (3.10) at low frequencies where the corresponding feedback loop gain is high ($1 \ll L_{\text{out}}$) and the converter exhibits constant power behavior.

$$Y_{\text{in-c}} = \frac{Y_{\text{in-o}}}{1+L_{\text{out}}} + \frac{L_{\text{out}}Y_{\text{in-}\infty}}{1+L_{\text{out}}} \approx |Y_{\text{in}\infty}| \approx -\frac{I_{\text{in}}}{U_{\text{in}}} \tag{3.10}$$

The other input-side special impedance $Y_{\text{in-sco}}$ is obtained from the small-signal model, when the converter output is shorted (Erickson and Maksimovic, 2001; Middlebrook, 1976). The extraction of this parameter from the two-port model is illustrated in Appendix C under the condition: $\hat{u}_{\text{o}} = 0$ and $\hat{c} = 0$. The corresponding impedance $Z_{\text{in-sco}}$ is typically the lowest of the input-side impedances, especially at low frequency.

Both parameters are independent of the output-side feedback state referring that whether the internal transfer functions are obtained at open or closed-loop, the resulting parameter is the same as illustrated in Appendix C. However, $Y_{\text{in-sco}}$ is dependent on the operation mode (i.e. CCM/DCM) and the internal feedback/feedforward arrangements, because they influence on the converter dynamics as will be demonstrated in the following section.

3.2.2 Load-side special parameters

The load-affected dynamics is obtained as described in Chapter 2 including the load-admittance as a part of the system. The corresponding dynamics is given in (3.11) including the control transfer functions and where the stability is given by the minor-loop gain $Z_{\text{o}}Y_{\text{L}}$. Detailed extraction is provided in Appendix D. From these equations, two special parameters influencing the control-to-input transfer function (G_{ci}) and the input admittance (Y_{in}) can be identified:

- $Z_{\text{o-}\infty}$, ideal output impedance
- $Z_{\text{o-oci}}$, output impedance at open-circuit input

The ideal output impedance is given in (3.12) and $Z_{\text{o-oci}}$ is given in (3.13) for open-loop and in (3.14) for the closed-loop.

$$\begin{bmatrix} \hat{i}_{\text{in}} \\ \hat{u}_{\text{o}} \end{bmatrix} = \begin{bmatrix} \frac{1+Z_{\text{o-oci}}Y_{\text{L}}}{1+Z_{\text{o}}Y_{\text{L}}}Y_{\text{in}} & \frac{T_{\text{oi}}}{1+Z_{\text{o}}Y_{\text{L}}} & \frac{1+Z_{\text{o-}\infty}Y_{\text{L}}}{1+Z_{\text{o}}Y_{\text{L}}}G_{\text{ci}} \\ \frac{G_{\text{io}}}{1+Z_{\text{o}}Y_{\text{L}}} & -\frac{Z_{\text{o}}}{1+Z_{\text{o}}Y_{\text{L}}} & \frac{G_{\text{co}}}{1+Z_{\text{o}}Y_{\text{L}}} \end{bmatrix} \begin{bmatrix} \hat{u}_{\text{in}} \\ \hat{j}_{\text{o}} \\ \hat{u}_{\text{ref}} \end{bmatrix} \tag{3.11}$$

$$Z_{\text{o-}\infty} = \frac{\hat{u}_{\text{o}}}{\hat{i}_{\text{o}}}|_{\hat{i}_{\text{in}}=0,\hat{u}_{\text{in}}=0} = Z_{\text{o}} + \frac{G_{\text{co}}T_{\text{oi}}}{G_{\text{ci}}} \tag{3.12}$$

$$Z^{\text{o}}_{\text{o-oci}} = \frac{\hat{u}_{\text{o}}}{\hat{i}_{\text{o}}}|_{\hat{i}_{\text{in}}=0,\hat{c}=0} = Z_{\text{o-o}} + \frac{G_{\text{io-o}}T_{\text{oi-o}}}{Y_{\text{in-o}}} = \frac{Z_{\text{o-o}}}{Y_{\text{in-o}}}Y_{\text{in-sco}} \tag{3.13}$$

$$Z^{\mathrm{c}}_{\text{o-oci}} = \frac{\hat{u}_{\mathrm{o}}}{\hat{i}_{\mathrm{o}}}|_{\hat{i}_{\mathrm{in}}=0,\hat{c}=0} = Z_{\text{o-c}} + \frac{G_{\text{io-c}}T_{\text{oi-c}}}{Y_{\text{in-c}}} = \frac{Z_{\text{o-c}}}{Y_{\text{in-c}}}Y_{\text{in-sco}} \tag{3.14}$$

The open-circuit output impedance $Z_{\text{o-oci}}$ was provided in (Vesti et al., 2012, 2011, 2013a) and it completes the previously presented interactions formulation. It characterizes the influence of the load impedance to the input impedance and is obtained from the small-signal model under the condition of open circuited input. Its extraction from the two-port model when $\hat{c} = 0$ and $\hat{i}_{\mathrm{in}} = 0$ is provided in Appendix E. It should be noted that this impedance depends on the state of the output-side feedback as illustrated in Appendix E. Therefore, it has different values at open (3.13) and closed-loop (3.14).

The ideal output impedance (3.12) refers to an impedance that is obtained under the condition that the input-current control is ideal ($\hat{i}_{\mathrm{in}} = 0$) and it is independent of the state of the feedback as demonstrated in Appendix E. Its extraction from the two-port model under the condition: $\hat{u}_{\mathrm{in}} = 0$ and $\hat{i}_{\mathrm{in}} = 0$ is demonstrated in Appendix E. For a converter with input-side-feedback, $Z_{\text{o-}\infty}$ characterizes the closed-loop output impedance ($Z_{\text{o-c}}$) at the low frequencies where the corresponding feedback loop gain L_{in} is high (3.15) and it represents the constant power behavior of the output terminal at low frequencies (Suntio et al., 2010).

$$Z_{\text{o-c}} = \frac{Z_{\text{o-o}}}{1 + L_{\mathrm{in}}} + \frac{L_{\mathrm{in}}}{1 + L_{\mathrm{in}}}Z_{\text{o-}\infty} \approx |Z_{\text{o}\infty}| \approx \frac{U_{\mathrm{o}}}{I_{\mathrm{o}}} \tag{3.15}$$

3.2.3 Main interactions formulation

Based on the presented source and load-affected dynamics, the main interaction formulations for a traditional output-side feedback controlled converter are collected in (3.16) - (3.19), where the superscripts S and L denote source and load affected transfer functions. These expressions are obtainable based on the EET, however, by applying the presented methodology the special impedance parameters are expressed explicitly based on the internal transfer functions.

$$L^{\mathrm{s}}_{\mathrm{out}} = \frac{1 + Z_{\mathrm{s}}Y_{\text{in-}\infty}}{1 + Z_{\mathrm{s}}Y_{\text{in-o}}}L_{\mathrm{out}} \tag{3.16}$$

$$Z^{\mathrm{s}}_{\mathrm{o}} = \frac{1 + Z_{\mathrm{s}}Y_{\text{in-sco}}}{1 + Z_{\mathrm{s}}Y_{\mathrm{in}}}Z_{\mathrm{o}} \tag{3.17}$$

$$L_{\text{out}}^{\text{L}} = \frac{L_{\text{out}}}{1 + Z_{\text{o-o}} Y_{\text{L}}} \tag{3.18}$$

$$Y_{\text{in}}^{\text{L}} = \frac{1 + Z_{\text{o-oci}}^{\text{x}} Y_{\text{L}}}{1 + Z_{\text{o}} Y_{\text{L}}} Y_{\text{in}} \tag{3.19}$$

The influence of the load-side impedance on the loop-gain can be assessed based on (3.18) and to the input dynamics according to (3.19). The superscript x refers that the transfer functions can be either open or closed-loop. The original transfer functions in (3.16), (3.17), (3.19) remain unaffected by the source or load impedances if the numerator and denominator polynomials are equal thus canceling each other. In addition, to guarantee robust stability, the source or load-side minor-loop-gain based sensitivity function needs to comply with the conditions specified in Chapter 2.

For a source invariant converter all input-side admittances are the same. This occurs, if the audiosusceptibility G_{io} is small in (3.6) and (3.9). Thus the source-side interaction propagation between the input and output terminals is prevented, because the original input admittances remain unaltered by the external impedance. Otherwise the converter is sensitive to the interactions and the following conditions:

- $Z_{\text{s}} Y_{\text{in}} \ll 1$
- $Z_{\text{s}} Y_{\text{in-}\infty} \ll 1$
- $Z_{\text{s}} Y_{\text{in-sco}} \ll 1$

need to be complied with. Guaranteeing these conditions, refers that the converter performance is not degraded due to the external source impedance. It should be noted that the output impedance of a converter with high input noise attenuation is not influenced by large peak in the source-side sensitivity function $1/(1+Z_{\text{s}} Y_{\text{in}})$, because the input-side impedances cancel each other. However, the other internal transfer functions would be altered due to the peaking.

Correspondingly, for a load invariant converter all output-side impedances are the same. This occurs, if the audiosusceptibility G_{io} is small in (3.13) and (3.14). Thus the converter input dynamics remains unaltered by the load impedance. Otherwise the converter is sensitive to the interactions and the following conditions:

- $Z_{\text{o}} Y_{\text{L}} \ll 1$
- $Z_{\text{o-oci}}^{\text{x}} Y_{\text{L}} \ll 1$

need to be complied with. This guarantees that the input impedance remains unaltered due to the load impedance interconnection. The loop-gain sensitivity (3.18) to the load impedance is determined by the shape of the open-loop output impedance magnitude. It is the most sensitive to load interactions at the frequencies where the open-loop output impedance has its highest value. Thus a converter with zero $Z_{\text{o-o}}$ and zero G_{io} would be highly invariant to both source and load-impedances.

The presented equations form the basis for the overall interaction analysis. It should be noted that in the case of commercial converters, the interactions are assessable based on (3.17) and (3.19), because only four closed-loop transfer functions are measurable from the input and output terminals.

3.3 Control method influence on the interaction

This section discusses the traditional control methods and their influence on the dynamical features which make the converter sensitive to the interactions. Detailed control design and the derivation of the analytical models under each scheme are out of the scope of this thesis. The discussed control methods are briefly introduced so that their influence on the dynamics is clear. The dynamical characterization and detailed derivation of analytical state-space models for buck converter under these control methods are presented in (Hankaniemi et al., 2005a,b; Karppanen et al., 2007a,b) as well as the experimental validation of the models. In this section, these analytical models and their corresponding frequency response characterizations are utilized as a basis for the interactions analysis to fully explain and demonstrate the interaction phenomena. Analytical representations of the special parameters based on circuit parameters are extracted and validated experimentally.

3.3.1 Circuit-element-based interactions parameters

Based on the formulations presented in the previous section, the main dynamical features influencing the interaction sensitivity are the input noise attenuation G_{io} and the open-loop output impedance $Z_{\text{o-o}}$. These features are dependent on the utilized feedback/feedforward arrangements. Therefore, to analyze the control method influence on the interactions sensitivity, explicit representation of the special parameters based on circuit elements is required. These parameters are not directly measurable and are difficult to obtain applying the extra-element theorem due to their complexity and implicit nature (Choi et al., 2005; Middlebrook, 1976).

The analytical expressions for the impedance parameters are obtained by:

- Applying state-space averaging and forming the circuit-element-based representation of the internal dynamics

- Solving the special parameters (3.6), (3.9), (3.12)-(3.14) using the obtained circuit-element-based representations for the transfer functions

The analytical models as well as the experimental validations presented in this chapter, are based on the same power stage shown in Fig. 3.4 illustrating the necessary feedback and feedforward arrangements for the VM, IVFF, PCM and OCF controlled converters. The converter operates in continuous conduction mode and the operating conditions are defined in the figure. The protoype consists of the following component values: L = 105μH, r_{L} = 60mΩ, C = 316μF, r_{C} =33mΩ, r_{ds} = 0.2-0.4Ω, r_{d} = 55mΩ and R_{s1} = R_{s2} =75mΩ. The output-voltage loop gain for each control scheme is designed to have a crossover frequency approximately at 10kHz at 50V input.

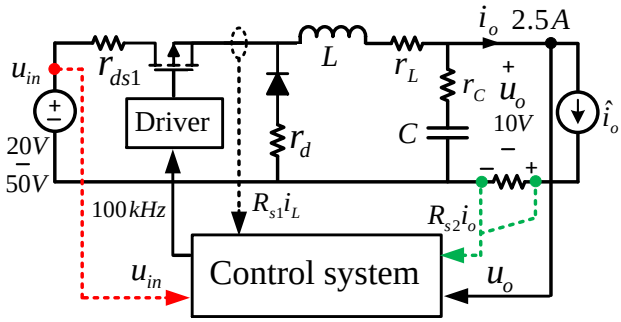

Fig. 3.4: Buck converter with all the feedback and feedforward arrangements.

3.3.2 Source-side interactions formulation for VM and IVFF-control

The main objective for the input-voltage-feedforward (IVFF) is to ideally obtain zero audiosusceptibility, $G_{\mathrm{io\text{-}o}}$, and thus improving the source-side interactions sensitivity of VM-controlled converter. The IVFF influence on the VM-converter dynamics is given in (3.20) based on the control block diagram in Fig. 3.5, where the transfer functions inside the dashed line represent the open-loop VM-converter. The circuit-element based open-loop dynamics for the IVFF-controlled converter is provided in Appendix F, where the following gains utilized in this control are defined in detail:

- Input-voltage-feedforward gain q_{i}^{IF}
- Duty-ratio gain F_{m}^{IF}

$$\begin{bmatrix} \hat{i}_{\mathrm{in}} \\ \hat{u}_{\mathrm{o}} \end{bmatrix} = \begin{bmatrix} Y_{\text{in-o}} - F_{\mathrm{m}}^{\mathrm{IF}} q_{\mathrm{i}}^{\mathrm{IF}} G_{\mathrm{ci}} & T_{\text{oi-o}} & F_{\mathrm{m}}^{\mathrm{IF}} G_{\mathrm{ci}} \\ G_{\text{io-o}} - F_{\mathrm{m}}^{\mathrm{IF}} q_{\mathrm{i}}^{\mathrm{IF}} G_{\mathrm{co}} & -Z_{\text{o-o}} & F_{\mathrm{m}}^{\mathrm{IF}} G_{\mathrm{co}} \end{bmatrix} \begin{bmatrix} \hat{u}_{\mathrm{in}} \\ \hat{i}_{\mathrm{o}} \\ \hat{u}_{\mathrm{ref}} \end{bmatrix} \tag{3.20}$$

From this dynamical representation, the condition for zero audiosusceptibility, $G_{\text{io-o}}^{\mathrm{IF}}$, can be derived as is given in (3.21).

$$F_{\mathrm{m}}^{\mathrm{IF}} q_{\mathrm{i}}^{\mathrm{IF}} = \frac{G_{\text{io-o}}}{G_{\mathrm{co}}} \tag{3.21}$$

In (Karppanen et al., 2007a) the IVFF is implemented by making the PWM-ramp directly proportional to the input voltage resulting to $F_{\mathrm{m}}^{\mathrm{IF}} q_{\mathrm{i}}^{\mathrm{IF}} = \mathrm{D}/U_{\mathrm{in}}$. For a VM-controlled buck converter with input-voltage-feedforward, a zero $G_{\text{io-o}}^{\mathrm{IF}}$ refers that:

- All input-side impedances are equal
- The open-loop input impedance $Y_{\text{in-o}}^{\mathrm{IF}}$ in (3.20) becomes equal to (3.6) thus resembling negative incremental resistance even without the output voltage feedback.

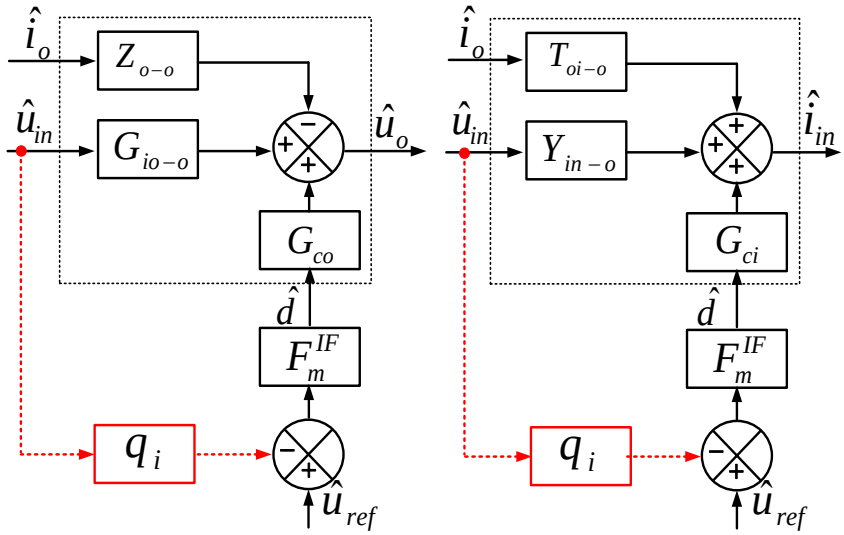

Fig. 3.5: Control block diagrams for assessing the effect of IVFF for output and input dynamics.

The dynamical circuit-element based representations of the buck converter under VM- and IVFF control are given in Appendix F and according to them, the source-side special parameters, $Y_{\text{in-}\infty}$ (3.6) and $Y_{\text{in-sco}}$(3.9), are solved. The corresponding ideal input

impedance $Z_{\text{in-}\infty}$ given in (3.22) characterizes the constant power behavior at low frequencies as previously discussed and is the same for all converters independent of the control scheme. The analytical expressions for the input-short-circuit impedances are provided in (3.23) and (3.24) for the VM and IVFF control, respectively. The equivalent parameters U_{E} and r_{E} include the influence of the circuit parasitics and are also defined in Appendix F.

$$Z_{\text{in-}\infty} = \frac{\hat{u}_{\text{in}}}{\hat{i}_{\text{in}}}|_{\hat{i}_{\text{o}}=0,\hat{u}_{\text{o}}=0} = -\frac{U_{\text{E}}}{DI_{\text{o}}} \approx -\frac{U_{\text{in}}}{I_{\text{in}}} \tag{3.22}$$

$$Z^{\text{VM}}_{\text{in-sco}} = \frac{\hat{u}_{\text{in}}}{\hat{i}_{\text{in}}}|_{\hat{c}=0,\hat{u}_{\text{o}}=0} = \frac{r_{\text{E}} + sL}{D^2} \tag{3.23}$$

$$Z^{\text{IF}}_{\text{in-sco}} = \frac{\hat{u}_{\text{in}}}{\hat{i}_{\text{in}}}|_{\hat{c}=0,\hat{u}_{\text{o}}=0} = \frac{r_{\text{E}} + sL}{D(D - F^{\text{IF}}_{\text{m}} q^{\text{IF}}_{\text{i}} U_{\text{E}}) - F^{\text{IF}}_{\text{m}} q^{\text{IF}}_{\text{i}} I_{\text{o}}(r_{\text{E}} + sL)} \tag{3.24}$$

As previously discussed, if the feedforward is designed so that $F^{IF}_{\text{m}}\, q^{IF}_{\text{i}} = \text{D}/U_{\text{in}}$ from (3.24) it can be observed that the $Z^{IF}_{\text{in-sco}}$ equals the ideal input impedance (3.22). However, in practice the feedforward is impossible to design so that the audiosusceptibility is completely nullified, and therefore, the $Z^{IF}_{\text{in-sco}}$ does not perfectly match the other input-side impedances. Nevertheless, it can be stated that $Z^{\text{VM}}_{\text{in-sco}} \ll Z^{\text{IF}}_{\text{in-sco}}$ yielding reduced interactions sensitivity as a comparison to the VM-controlled converter.

The source-side stability is analyzed based on the closed-loop input impedance, which represents the negative incremental resistance behavior. However, instability might occur even if the converter is operating at open-loop in the following cases:

- Open-loop buck converter with a fixed duty is supplying another regulated converter, which behaves as a constant power load
- IVFF is applied to the open-loop buck converter

The load impedance influence to the open-loop input impedance (3.25) is extracted based on the load-affected dynamics in (3.11) and the circuit-element-based representation in Appendix F. The resulting load-affected input impedance is given in (3.26), where R_{L} represents the ohmic property of the load impedance which can be a conventional resistance or negative incremental input resistance of a regulated downstream converter. Therefore, if the open-loop buck converter is supplying another regulated converter the low-frequency phase of the input impedance can start at -180° and as a consequence the converter might become unstable.

$$Z_{\text{in-o}} = \frac{s^2LC + s(r_{\text{E}} + r_{\text{C}})C + 1}{sD^2C} \tag{3.25}$$

$$Z_{\text{in-o}}^{\text{L}} = \frac{R_{\text{L}}}{D^2}\frac{s^2LC + s((r_{\text{E}} + r_{\text{C}})C + L/R_{\text{L}}) + 1}{1 + sR_{\text{L}}C} \tag{3.26}$$

As previously discussed, the input-voltage-feedforward makes $Z_{\text{in-o}}$ equal the ideal input impedance in (3.22). Therefore, the negative-incremental-resistance property of the IVFF-controlled converter input terminal makes it prone to instability even at open loop. Both of these converters can be used as a bus converter in distributed systems without applying the output-voltage feedback. The open-loop converter operates with a fixed duty ratio whereas the IVFF converter improves the rejection of input voltage variations. Therefore, the stability analysis should not be neglected even if the converter is operating at open-loop due to the system interactions.

3.3.3 Source-side interactions formulation for PCM and OCF-control

The peak-current-mode-control is well-known and it provides inherent input voltage disturbance rejection due to the introduced compensation ramp (Erickson and Maksimovic, 2001). Therefore, close to zero audiosusceptibility can be obtained. The circuit-element based open-loop dynamics for the PCM-controlled converter is provided in Appendix G, where the following gains utilized in this control are defined in detail:

- Duty-ratio gain F_{m}^{PCM}
- Inductor-current feedback gain q_{c}^{PCM}
- Input-voltage-feedforward gain q_{i}^{PCM}

As previously mentioned, the PCM-controlled converter has high open-loop output impedance, which can be reduced by introducing output-current-feedforward. Thus, the loop-gain sensitivity to the load impedance is decreased. This OCF-scheme is illustrated by the control block diagram in Fig. 3.6 based on the PCM dynamics. The dynamical model of the OCF- controlled converter is derived from the PCM-controlled converter and given in (3.27). It can be observed that only $Z_{\text{o-o}}$ and $T_{\text{oi-o}}$ are influenced by the output current feedforward. The circuit-element based open-loop dynamics of the OCF-control is given in Appendix G.

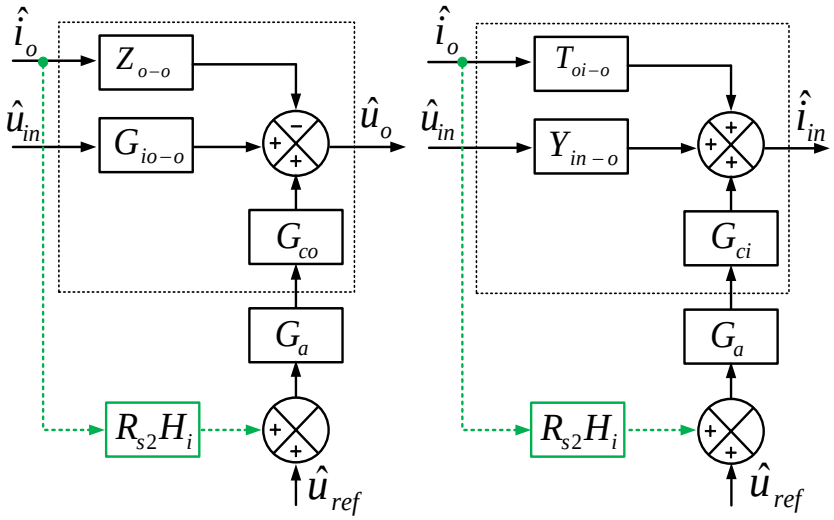

Fig. 3.6: Control block diagrams for assessing the effect of OCF for output and input dynamics.

$$\begin{bmatrix} \hat{i}_{\text{in}} \\ \hat{u}_{\text{o}} \end{bmatrix} = \begin{bmatrix} Y_{\text{in-o}} & T_{\text{oi-o}} + R_{\text{s2}}H_{\text{i}}G_{\text{a}}G_{\text{ci}} & G_{\text{a}}G_{\text{ci}} \\ G_{\text{io-o}} & -(Z_{\text{o-o}} - R_{\text{s2}}H_{\text{i}}G_{\text{a}}G_{\text{co}}) & G_{\text{a}}G_{\text{co}} \end{bmatrix} \begin{bmatrix} \hat{u}_{\text{in}} \\ \hat{i}_{\text{o}} \\ \hat{u}_{\text{ref}} \end{bmatrix} \tag{3.27}$$

Based on this dynamical representation, a condition for zero $Z_{\text{o-o}}^{\text{OCF}}$ is obtained. The required output-current-feedforward gain is given in (3.28), where the inductor current sensing gain G_{a} for the PCM-controlled converter is $1/R_{\text{s1}}$. Therefore, close to zero $Z_{\text{o-o}}^{\text{OCF}}$ can be achieved under the following conditions (Karppanen et al., 2007b):

- Unity gain output current feedforward (H_{i}=1)
- Equivalent current sensing resistors (R_{s1} for $i_{\text{L}} = R_{\text{s2}}$ for i_{o})

$$H_{\text{i}} = \frac{1}{R_{\text{s2}}G_{\text{a}}} \frac{Z_{\text{o-o}}}{G_{\text{co}}} \tag{3.28}$$

In (Karppanen et al., 2007b) the H_{i}=1 is chosen due to simple implementation and it is also shown that the mismatch of the two sensing resistors R_{s1} and R_{s2} adversely influences the $Z_{\text{o-o}}^{\text{OCF}}$ with the objective of obtaining zero output impedance. Based on the dynamical models of the PCM and OCF-controlled converters provided in Appendix G, the source-side special parameters are extracted according to the interactions formulation.

The ideal input impedance is the same as defined in (3.22) for all control methods. The input short-circuit impedance for the PCM is given in (3.29) and for the OCF in (3.30). The equivalent parameters U_{E} and r_{E} include the influence of the circuit parasitics and are defined in Appendix F.

$$Z_{\text{in-sco}}^{\mathrm{PCM}} = \frac{r_{\mathrm{E}} + F_{\mathrm{m}}^{\mathrm{PCM}} q_{\mathrm{c}}^{\mathrm{PCM}} U_{\mathrm{E}} + sL}{D(D - F_{\mathrm{m}}^{\mathrm{PCM}} q_{\mathrm{i}}^{\mathrm{PCM}} U_{\mathrm{E}}) - F_{\mathrm{m}}^{\mathrm{PCM}} q_{\mathrm{i}}^{\mathrm{PCM}} I_{\mathrm{o}} (r_{\mathrm{E}} + U_{\mathrm{E}} F_{\mathrm{m}}^{\mathrm{PCM}} q_{\mathrm{c}}^{\mathrm{PCM}} + sL)} \tag{3.29}$$

$$Z_{\text{in-sco}}^{\mathrm{OCF}} = \frac{r_{\mathrm{E}} + sL}{D(D - F_{\mathrm{m}}^{\mathrm{PCM}} q_{\mathrm{i}}^{\mathrm{PCM}} U_{\mathrm{E}}) - F_{\mathrm{m}}^{\mathrm{PCM}} q_{\mathrm{i}}^{\mathrm{PCM}} I_{\mathrm{o}} (r_{\mathrm{E}} + sL)} \tag{3.30}$$

The audiosusceptibility is nullified in PCM control by the design of the compensation ramp. This refers that the term D-F_{m}^{PCM} q_{i}^{PCM} U_{E} in (3.29) and (3.30) equals zero. As a consequence, both $Z_{\text{in-sco}}$'s are the same as the ideal input impedance (3.22) referring reduced source-side interactions sensitivity.

3.3.4 Load-side interactions formulation

The load-side special transfer functions are obtained for each control method applying the circuit-element based dynamical representations according to the interactions formulas (3.12)-(3.14). The ideal output impedance is given in (3.31) and it is obtained under the condition that the input-current feedback control is ideal. It characterizes constant power behavior at the output terminal under input-side feedback and is the same for every applied control method.

For the VM-controlled converter, the open-circuit output impedance $Z_{\text{o-oci}}^{\mathrm{o}}$ is defined in (3.32). It corresponds to the impedance of the output capacitor whereas the open-loop output impedance of the VM-controlled converter is the impedance of the power stage output filter as defined in Appendix F. The closed-loop $Z_{\text{o-oci}}^{\mathrm{c}}$ cannot be explicitly given based on the circuit elements due to its dependence on the state of feedback. However, it can be computed according to (3.33) based on the short-circuit input admittance, closed-loop input admittance and closed-loop output impedance for VM-controlled converter.

$$Z_{\text{o-}\infty} = \frac{\hat{u}_{\mathrm{o}}}{\hat{i}_{\mathrm{o}}}\Big|_{\hat{i}_{\mathrm{in}}=0, \hat{u}_{\mathrm{in}}=0} = \frac{1}{LC} \frac{(sL + (DU_{\mathrm{in}}/I_{\mathrm{o}}) + r_{\mathrm{L}} + r_{\mathrm{d}})(1 + sr_{\mathrm{c}}C)}{s^2 + s(r_{\mathrm{L}} + r_{\mathrm{d}} + r_{\mathrm{c}} + (DU_{\mathrm{in}}/I_{\mathrm{o}}))/L + 1/LC} \approx \frac{U_{\mathrm{o}}}{I_{\mathrm{o}}} (s = 0) \tag{3.31}$$

$$Z^{\mathrm{o}}_{\text{o-oci}} = \frac{\hat{u}_{\mathrm{o}}}{\hat{i}_{\mathrm{o}}}\Big|_{\hat{i}_{\mathrm{in}}=0,\hat{c}=0} = \frac{1+sr_{\mathrm{c}}C}{sC} \tag{3.32}$$

$$Z^{\mathrm{c}}_{\text{o-oci}} = \frac{\hat{u}_{\mathrm{o}}}{\hat{i}_{\mathrm{o}}}\Big|_{\hat{i}_{\mathrm{in}}=0,\hat{c}=0} = \frac{Z_{\text{o-c}}}{Y_{\text{in-c}}} Y_{\text{in-sco}} \tag{3.33}$$

For the other control methods, the open and the closed-loop open-circuit output impedance $Z_{\text{o-oci}}$ cannot be symbolically given based on the circuit elements due to their dependence on the state of the feedback. Therefore, these impedances can be most conveniently computed based on (3.33) using the defined closed-loop transfer functions and (3.34) where the internal transfer functions are obtained at open-loop.

$$Z^{\mathrm{o}}_{\text{o-oci}} = \frac{Z_{\text{o-o}}}{Y_{\text{in-o}}} Y_{\text{in-sco}} \tag{3.34}$$

As previously discussed, the IVFF, PCM and OCF all possess high input noise attenuation, which causes all the defined input-side impedances to be approximately the same. In the load-side interactions analysis this refers that in (3.33) and (3.34) the input admittances cancel each other. Therefore, the $Z_{\text{o-oci}}$ corresponds to the open-loop or closed-loop output impedance, respectively, implying to reduced load-side interactions sensitivity.

3.3.5 Experimental interconnected system

Experimental validation of the presented overall interaction analysis is provided based on an interconnected prototype system shown in Fig. 3.7, where the dc-dc converter is the prototype buck converter from Fig. 3.4 under different control schemes. The source-side interactions are assessed by designing a simple input filter so that the stability is guaranteed according to Middlebook's criterion. However, in order to better illustrate the interactions sensitivity, the robustness is slightly reduced by design. Thus the resulting component values are: $L_{\mathrm{F}} = 500\mu\mathrm{H}$, $r_{\mathrm{LF}} = 0.2\Omega$ and $C_{\mathrm{F}} = 200\mu\mathrm{F}$, $r_{\mathrm{CF}} = 45\mathrm{m}\Omega$. Correspondingly, the load-side interactions are assessed connecting an impedance load at the converter output terminal that emulates the behavior of a cascaded input filter of a downstream converter with the following parameter values: $L_{\mathrm{L}} = 230\mu\mathrm{H}$, $r_{\mathrm{LL}} = 0.1\Omega$, and $C_{\mathrm{L}} = 440\mu\mathrm{F}$, $r_{\mathrm{CL}} = 10\mathrm{m}\Omega$.

All measurements are obtained at the operating point with the lowest input voltage, 20V and full output power of 25W to maximize the source-side interactions. Based on the theoretical analysis, the most fundamental feature contributing on both source- and

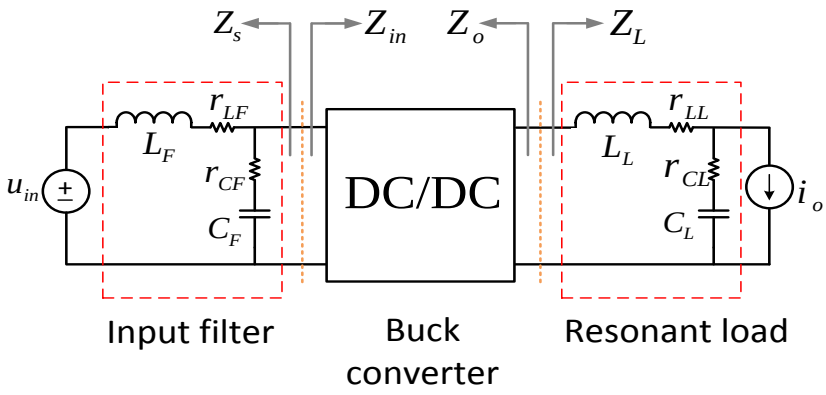

Fig. 3.7: Interconnected prototype system to demonstrate the source and load impedance interactions sensitivity.

load-side interactions is the input noise attenuation. The measured audiosusceptibility $G_{\text{io-o}}$ for each control method is shown in Fig. 3.8, where it can be observed that:

- VM-controlled converter has the worst $G_{\text{io-o}}$ with a high peak at the resonant frequency
- IVFF improves the $G_{\text{io-o}}$ of the VM converter, but the resonant behavior still causes reduction of the attenuation
- PCM and PCM-OCF inherently provide small $G_{\text{io-o}}$

The analytical circuit-element-based formulations are compared with the computed special parameters based on the measurements for the VM-controlled converter. Fig. 3.9 illustrates the computed input-side special impedances $Y_{\text{in-}\infty}$ (3.22) and $Y_{\text{in-sco}}$ (3.23) (solid lines) and the analytical ones (dashed lines). It can be observed that the analytical formulations do not provide perfect matching at the high frequencies, where the circuit parasitics begin to affect. Nevertheless, they give satisfactory results within the frequency range of interest. The ideal input impedance $Z_{\text{in-}\infty}$ is the same for all control methods, but the input short-circuit impedance $Z_{\text{in-sco}}$ varies depending on the applied control.

3.3.6 Experimental source-side analysis for VM and IVFF-controlled converter

The theoretical interaction analysis methodology is validated by analyzing the measured open and closed-loop input impedances as well as computed $Z_{\text{in-sco}}$ and the filter output

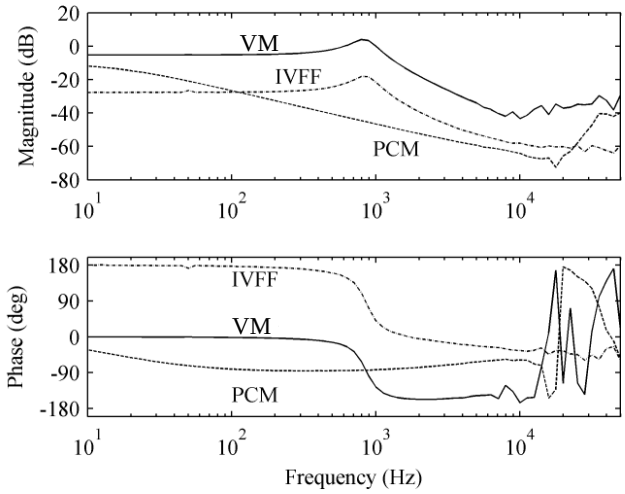

Fig. 3.8: Measured open-loop audiosusceptibilities at the input voltage of 20V.

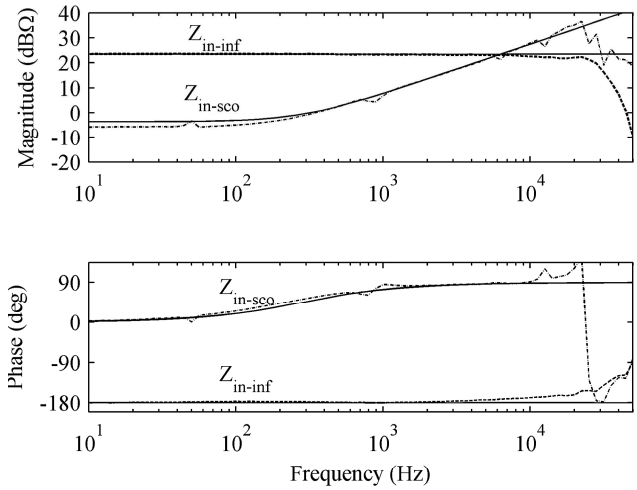

Fig. 3.9: Computed and analytical special input-side impedances $Z_{\text{in-}\infty}$ and $Z_{\text{in-sco}}$ for VM-controlled converter, where the solid line refers to the computed and dashed line to analytical.

impedance. These impedances are shown in Fig. 3.10 for the VM-controlled converter together with the filter output impedance Z_{s}. The $Z_{\text{in-sco}}$ is the lowest of the input impedances due to high $G_{\text{io-o}}$ and low $Z_{\text{o-o}}$ at low frequencies which contribute to this special parameter according to (3.9). From the figure it can be observed that:

- The filter output impedance Z_{s} intersects with the open-loop input impedance $Z_{\text{in-o}}$ thus referring that the output-voltage loop gain (3.16) is affected

- Z_{s} intersects with the input short-circuit impedance $Z_{\mathrm{in\text{-}sco}}$ referring that the output impedance (3.17) is affected
- Slightly reduced gain margin for the minor-loop gain $Z_{\mathrm{s}}Y_{\mathrm{in\text{-}c}}$ refers peaking in the corresponding sensitivity function

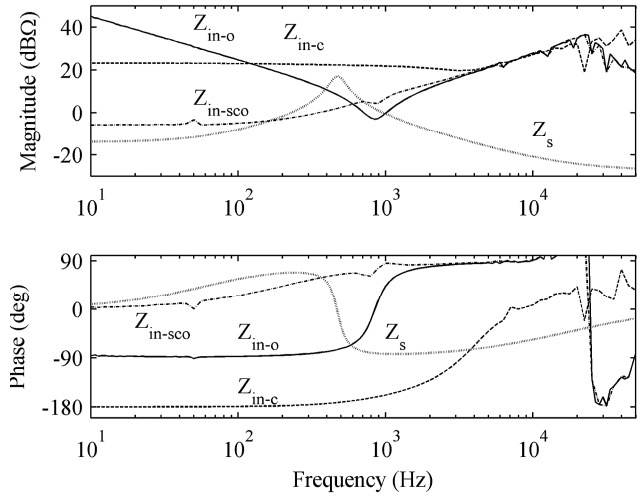

Fig. 3.10: Measured input-side impedances of the VM-controlled buck converter with the input filter output impedance Z_{s}.

The measured VM-converter output impedances, with (dashed line) and without (solid line) the input filter, are shown in Fig. 3.11 for open and closed-loop. The behavior of the measured source-affected output impedances is explained based on the previously discussed interactions phenomena:

- The peaking in $Z_{\mathrm{o\text{-}o}}$ (3.17) is consequence of the filter output impedance Z_{s} and the converter input-short circuit impedance $Z_{\mathrm{in\text{-}sco}}$ intersection
- The dipping in $Z_{\mathrm{o\text{-}o}}$ is caused by the intersection of the filter output impedance Z_{s} and the converter open-loop input impedance $Z_{\mathrm{in\text{-}o}}$
- The peaking in the closed-loop output impedance, $Z_{\mathrm{o\text{-}c}}$, is due to the intersection of Z_{s} and $Z_{\mathrm{in\text{-}sco}}$, together with peaking in the sensitivity function $1/(1+Z_{\mathrm{s}}Y_{\mathrm{in\text{-}c}})$

Based on the measured source-affected open and closed-loop output impedances, it can be observed that due to the intersection of the filter output impedance Z_{s} and the converter short-circuit input impedance $Z_{\mathrm{in\text{-}sco}}$, both $Z_{\mathrm{o\text{-}o}}$ and $Z_{\mathrm{o\text{-}c}}$ are affected. Therefore, it can be validated that the special parameter $Z_{\mathrm{in\text{-}sco}}$ is independent of the state

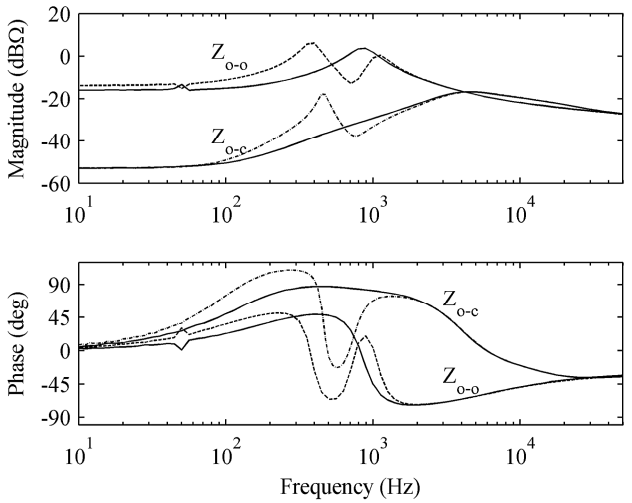

Fig. 3.11: Measured output impedances of the VM-controlled converter (solid lines: unaffected impedances without the filter, dashed line: the source-affected impedances with the filter).

of the feedback as previously discussed. In addition, it should be noted that the peaking in the closed-loop output impedance is clearly higher than in the open-loop output impedance due to the peaking in the minor-loop ($Z_{\mathrm{s}}Y_{\mathrm{in\text{-}c}}$)-based sensitivity function.

The measured input impedances of the IVFF-controlled converter are shown in Fig. 3.12 with the filter output impedance Z_{s}. It can be observed that not all input impedances are exactly equal as they would be if the audiosusceptibility is perfectly nullified. However, none of the impedances is intersecting with the Z_{s} and the condition $Z_{\mathrm{s}} < Z_{\mathrm{in\text{-}sco}}$ is complied with. Therefore, the converter output impedance remains unaltered by the addition of the input filter. It is clearly seen that the IVFF improves the interactions sensitivity of the VM-controlled converter. Additionally, it can be observed that the $Z^{IF}_{\mathrm{in\text{-}o}}$ exhibits negative-incremental-resistance property due to the applied feedforward as discussed earlier.

3.3.7 Experimental source-side analysis for PCM- and OCF-controlled converter

The output-current-feedforward affects only on Z_{o} and T_{oi}, and therefore, the open and closed-loop input impedances are the same for PCM and PCM-OCF controlled converters. However, the special parameter, $Y_{\mathrm{in\text{-}sco}} = Y_{\mathrm{in\text{-}o}} + G_{\mathrm{io\text{-}o}}T_{\mathrm{oi\text{-}o}}/Z_{\mathrm{o\text{-}o}}$, is influenced by this feedforward. It should be noted that in addition to small $G_{\mathrm{io\text{-}o}}$, the $Z_{\mathrm{o\text{-}o}}$ should be large enough in order to have all the input side admittances equal.

The measured and computed input impedances are shown in Fig. 3.13, where it can

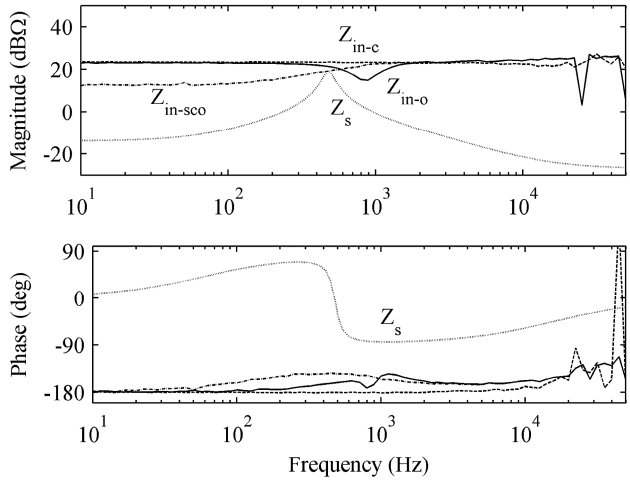

Fig. 3.12: Measured input-side impedances of the IVFF-controlled buck converter with the input filter output impedance.

be observed that:

- For PCM all the input-side impedances are essentially equal explaining the invariance to the source-side interactions
- $Z_{\text{in-sco}}^{OCF}$ is reduced due to lower $Z_{\text{o-o}}^{OCF}$ as a comparison to the PCM converter and thus making it more sensitive to the input filter interactions

Even if the inductor-current-loop compensation is impossible to be designed so that the audiosusceptibility is perfectly nullified, $Z_{\text{in-sco}}^{PCM}$ is not similarly affected as in the case of IVFF $Z_{\text{in-sco}}^{IF}$. This is due to higher open-loop output impedance as a comparison to input-voltage or output-current-feedforward controlled converters. From Fig. 3.13, minor intersection can be observed between the filter output impedance, Z_{s}, and input short-circuit impedance $Z_{\text{in-sco}}^{OCF}$ of the OCF controlled converter, and therefore, its output impedances would be slightly affected.

The measured open and closed-loop output impedances for the OCF converter are shown in Fig. 3.14. The dotted lines are the original open and closed-loop output impedances without the input filter whereas the solid and dashed lines are the original open and closed-loop output impedances. It can be observed that for both measured Z_{o} with the input filter, the resonant peaking is the same. This peaking is due to the intersection of $Z_{\text{in-sco}}^{OCF}$ and the filter output impedance implying that the peaking in the sensitivity function is not influencing the OCF converter in a similar way than the VM-converter. Nevertheless, the resonant behavior at the output impedance is so insignificant

that it does not affect the load-transient performance.

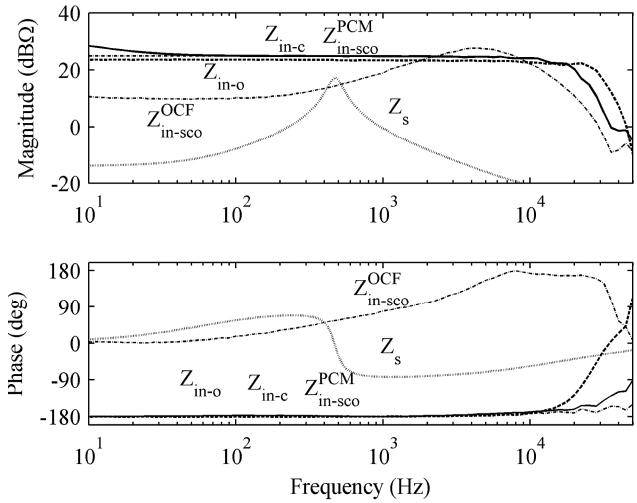

Fig. 3.13: Measured input impedances of the PCM and PCM-OCF-controlled converters with the input filter output impedance.

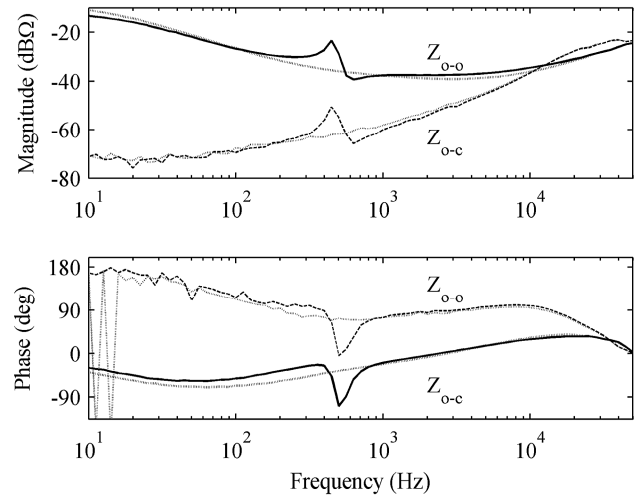

Fig. 3.14: Measured open and closed-loop output impedances of the PCM-OCF-controlled converter, where the dotted lines represent the original open and closed-loop output impedances without the filter and the solid and dashed lines are the output impedances with the filter.

3.3.8 Experimental load-side interactions analysis for VM-controlled converter

The load-side interactions sensitivity is assessed based on the computed special parameters ($Z_{\text{o-}\infty}$ $Z^{o}_{\text{o-oci}}$, $Z^{c}_{\text{o-oci}}$). These impedances are shown in Fig. 3.15 for the VM-controlled converter together with the load impedance Z_{L}. As discussed in the theoretical analysis and based on the figure it can be observed that:

- Open-loop $Z^{o}_{\text{o-oci}}$ is the impedance of the output capacitor (3.32)
- $Z_{\text{o-}\infty}$has a property of a resistance at low frequency depicting constant-power nature
- The load impedance Z_{L} intersects with all output-side impedances expect the $Z_{\text{o-c}}$

The overlapping of the Z_{L} and the open-loop output impedance indicates that the loop-gain is altered (3.18), whereas the intersection of the Z_{L} and the open and closed-loop $Z_{\text{o-oci}}$ indicates that the converter input impedance is influenced (3.19). The load-affected input impedances are shown in Fig. 3.16 with the filter output impedance, Z_{s}. It is clearly seen that both impedances are affected by the resonant load as a comparison to Fig. 3.10.

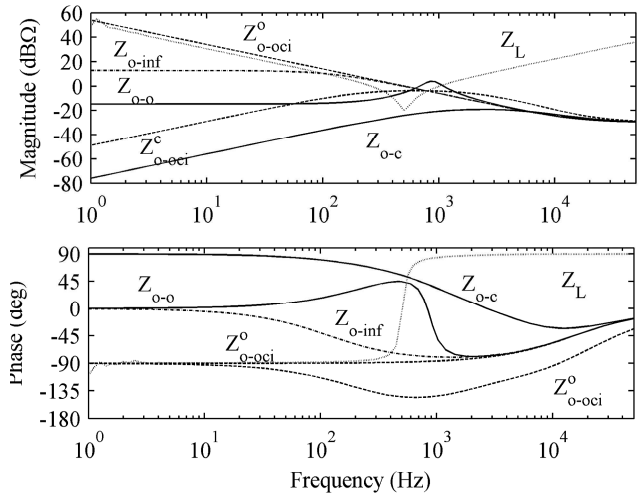

Fig. 3.15: Output impedances of the VM-controlled converter and the input impedance of the cascaded series resonant LC-circuit, Z_{L}.

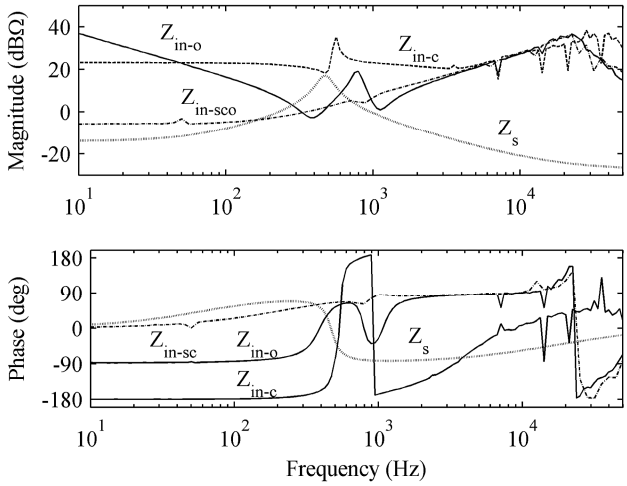

Fig. 3.16: Measured load-affected input impedances of the VM-controlled converter with the input filter output impedance.

3.3.9 Simultaneous source and load-side interactions analysis for VM-controlled converter

Simultaneous source and load-side interactions can make the VM-controlled converter close to instability. If the input filter is connected to the load-affected converter, from Fig. 3.16 it can be observed that load-affected $Z_{\text{in-c}}$ is close to intersect with the filter output impedance as a comparison to Fig. 3.10 thus indicating reduced robustness. The stability of this interconnected system is assessed based on source and load-side minor-loop gains:

- Source-side minor-loop gain (ML^S_{LC}) formed between the load-affected input impedance and Z_{s}
- Load-side minor-loop gain (ML^L_{LC}) based on the source-affected output impedance and Z_{L}

These minor-loop gains are shown in Fig. 3.17 as Nyquist plots, where the subscript 'LC' means that both of the resonant circuits affect the converter simultaneously. The input-side minor-loop gain contains 40 data points/decade and the output side contains only 20 data points/decade reducing the resolution of the Nyquist plot information. Nevertheless, from these plots it can be observed that both minor-loop gains equally indicate that the system is stable. However, the robustness information is different because the source-side sensitivity function describes the filter influences on the converter dynamics

and correspondingly the load side sensitivity function illustrates the load influence.

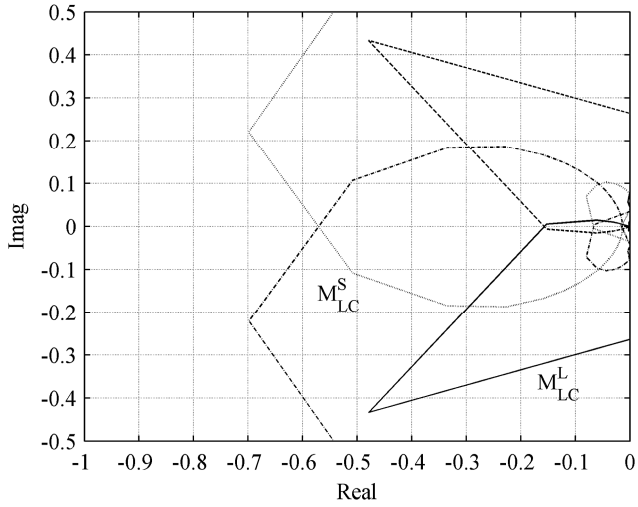

Fig. 3.17: Measured source and load-side minor-loop gains, where the subscript 'LC' refers that both of the resonant circuits affect the converter simultaneously.

The simultaneous influence of the source and load- impedances on the converter dynamics is best observed in time domain by applying a load step. The output voltage response is shown in Fig. 3.18, where the plot a) represents the original response and b) is the response with the filter. These two plots have the same time scaling. However, in order to better observe the performance degradation different time-scale is used in c) and d), where c)corresponds to plot b) and d) is obtained including both, the filter and the resonant load. Based on these output-voltage responses at different combinations of the source and load-side impedances it can be observed that:

- The initial dip in the output voltage remains unaltered despite the changes in the output impedance
- Settling time is influenced by the addition of the input filter, due to the resonance occurring within the control bandwidth of the source-affected $Z_{\text{o-c}}$ in Fig. 3.11
- Simultaneous effect of the source and load impedances results in prolonged decaying oscillation Fig. 3.18 d)

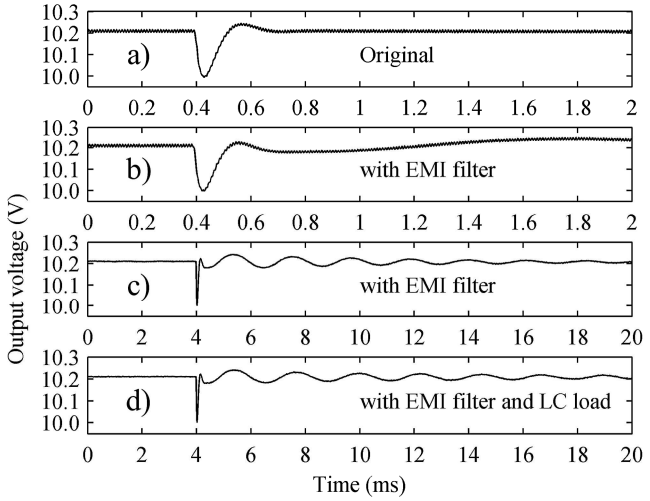

Fig. 3.18: The measured output-voltage responses to the load change from 0.2A to 2.5A (250mA/μs) at different combinations of the source and load-side impedances.

3.3.10 Experimental load-side analysis for converters with high input noise attenuation

For IVFF, PCM, and PCM-OCF controlled converters, the input noise attenuation is high, as discussed previously and shown in Fig. 3.8. For the load-side interactions this refers that:

- All input impedances are essentially equal and, according to (3.33) and (3.34), they cancel each other

- The special load-side parameters $Z^o_{\text{o-oci}}$ and $Z^c_{\text{o-oci}}$ correspond to the open and closed loop output impedances, respectively

The measured open and closed-loop output impedances as well as the special load-side parameters $Z^o_{\text{o-oci}}$ and $Z^c_{\text{o-oci}}$ are shown in Fig. 3.19 for the IVFF-controlled converter. It can be observed that $Z^o_{\text{o-oci}}$ and $Z^c_{\text{o-oci}}$ are essentially same than the open and closed-loop output impedances. The output-side impedances of the PCM and PCM-OCF converter behave in the same way as for the IVFF converter, shown in Fig. 3.19 due to low $G_{\text{io-o}}$. Therefore, it can be concluded that a converter with high input noise attenuation prevents also the load impedance from interacting with the input impedance.

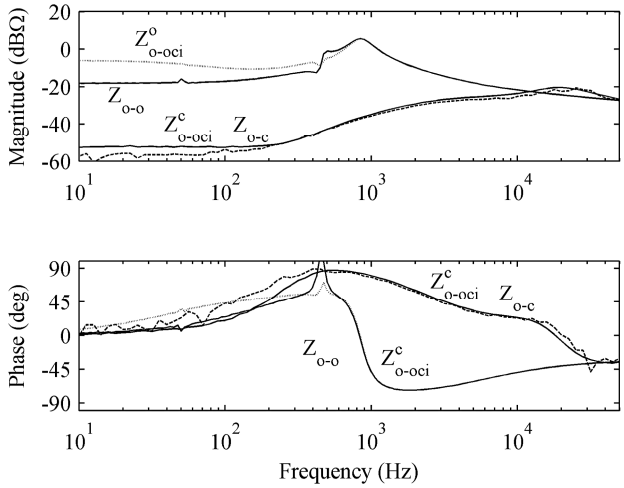

Fig. 3.19: Measured open- (dotted line) and closed- loop output impedances (solid line) for the IVFF converter.

3.3.11 Interactions characterization of commercial converters

In case the internal converter structure and the control method are known, the interactions sensitivity can be assessed based on circuit-element-based equations. However, for commercial converters only four closed-loop transfer functions are measurable, based on which the special parameters $Z_{\text{in-sco}}$ and $Z_{\text{o-oci}}$ characterizing the interactions sensitivity, can be computed.

These special parameters are extracted for two commercial power modules M3 (Tracopower, 2009) and M2 (TexasInstruments, 2000). The measurements were performed at 12V input for both converters with the output current of 1A for M3 and 1.5A for M2. The input-side impedances $Z_{\text{in-c}}$ and $Z_{\text{in-sco}}$ as well as the output-side impedances $Z_{\text{o-c}}$ and $Z_{\text{o-oci}}$ are shown for both converters in Fig. 3.20 and Fig. 3.21. Based on these plotted special parameters, it can be observed that:

- For M3, both the input and the output-side impedances are equal
- For M2, both source and load-side special parameters indicate increased interactions sensitivity

Therefore, without knowing the internal structure or the applied control method, it can be concluded that the second converter M2 is more sensitive to the source and load-side interactions.

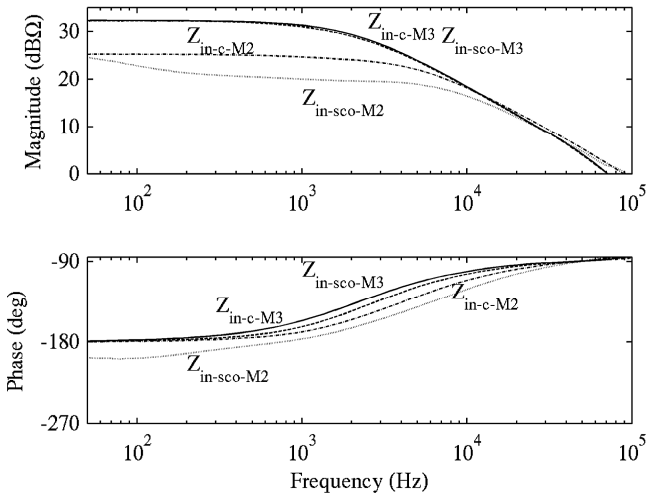

Fig. 3.20: The measured input-side impedances and computed $Z_{\text{in-sco}}$'s of the commercial M3 and M2 modules.

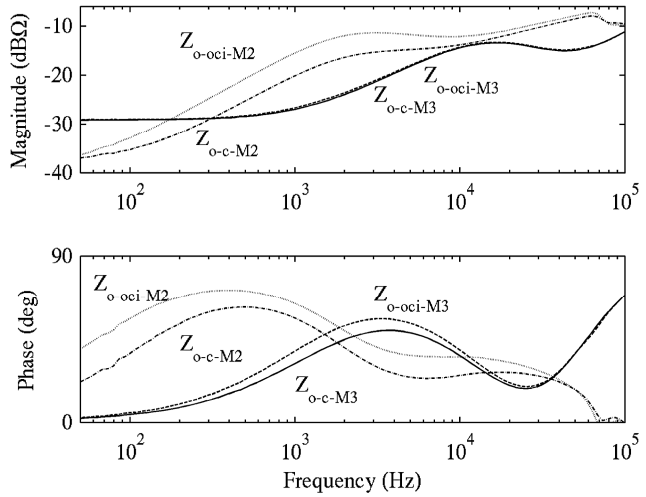

Fig. 3.21: The measured output-side impedances and computed $Z_{\text{o-oci}}$'s of the M3 and M2 modules.

3.4 System-level interactions

This section focuses on system-level interactions analysis based on commercial converters. The coupling methods are assessed in this thesis for a system structure of input-parallel-connected converters with a common input filter using system-level interactions

formulation presented in (Vesti et al., 2012, 2011). The constructed model introduces cross-coupling mechanisms which may deteriorate the system performance.

The distributed system is typically divided into smaller and manageable subsystems, which are analyzed individually. In this section, a subsystem consisting of two converters sharing an input filter, illustrated in Fig. 3.22, is analyzed. First, the theoretical formulation is extracted utilizing the two-port modeling approach for obtaining the special parameters to characterize the interactions within the system. It is shown that several mechanisms, possibly leading to deteriorated load-transient behavior or even instability, exist within the system. It depends on the converter dynamics whether the interactions couple through the system. Finally, an experimental system is used to validate the presented theoretical analysis.

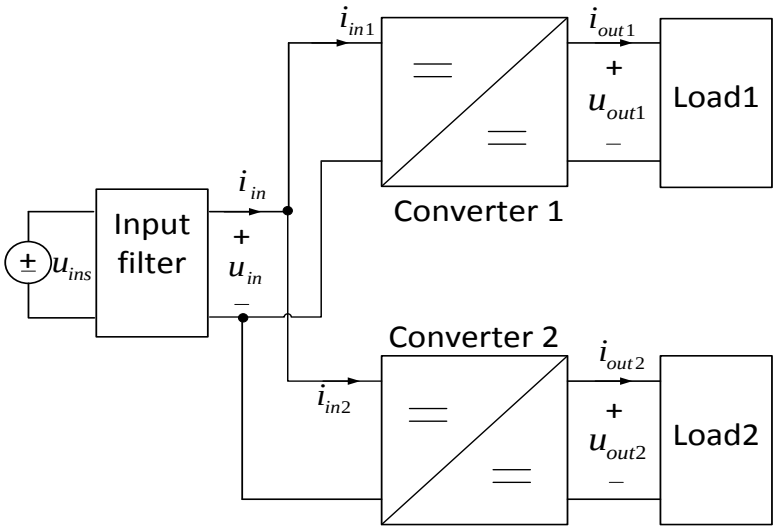

Fig. 3.22: Input-parallel connected system structure.

3.4.1 Dynamical system model

The dynamical model of the system is obtained by representing the dc-dc converters as their closed-loop two-port model and the input filter by its output impedance denoted as Z_s for the theoretical analysis. The resulting system structure is shown in Fig. 3.23. The dashed line corresponds to the internal dynamics of the input-parallel connected converters given in (3.35) while the source and both loads are assumed ideal. From the internal dynamic representation the following observations can be made:

- The additional terms G_{cr1} and G_{cr2} illustrate the cross-coupling mechanism between the converters due to the common source impedance and they equal zero

when the source is ideal (3.35)

- The system input current is the sum of the converter input currents
- The input admittance is the sum of the converter input admittances

In this system analysis, no parasitics due to the system interconnection are considered thus only one interface exists to assess the source-side robustness of the converters.

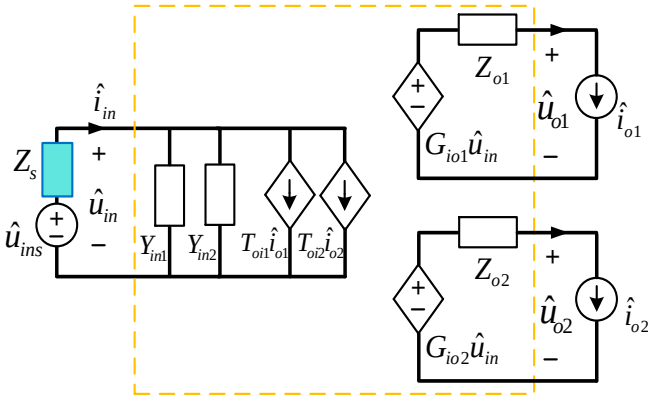

Fig. 3.23: Linear model of the input-parallel connected converters with the input filter.

$$\begin{bmatrix} \hat{i}_{\text{in}} \\ \hat{u}_{\text{o1}} \\ \hat{u}_{\text{o2}} \end{bmatrix} = \begin{bmatrix} Y_{\text{in}} & T_{\text{oi1}} & T_{\text{oi2}} \\ G_{\text{io1}} & -Z_{\text{o1}} & G_{\text{cr1}}=0 \\ G_{\text{io2}} & G_{\text{cr2}}=0 & -Z_{\text{o2}} \end{bmatrix} \begin{bmatrix} \hat{u}_{\text{in}} \\ \hat{i}_{\text{o1}} \\ \hat{i}_{\text{o2}} \end{bmatrix} \tag{3.35}$$

The source and load impedance influence to the system dynamics is analyzed in a similar way as for an individual converter. The source-affected system-level dynamics is given in (3.36) and the detailed derivation is provided in Appendix H. The special parameters describing the source-side interactions, $Y^s_{\text{in-sco1}}$ and $Y^s_{\text{in-sco2}}$ for both converters are defined in (3.37) and (3.38) where the subscript 's' denotes source-affected.

$$\begin{bmatrix} \hat{i}_{\text{in}} \\ \hat{u}_{\text{o1}} \\ \hat{u}_{\text{o2}} \end{bmatrix} = \begin{bmatrix} \frac{Y_{\text{in}}}{1+Z_{\text{s}}Y_{\text{in}}} & \frac{T_{\text{oi1}}}{1+Z_{\text{s}}Y_{\text{in}}} & \frac{T_{\text{oi2}}}{1+Z_{\text{s}}Y_{\text{in}}} \\ \frac{G_{\text{io1}}}{1+Z_{\text{s}}Y_{\text{in}}} & -\frac{1+Z_{\text{s}}Y^{\text{S}}_{\text{in-sco1}}}{1+Z_{\text{s}}Y_{\text{in}}}Z_{\text{o1}} & -\frac{G_{\text{io1}}T_{\text{oi2}}Z_{\text{s}}}{1+Z_{\text{s}}Y_{\text{in}}} \\ \frac{G_{\text{io2}}}{1+Z_{\text{s}}Y_{\text{in}}} & -\frac{G_{\text{io2}}T_{\text{oi1}}Z_{\text{s}}}{1+Z_{\text{s}}Y_{\text{in}}} & -\frac{1+Z_{\text{s}}Y^{\text{S}}_{\text{in-sco2}}}{1+Z_{\text{s}}Y_{\text{in}}}Z_{\text{o2}} \end{bmatrix} \begin{bmatrix} \hat{u}_{\text{ins}} \\ \hat{i}_{\text{o1}} \\ \hat{i}_{\text{o2}} \end{bmatrix} \tag{3.36}$$

$$Y^{\mathrm{S}}_{\text{in-sco1}} = \frac{\hat{i}_{\text{in}}}{\hat{u}_{\text{in}}}|_{\hat{i}_{\text{o1}}=0,\hat{i}_{\text{o2}}=0} = Y_{\text{in-sco1}} + Y_{\text{in2}} \tag{3.37}$$

$$Y^{\mathrm{S}}_{\text{in-sco2}} = \frac{\hat{i}_{\text{in}}}{\hat{u}_{\text{in}}}|_{\hat{i}_{\text{o1}}=0,\hat{i}_{\text{o2}}=0} = Y_{\text{in-sco2}} + Y_{\text{in1}} \tag{3.38}$$

The original $Y_{\text{in-sco1}}$ and $Y_{\text{in-sco2}}$ are obtained individually according to (3.9). From these source-affected formulas, (3.37) and (3.38), it can be observed that the magnitude of the corresponding source-affected $Z^{\mathrm{S}}_{\text{in-sco}}$ would be lower than the individual $Z_{\text{in-sco}}$ and thus the source-side interactions sensitivity is slightly increased.

The load affected system dynamics is obtained in a similar way as for an individual converter. However, due to the system structure the load impedance influences the overall system input impedance. Due to the input filter, the transfer functions are source-affected and the influence of the load Y_{L1} at the Converter 1 output to the system, is given in (3.39) and derived in detail in Appendix I. The special parameter describing the load-side interactions sensitivity of the Converter 1 is given in (3.40).

$$\begin{bmatrix} \hat{i}_{\text{in}} \\ \hat{u}_{\text{o1}} \\ \hat{u}_{\text{o2}} \end{bmatrix} = \begin{bmatrix} \frac{1+Z^{\mathrm{S}}_{\text{o-oci1}}Y_{\text{L1}}}{1+Z^{\mathrm{S}}_{\text{o1}}Y_{\text{L1}}}Y^{\mathrm{S}}_{\text{in1}} + Y^{\mathrm{S}}_{\text{in2}} & \frac{T^{\mathrm{S}}_{\text{oi1}}}{1+Z^{\mathrm{S}}_{\text{o1}}Y_{\text{L1}}} & \frac{Y_{\text{L1}}G^{\mathrm{S}}_{\text{cr1}}T^{\mathrm{S}}_{\text{oi1}}}{1+Z^{\mathrm{S}}_{\text{o1}}Y_{\text{L1}}} + T^{\mathrm{S}}_{\text{oi2}} \\ \frac{G^{\mathrm{S}}_{\text{io1}}}{1+Z^{\mathrm{S}}_{\text{o1}}Y_{\text{L1}}} & -\frac{Z^{\mathrm{S}}_{\text{o1}}}{1+Z_{\text{o1}}Y_{\text{L1}}} & \frac{G_{\text{cr1}}}{1+Z^{\mathrm{S}}_{\text{o1}}Y_{\text{L1}}} \\ G^{\mathrm{S}}_{\text{io2}} + \frac{Y_{\text{L1}}G^{\mathrm{S}}_{\text{io1}}G^{\mathrm{S}}_{\text{cr2}}}{1+Z^{\mathrm{S}}_{\text{o1}}Y_{\text{L1}}} & \frac{G^{\mathrm{S}}_{\text{cr2}}}{1+Z^{\mathrm{S}}_{\text{o1}}Y_{\text{L1}}} & -(Z^{\mathrm{S}}_{\text{o2}}\frac{Y_{\text{L1}}G^{\mathrm{S}}_{\text{cr1}}G^{\mathrm{S}}_{\text{cr2}}}{1+Z^{\mathrm{S}}_{\text{o1}}Y_{\text{L1}}}) \end{bmatrix} \begin{bmatrix} \hat{u}_{\text{ins}} \\ \hat{j}_{\text{o1}} \\ \hat{i}_{\text{o2}} \end{bmatrix} \tag{3.39}$$

$$Z^{\mathrm{S}}_{\text{o-oci1}} = \frac{\hat{u}_{\text{o1}}}{\hat{i}_{\text{o1}}}|_{\hat{u}_{\text{in}}=0,\hat{i}_{\text{o2}}=0} = Z^{\mathrm{S}}_{\text{o1}} + \frac{G^{\mathrm{S}}_{\text{io1}}T^{\mathrm{S}}_{\text{oi1}}}{Y^{\mathrm{S}}_{\text{in1}}} \tag{3.40}$$

This system-level representation considers the combined effects of the source and load impedances. It can be observed that the transient response could be significantly influenced depending on the design of the input filter and the type of the load impedance. Due to cross-coupling, the output impedance $Z_{\text{o-2}}$ might be altered by the load impedance at the Converter 1 output. Correspondingly, the effect of the load Y_{L2} at the output of Converter 2 is obtained in a similar way and derived in Appendix I.

3.4.2 Practical system characterization

As discussed in the previous section, control methods such as PCM control with high input noise attenuation, would also reduce the cross-coupling within the system and as a consequence operate as a dynamic buffer (Vesti et al., 2011). However, as shown earlier,

the VM-controlled converter is sensitive to both source and load-side interactions due to its poor input noise attenuation. Therefore, in order to demonstrate the coupling method within the system, the converters utilized to form the described system structure are both VM-controlled. The first converter is a commercial power module PMB 8518T (EricssonPowerModules, 2011) with the switching frequency of 300kHz and the second converter is a designed DSP-controlled buck converter treated as a commercial converter with switching frequency of 100kHz.

The system input filter is designed so that the Middlebrook's criterion for stability is met. The corresponding component values for this single stage filter are: $L_{\mathrm{F}} = 200\mu\mathrm{H}$ and $C_{\mathrm{F}} = 470\mu\mathrm{F}$ and the measured output impedance is denoted as Z_{o}. The load-side interactions are assessed by connecting an LC resonant circuit: $L_{\mathrm{LC}} = 28\mu\mathrm{H}$, $C_{\mathrm{LC}} = 3\mathrm{mF}$, at the output terminal of a converter. This resonant load emulates the input filter of a downstream-connected converter and the measured input impedance is denoted as $Z_{\text{in-LC}}$. The first step in the system interactions sensitivity analysis is to characterize both converters by measuring the four closed-loop transfer functions at the following operating point:

- PMB: Uin = 12V, Io = 5A and Uo = 3.3V
- DSP: Uin = 12V, Io = 1A and Uo = 5V

As discussed previously, high input noise attenuation is the most decisive dynamical feature of a converter contributing on the interactions sensitivity. The measured G_{io}'s from both converters are shown in Fig. 3.24. It can be observed that the PMB converter has higher input noise attenuation at the relevant frequencies from 100Hz to 10kHz thus indicating reduced sensitive to the impedance-based interactions as a comparison with the DSP converter.

3.4.3 Interactions sensitivity to external impedances

The interactions sensitivity is assessed by computing the special parameters based on the measurements according to the presented system-level formulation. Buck converters require a discrete input capacitor at the input terminal for proper operation and typically these capacitors are small for the point-of-load converters. However, the converters utilized for this analysis have relatively large input capacitors (DSP: $147\mu\mathrm{F}$, PMB: $28\mu\mathrm{F}$) and they influence on the input impedance measurements. Their effect can be removed by measuring the input impedance while the converter is inoperable obtaining the capacitor frequency response and thus the original input impedances can be extracted. The effect of the input capacitors is then added to the filter output impedance, slightly reducing the resonant frequency of the filter.

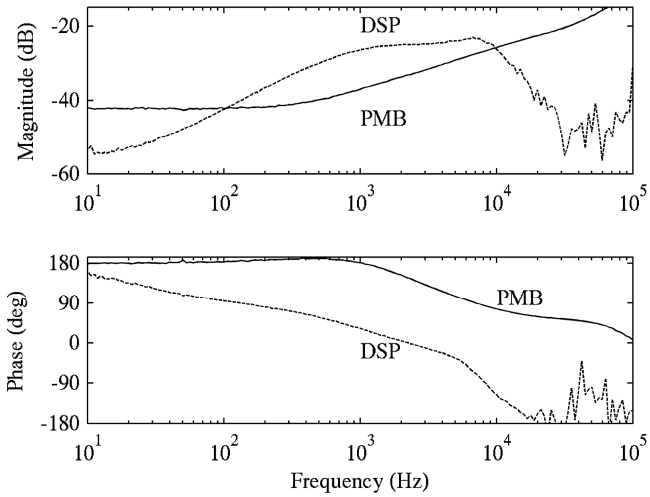

Fig. 3.24: The measured audiosusceptibility Gio of both converters.

Source-side sensitivity

The sensitivity to the filter interactions of both converters within the described system structure is assessed based on the source-affected $Z^{\mathrm{S}}_{\text{in-sco}}$ according to (3.37). The computed original and source-affected special parameters are shown in Fig. 3.25 and Fig. 3.26 for the PMB and DSP converters, respectively, together with the measured input impedances and the filter output impedance. The solid line in both figures is the source-affected input short-circuit impedance, the dashed line is the original input short-circuit impedance and the dotted line is the closed-loop input impedance. It can be observed that for both converters the magnitude of $Z^{s}_{\text{in-sco}}$ is lower than original $Z_{\text{in-sco}}$ thus slightly increasing the source-side interactions sensitivity. DSP $Z^{s}_{\text{in-sco}}$ is overlapping with the filter output impedance thus implying that the DSP converter output impedance would be affected by the system.

Load-side sensitivity

The load impedance influence to the converter input dynamics is first assessed individually and then on the system-level. The computed open-circuit output impedance (3.40) and the measured output impedance for both converters are shown in Fig. 3.27 and Fig. 3.28 for PMB and DSP converters, respectively, together with the input impedance of the LC resonant circuit. From these figures, it can be observed that:

- The PMB converter is clearly less sensitive to the load impedance and its Z_{in} remains unaltered

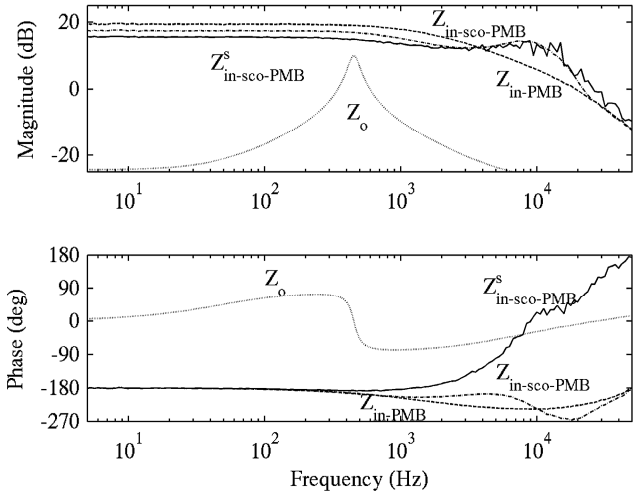

Fig. 3.25: The measured input impedance $Z_{\text{in-PMB}}$ (dotted line), source-affected short-circuit input impedance $Z^s_{\text{in-sco-PMB}}$ (solid line), original $Z_{\text{in-sco-PMB}}$ (dashed line) and the filter output impedance Z_{o}.

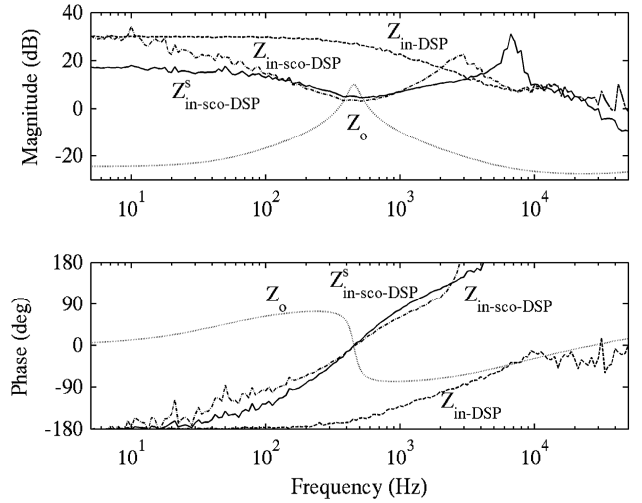

Fig. 3.26: The measured input impedance $Z_{\text{in-DSP}}$ (dotted line), source-affected short-circuit input impedance $Z^s_{\text{in-sco-DSP}}$ (solid line), original $Z_{\text{in-sco-DSP}}$ (dashed line) and the filter output impedance Z_{o}.

- DSP $Z_{\text{o-oci}}$ intersects with the load impedance referring to altered input dynamics

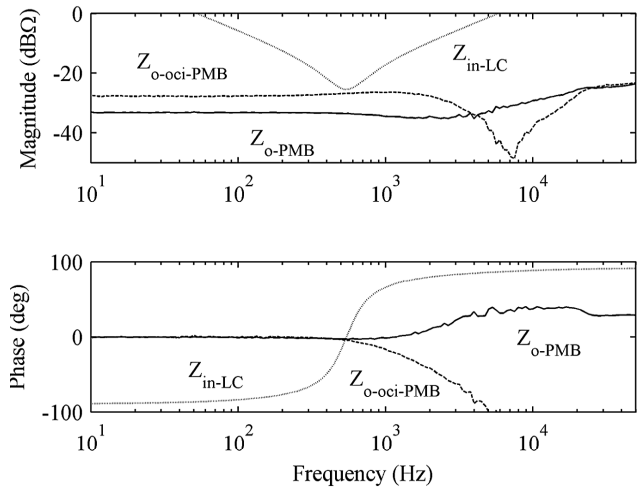

Fig. 3.27: The measured output impedance (solid line) and computed open-circuit output impedance (dashed line) of the PMB converter vs. the resonant load impedance (dotted line).

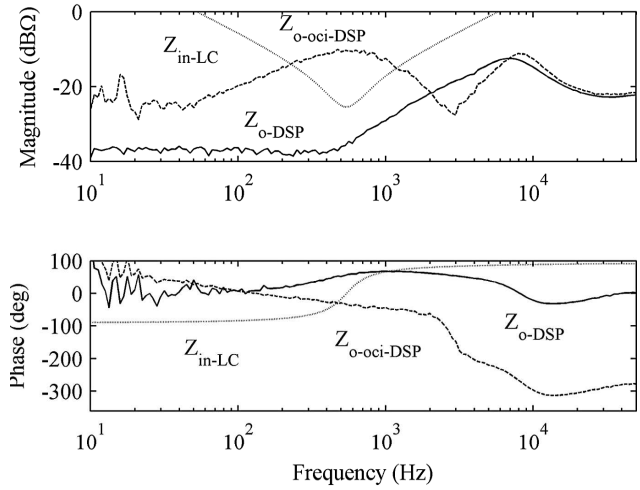

Fig. 3.28: The measured output impedance (solid line) and computed open-circuit output impedance (dashed line) of the DSP converter vs. the resonant load impedance (dotted line).

3.4.4 System dynamics

The conclusions drawn based on the converter characterization and the theoretical formulations are validated by assessing the overall system performance. The converter performance in the described system might be degraded due to the altered internal dynamics

or through the cross-coupling mechanism. In this subsection they are both assessed.

Based on the prior analysis, the DSP converter output as well as the input impedances are influenced by the external impedances whereas the PMB converter dynamics remains unaltered. The DSP converter Z_{o} is measured while the input filter is connected and the load is a current source. The measured original (solid line) and source-affected (dashed line) output impedances are shown in Fig. 3.29, thus verifying the conclusion from the prior source-side interactions sensitivity analysis. This refers that the load transient performance might be slightly influenced by the altered Z_{o}.

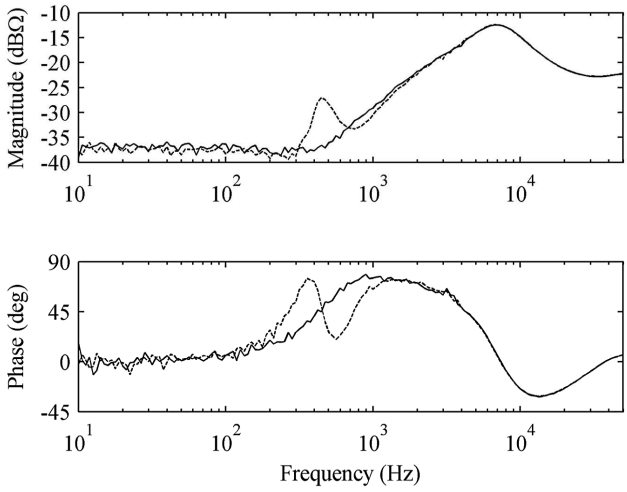

Fig. 3.29: The measured output impedances of the DSP converter without the input filter (solid line) and with it (dashed line).

Correspondingly, the load impedance influence on the system input impedance can be observed from Fig. 3.30, where the following impedances are shown:

- Original system input impedance (solid line)
- Z_{in} when the resonant load is connected at the PMB converter output (dashed line, PMB-LC)
- Z_{in} when the resonant load is connected at the DSP converter output (dash dotted line, DSP-LC)
- Filter output impedance $Z_{\text{o-LC}}$ (dotted line)

As predicted, the resonant load has insignificant impact on the input impedance while connected at the output of the PMB converter. However, due to the intersection

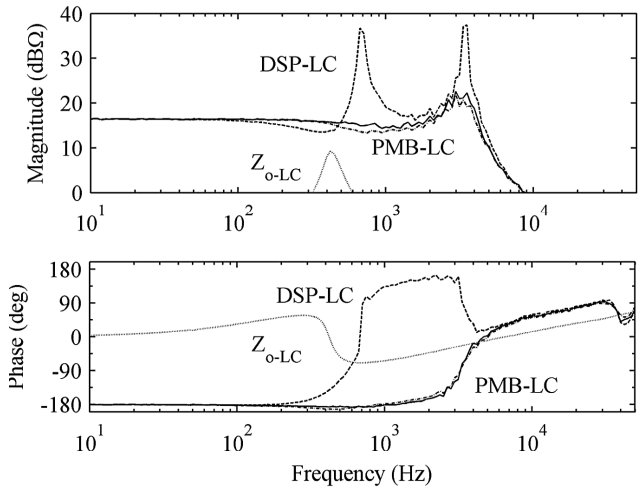

Fig. 3.30: Measured system input impedances: original (solid line), load at the DSP output DSP-LC (dashed line) and load at the PMB output PMB-LC (dash-dotted line).

of the DSP open-circuit output impedance $Z_{\text{o-oci-DSP}}$ and the load impedance $Z_{\text{in-LC}}$, the system input voltage is clearly altered when the load is connected at the output of the DSP converter. Nevertheless, as it can be observed from Fig. 3.30 the altered input impedance is not overlapping with the output impedance $Z_{\text{o-LC}}$ of the filter guaranteeing sufficient margin for stability. Therefore, the system stability is not endangered.

3.4.5 Cross-coupling within the system

In addition to the dynamical changes in the internal transfer functions, the system performance could be degraded due to cross-coupling through the common input impedance. In order to better illustrate this cross-coupling mechanism, only the source-affected system is considered and both loads are assumed as ideal current sources.

According to the source-affected system-level formulation (3.39), the output voltage of the DSP converter can be expressed as (3.41).

$$\hat{u}_{\text{o-DSP}} = \frac{G_{\text{io}}^{\text{DSP}}}{1 + Z_{\text{s}} Y_{\text{in}}} \hat{u}_{\text{ins}} - \frac{G_{\text{io}}^{\text{DSP}} T_{\text{oi}}^{\text{PMB}} Z_{\text{s}}}{1 + Z_{\text{s}} Y_{\text{in}}} \hat{i}_{\text{o}}^{\text{PMB}} - \frac{1 + Z_{\text{s}} Y_{\text{in-sco}}^{\text{S-DSP}}}{1 + Z_{\text{s}} Y_{\text{in}}} Z_{\text{o}}^{\text{DSP}} \hat{i}_{\text{o}}^{\text{DSP}} \tag{3.41}$$

From this output voltage expression, it can be observed that the DSP output voltage might be affected due to:

- Peaking in the minor-loop gain based sensitivity function, formed between the output impedance of the filter denoted as Z_{s} in the theoretical analysis and the

input admittance Y_{in} of the overall system

- Intersection between the filter output impedance Z_{s} and the source-affected input short-circuit impedance $Z_{\text{in-sco}}^{\text{S-DSP}}$
- Changes in the PMB converter output current $i_{\text{o}}^{\text{PMB}}$ if the cross-coupling impedance $(G_{\text{io}}^{\text{DSP}} T_{\text{oi}}^{\text{PMB}} Z_{\text{s}})/(1+Z_{\text{s}}Y_{\text{in}})$ is large

The cross-coupling impedance, shown in Fig. 3.31, is measured by introducing a perturbation in the PMB load current and measuring the output voltage of the DSP converter. It can be seen that this impedance is small in magnitude but contains a resonance at the filter resonant frequency. Therefore, the output voltage of the DSP converter might slightly affected while a load transient is applied at the PMB converter output.

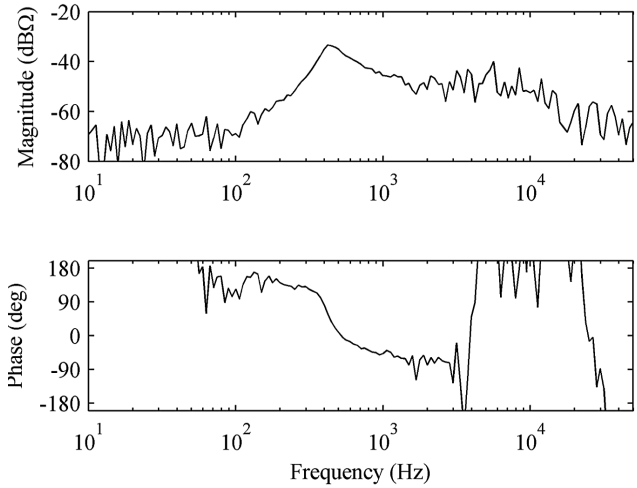

Fig. 3.31: The measured cross-coupling impedance from the output of the PMB converter to the output of the DSP converter.

The system cross-coupling phenomena is best observed in time-domain while introducing a load step at the output of the PMB converter. The output voltages of both converters to this load step are illustrated in Fig. 3.32 while the input filter is connected at the system input. It can be observed that the output voltage of the DSP converter is deviated due to this transient applied to the PMB converter as a comparison to the original response, shown in Fig. 3.33, which is obtained with ideal source impedance. Thus, the conclusions based on the theoretical analysis are confirmed. The cross-coupling can be critical especially within systems where one converter is supplying a pulsating load and the other converter feeds a sensitive load that requires extremely stable supply voltage.

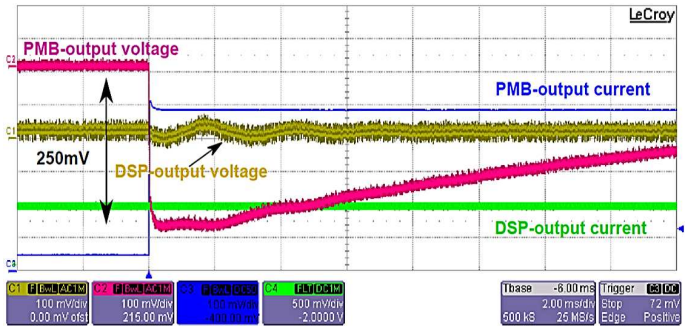

Fig. 3.32: The measured transient behavior of the output voltage of the DSP converter when the output current of the PMB converter is changed from 0.5A to 5A, while the input filter is connected (Current: 1A/div, Voltage: 100mV/div, Time: 2ms/div).

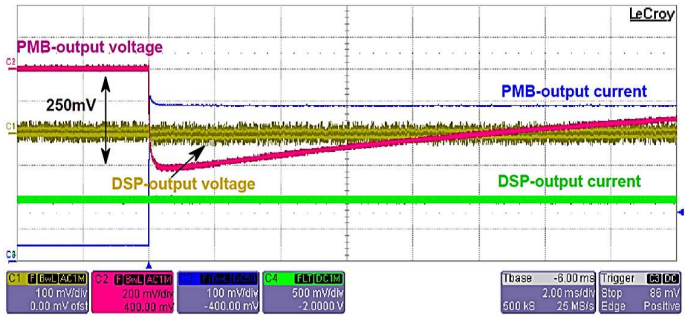

Fig. 3.33: The measured transient behavior of the output voltage of the DSP converter when the output current of the PMB converter is changed from 0.5A to 5A, without the input filter (Current: 1A/div, Voltage: 200mV/div, Time: 2ms/div).

3.5 Conclusion

This chapter provided a complete set of impedance-type special parameters characterizing both, the source and the load-side interactions. It was demonstrated that the interac-

tion sensitivity of a dc-dc converter can be fully explained and analyzed based on the presented formulas. The given formulation can be utilized equally for predicted analytic transfer functions or measured frequency responses in case of commercial converters. The special impedance parameters consisting of internal transfer functions, are not directly measurable and need to be computed based on the measured frequency responses. Thus it was stated that the proper analysis of the detailed interactions needs to be performed based on Bode plots.

This chapter demonstrated that the control method has significant impact on the converter interaction sensitivity. It was also stated that:

- VM-controlled converter is the most sensitive to both source and load-side interactions due to its internal resonant behavior and low input-noise attenuation.
- IVFF and PCM-OCF converters are slightly more sensitive to the source interactions than the PCM-controlled converter due to small open-loop output impedance which reduces the short-circuit-input impedance.
- Due to simultaneous influence of the source and the load-impedances, even open-loop buck converter might become unstable.
- Under simultaneous interactions, the input and output-side minor-loop gains equally predict the stability of the converter but provide different robustness information.

The origin for the observed reduction in the source-side interactions for a converter with high input noise attenuation was explained from the fact that all the input-side impedances are the same. Furthermore, this results also reduced load impedance sensitivity, referring that the high peak in the source-side sensitivity function would not cause resonant peaking in the output impedance, even though all other internal transfer functions would be affected.

In addition, it was demonstrated that various mechanisms for system-level interactions exist. The dynamic representation was extracted for a system structure with input-parallel connected converters sharing an input filter. It was stated that an individual converter within the described system is more prone to source-side interactions due to the lower magnitude of the short-circuit-input impedance parameter characterizing the interactions. An experimental system was used to validate the theoretical analysis.

4 ARCHITECTURE COMPARISON IN TERMS OF STABILITY

The main contribution of this chapter is to propose performance metrics to state overall small-signal stability of a given distributed system. The objective is to express the stability with a single number and to provide a measure for the whole system enabling comparisons between various power-architecture solutions. Moreover, the objective is to present a simplified method to systematically analyze the overall system stability in order to integrate it into an existing power system architecture optimization methodology.

In the previous chapters, this thesis concentrated to assess the stability of a single interface between two components. Now the objective is to state the small-signal stability of the overall system. In Chapter 2, the presented concept of maximum peak criteria was employed to describe the robust stability at each system interface providing the least conservative stability margins. However, a distributed system consists of various components and interfaces. In order to compare different architecture solutions, a single parameter providing an overall measure of the whole system stability is required. The purpose is to provide a meaningful parameter for system comparisons: the best system in terms of robust stability is the one that minimizes the index.

In this chapter, the existing design and optimization tool for distributed power systems is first briefly introduced. Thereafter, the selection of the proper performance metrics to describe the overall system stability is discussed. Finally experimental system architectures are compared in terms of small-signal stability based on the selected stability index.

4.1 Introduction

Optimized size, cost and high efficiency as well as fast time-to-market are general design objectives for distributed systems. Therefore, the utilized components are typically commercial and the amount of available dc-dc converters from various manufacturers is large. The selection of proper components and their connections to form the system architecture is a complex task and the amount of possible architectural solutions for certain specification can be excessive. To facilitate this problem a tool to design and optimize power distribution systems in terms of size, cost and efficiency based on complex optimization

algorithms was developed in (Laguna et al., 2010, 2009).

The optimization process requires converter models applicable to commercial converters, which are independent of the internal structure. In (Oliver et al., 2009, 2006) a behavioral model for commercial dc-dc converter is presented based on hybrid Wiener-Hammerstein structure considering the power stage and its control as well as event driven behavior. This model is shown in Fig. 4.1, where the static part of the Wiener-Hammerstein structure describes the basic power processing ability and the dynamic input and output blocks consider the large signal behavior such as the initial inrush current and the transient response.

The logic system includes the event driven behavior due to control signals and protection features. This behavioral model can be generated according to the parameters obtained from the converter datasheet or based on measurements and it can be implemented by a circuit simulator utilizing hardware description language (Prieto et al., 2009). These models enable system-level simulations regarding the large-signal behavior including different protection features as well as startup behavior (Oliver et al., 2008; Prieto et al., 2009; Vesti et al., 2010).

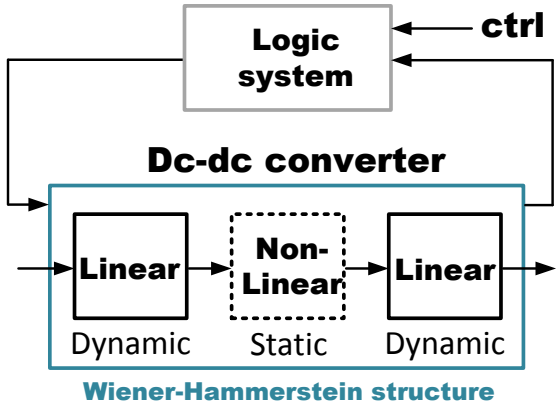

Fig. 4.1: Behavioral dc-dc converter model based on hybrid Wiener-Hammerstein structure (Oliver et al., 2009).

The optimization methodology analyzes large number of different design options, and therefore, extremely simple models are required. By considering only the static properties of the behavioral dc-dc converter model (Oliver et al., 2009) the requirements are considerably reduced and the converter model can be described as simple equations allowing the calculation of energy efficiency, size and cost (Laguna et al., 2010, 2009). In order to generate the architectural solutions, the following static parameters for the system are required:

- Source specification: system input voltage
- Load specifications: number of loads and their static parameters, input voltage and maximum power
- Library of modeled converters

The graphical user interface of the optimization tool is illustrated in Appendix J with the required system parameters. Based on the given specifications, the tool generates a set of optimized architectural solutions in terms of size, cost and efficiency as well as the best trade-offs between these features.

Due to the various simplifications assumed in the overall optimization process regarding the dc-dc converter models, the architecture solutions are obtained without considering the stability and dynamic performance of the system. Therefore, in order to assess the validity of an obtained optimized architecture and compare different solutions in terms of stability, the small-signal analysis is desired to be included as a part of the existing optimization methodology.

4.2 Measure of the whole system small-signal stability

In this section, the selection of the most appropriate index to state the overall system stability consisting of commercial converters is presented. For any system, the small-signal stability is a fundamental condition to comply with and it provides information whether two standalone stable subsystems can be cascaded without degrading the system performance or stability. In order to systematically assess the whole system stability, the assumed simplifications for the system-level modeling are first discussed, and thereafter, different methods to combine the stability information to a meaningful number are presented.

4.2.1 Simplified system-level analysis

The optimization methodology provides various architectural solutions according to the given specifications and the selected dc-dc converters. Already for a simple system with two loads, different design options exists as illustrated in Fig. 4.2. The load requirements for the system are typically static and no detailed information of the load impedance is available. Therefore, the loads are merely assumed as ideal current sources with certain requirements for the voltage and power ratings.

In order to assess the overall small-signal stability, the following simplifications are assumed within the system:

- Components are characterized by their input and output impedances

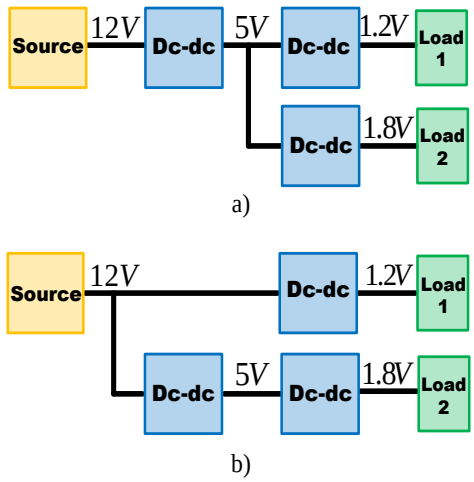

Fig. 4.2: Two architectural structures for the same specifications with a) pre-regulator and b) with single stage for Load 1 (Laguna et al., 2010).

- No parasitic or other coupling impedances within the system are considered
- Loads are assumed as ideal current sources

The system components considered in the stability analysis are input filters and dc-dc converters which are sufficient to be modeled by their input and output impedances. These impedances are directly measurable in the frequency domain or they can be identified according to the time-domain measurements (Oliver et al., 2009, 2006; Valdivia et al., 2009, 2010). Alternatively, in case the internal structure is known, the analytical expressions for the impedances can be applied as discussed in Chapter 3.

Based on the identified impedances, the stability at each system interface can be stated based on the minor-loop gain according to the Nyquist criterion as discussed in Chapter 2. Traditionally forbidden regions, out of which the minor-loop gain has to stay, provide certain minimum gain and phase margins. By applying the presented MPC-criteria, the robustness of stability at each interface is obtained as a single number. Thereafter, the stability information at every interface can be combined to one overall index as will be discussed in the following section.

The objective is to provide information whether the selected components can be connected to form a system according to the defined specifications, guaranteeing stability

and unaltered performance. Parasitic and other coupling impedances might degrade the system performance and in case detailed interactions are desired to be considered, the analysis can be performed as presented in Chapter 3.

4.2.2 Appropriate stability index

In this section, the most appropriate method to combine the provided stability information, i.e. the maximum peak value of the sensitivity function, at every interface to a meaningful number is discussed. Different options are evaluated based on an example system consisting of four converters with their respective input filters as illustrated in Fig. 4.3 emphasizing the interfaces where the stability is assessed by denoting them as M_s. The stability information at nominal operating point for this architecture is defined at each interface as:

- M_{s1} : 1.4 (3dB)
- M_{s2} : 1.2 (1.7dB)
- M_{s3} : 1.4 (3dB)
- M_{s4} : 1.1 (0.8dB)

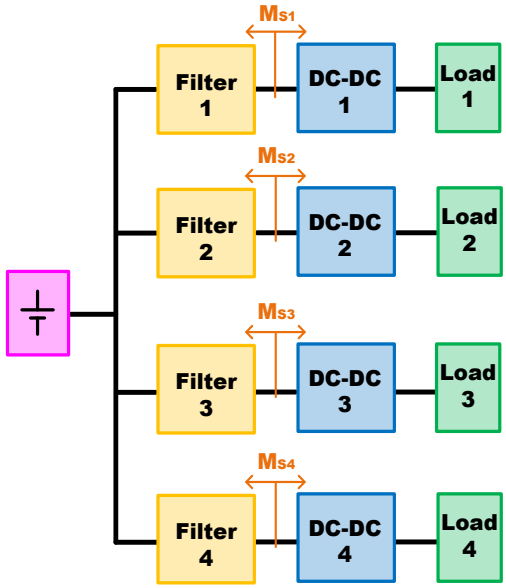

Fig. 4.3: Example architecture consisting of filters and dc-dc converters emphasizing the interfaces M_{s1} to M_{s4}, where the stability is assessed.

Different norms are typically utilized to provide a measure of the overall size of a vector, matrix, signal, or system and the most generally used norm is the Euclidean norm given in (4.1) (Skogestad and Postlethwaite, 2001). In control theory, the norms are applied in the controller synthesis, with the overall design objective of minimizing the utilized norm. For the purpose of optimized controller design, the most frequently used norm is the infinity-norm in (4.2) (Skogestad and Postlethwaite, 2001).

$$\| x\|_2 = \sqrt{| x|_1^2 + | x|_2^2 + \cdots + | x|_{\mathrm{n}}^2} \tag{4.1}$$

$$\| x\|_\infty = | x|_{\max} \tag{4.2}$$

The Euclidean norm corresponds to the square root of the sum of all singular squared values, whereas the infinity norm detects the largest singular value. The application of these norms to the example system provides the following values as for the overall stability index:

- $\| x\|_2$: 2.56
- $\| x\|_\infty$: 1.4

The Euclidean norm considers the stability information at every system interface. However, the obtained number itself is not descriptive of the overall stability and is required to be scaled in order to provide a meaningful number. For the simplicity of the analysis, it is not desirable to select an additional weighting function for the scaling, and therefore, this norm is not considered appropriate. The infinity norm provides information only regarding the system interface with the largest peak value while ignoring the rest of the stability information and thus it does not characterize the overall system stability.

Because the objective is to describe the whole system stability, central tendency of all peak values provides more meaningful number. This can be obtained by applying different averages such as arithmetic (A.M.) (4.3), geometric (G.M.) (4.4) and harmonic (H.M.) (4.5) means (Zwillinger, 1995). For the example system, they result the following stability index values:

- A.M.: 1.28
- G.M.: 1.27
- H.M.: 1.26

$$A.M. = \frac{x_1 + x_2 + \cdots + x_{\mathrm{n}}}{n} \tag{4.3}$$

$$G.M. = \sqrt[n]{x_1 x_2 \cdots x_{\mathrm{n}}} \tag{4.4}$$

$$H.M. = \frac{n}{\frac{1}{x_1} + \frac{1}{x_2} + \cdots + \frac{1}{x_{\mathrm{n}}}} \tag{4.5}$$

Each applied mean provides a similar value to characterize the system stability and they could be all applied to represent the overall stability. However, the Arithmetic mean is sensitive to large anomalies within the set of values and would be influenced by a single large peak value. Therefore, it would not necessarily provide the most representative index for the overall system stability. The other averages dampen the effect of very high or low values thus characterizing better the typical peak values of the interfaces.

The geometric mean (4.4) of the absolute peaking values can be also obtained according to (4.6) as the Arithmetic average of the peaking values expressed in dB (Zwillinger, 1995).

$$\log(G.M.) = \frac{\log x_1 + \log x_2 + \cdots + \log x_{\mathrm{n}}}{n} \tag{4.6}$$

Any of the described averages could be chosen as the stability index. However, the G.M. provides a convenient and straightforward method, because either the absolute values (4.4) or dB values (4.6) of the $S_{\max}$ can be utilized, and therefore, it is chosen. The selected stability metrics represents the average maximum peak value of the whole system providing corresponding gain and phase margins which can be obtained as discussed in Chapter 2. Therefore,different architectural structures can be compared and the best system in terms of robust stability is the one that minimizes the index.

4.2.3 Overall robustness

The geometric mean provides a number to characterize the average robustness of the specific system architecture and it does not consider the influence of very large individual peak value. Therefore, this index is not able to detect a single high peak value which might degrade the performance in one system interface. For instance, if the operating condition of the example system changes so that the $M_{\mathrm{s1}} = 1.1$ and $M_{\mathrm{s3}} = 2$, the following

can be observed:

- The obtained stability index provides similar results under nominal (1.27) and altered (1.3) operating points
- The maximum peak value under first condition is 1.4 (3dB) and under second condition 2 (6dB)

Even though the provided stability index is similar for both operating conditions, the robustness information in one interface varies significantly. For the nominal operating point, every interface provides good margins for stability with the maximum value of 1.4 (3 dB) but under the second operating condition, the interface M_{s3} with the value of 2 (6dB) is close to violate the margins for robustness. Therefore, in order to comprehensively describe the overall robust stability of the system, additionally the infinity norm (4.2) is applied to detect the weakest point in the system.

4.3 Practical architecture comparison

In order to perform practical system comparisons based on the selected stability index, three state-of-the-art converters from different manufacturers are utilized to form different architectures based on given system requirements. The stability at each interface is assessed based on measured impedances, and thereafter, by applying the specified stability index the architectures can be compared in terms of robust stability. Finally, the advantages and limitations of the proposed stability analysis methodology are discussed.

4.3.1 System architectures

The specifications for the architecture are shown in Fig. 4.4 where the loads are assumed as ideal current sources showing the required voltage levels and maximum power ratings. The selected commercial converters utilized to generate the architectural solutions of Fig. 4.4 are:

- PT78ST100 Texas Instruments (TexasInstruments, 2000) (U_{in}: 9-38V, U_{o}: 5V, P_{max}: 7.5W). Module: M2
- TSR-1 Traco Power (Tracopower, 2009) (U_{in}: 4.75-36V, U_{o}: 3.3V, P_{max}: 3.3W). Module: M3
- LM2853 National Semiconductor (NationalSemiconductor, 2006) (U_{in}: 5.5-3.3V, U_{o}: 3.3V, P_{max}: 9.9W). Module: M4

According to the given specifications, three different architectural solutions, denoted as Architecture 1, 2 and 3 in the further analysis, are formed using these commercial

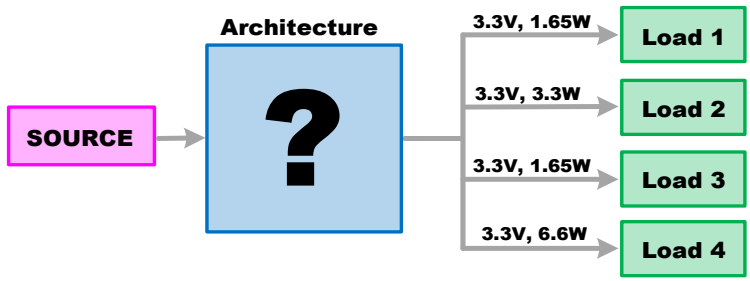

Fig. 4.4: Source and load specifications for the system architecture.

converters. Additionally, each architectural solution contains a single stage input filter as illustrated in Fig. 4.5 with the following component values:

- F1 (L = 200μH, ESR_{L} = 60mΩ, C = 260μF, ESR_{C} = 100mΩ)
- F2 (L = 260μH, ESR_{L} = 160mΩ, C = 260μF, ESR_{C} = 100mΩ)
- F3 (L = 120μH, ESR_{L} = 160mΩ, C = 300μF, ESR_{C} = 100mΩ)

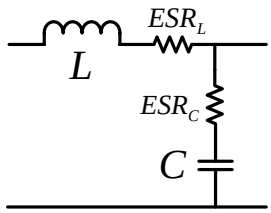

Fig. 4.5: Simple single-stage input filter structure.

These input filters are designed guaranteeing the stability but ignoring the attenuation features. The main aim for the filter is to obtain certain output impedance and thus provide different values for the sensitivity function in order to better compare the architectures. The obtained architectural structures including the filters are shown in Figs. 4.6, 4.7 and 4.8, where the utilized converters are referred as Module 2/3/4 and the filters as Filter 1/2/3. The interfaces where the stability is defined are emphasized and numbered as M_{s1},M_{s2} and M_{s3}.

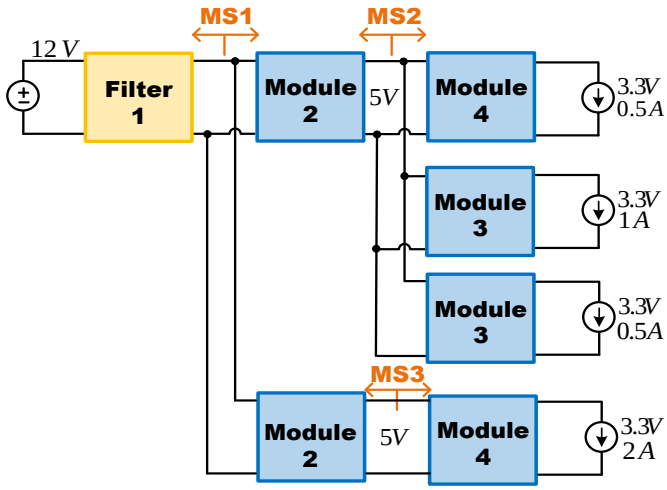

Fig. 4.6: Architectural structure 1 consisting of an input filter and six commercial converters emphasizing the interfaces where the small-signal stability is assessed.

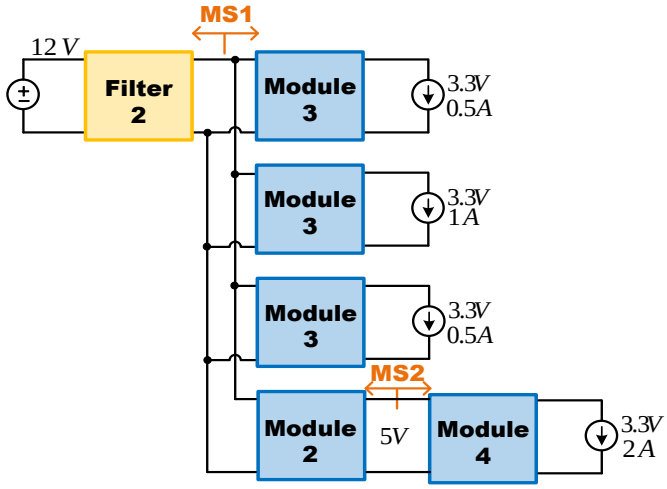

Fig. 4.7: Architectural structure 2 consisting of an input filter and five dc-dc converters emphasizing both interfaces, where the stability is assessed.

4.3.2 Comparison in terms of stability

The first step in the robustness analysis is to characterize the utilized commercial converters. Frequency response measurements were performed to obtain the information of the converter input and output impedances according to the defined system operating

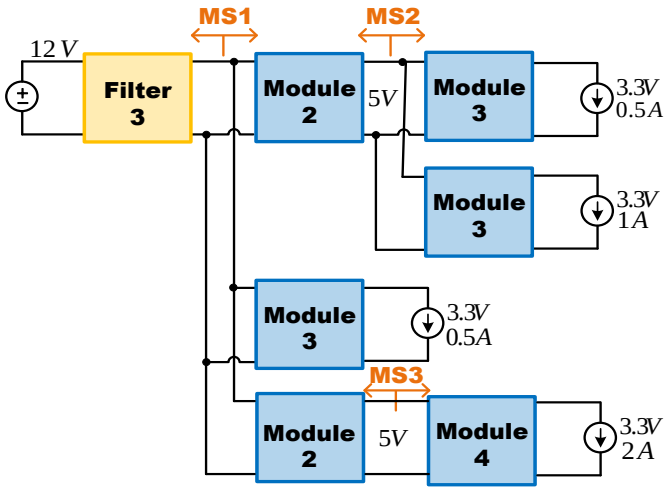

Fig. 4.8: Architectural structure 3 consisting of an input filter and six dc-dc converters emphasizing the interfaces, where the stability is assessed.

conditions. This implies that the same module might be required to be characterized at various operating points depending on the specifications. For instance, in order to correctly predict the robust stability at every interface of the Architecture 3, the module M3 (Tracopower, 2009) is required to be measured at three required operating points. This is illustrated in Fig. 4.9 where the measured input impedances at different operating conditions $Z_{\text{in-load1}}$ (U_{in}: 5V, I_{o}: 0.5A), $Z_{\text{in-load2}}$ (U_{in}: 5V, I_{o}: 1A) and $Z_{\text{in-load3}}$ (U_{in}: 12V, I_{o}: 0.5A)are shown.

Based on the obtained measurement data, the minor-loop gains are formed separately at every specified interface for each architectural solution. The resulting minor-loop gains are shown in Fig. 4.10 on the complex plane, where the MPC-region is defined for a maximum peak value of 6dB. It can be observed that each interface is stable and that the robust stability is guaranteed. The corresponding minor-loop gain based sensitivity functions are computed and presented in Fig. 4.11 for each architecture.

From the minor-loop gains on the complex plane in Fig. 4.10, it can be visually observed that the minor-loop gains of the Architecture 3 have the largest minimum distance between the point (-1.0), and consequently, the smallest peaking values of the corresponding sensitivity functions which can be observed from Fig. 4.11. Furthermore, it can be seen that Architecture 1 has the smallest distance between the the critical point (-1.0) and the minor-loop gain, ML_1, and therefore, the largest peak in the sensitivity function. This same robustness information at each system interface can be also represented numerically as provided in Table 4.1 together with the selected performance metrics.

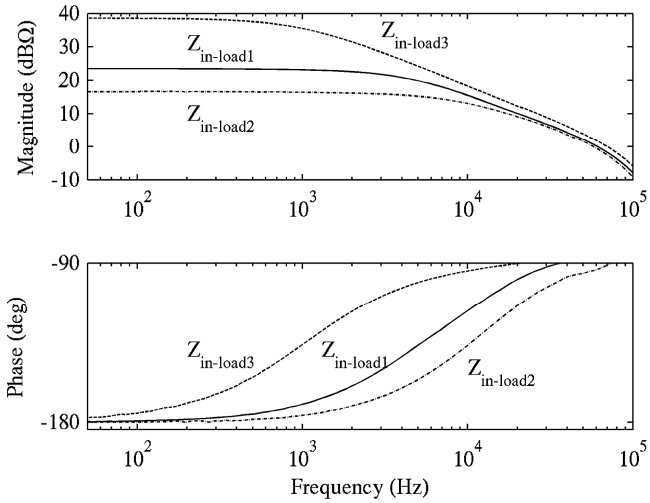

Fig. 4.9: The measured input impedances $Z_{\text{in-load1}}$, $Z_{\text{in-load2}}$, $Z_{\text{in-load3}}$ of the commercial module M3 at the operating points U_{in}: 5V, I_{o}: 0.5A, U_{in}: 5V, I_{o}: 1A and U_{in}: 12V, I_{o}: 0.5A, respectively for architecture 3.

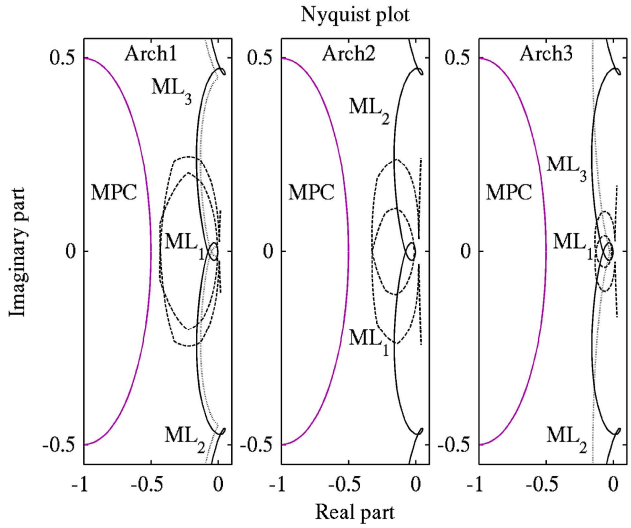

Fig. 4.10: Computed minor-loop gains at every interface of the different architectural structures.

The selected stability index provides another parameter, based on which different architectural solutions can be compared. Finally, the most appropriate architecture can be selected based on the application requirements. The results based on the example systems can be summarized as:

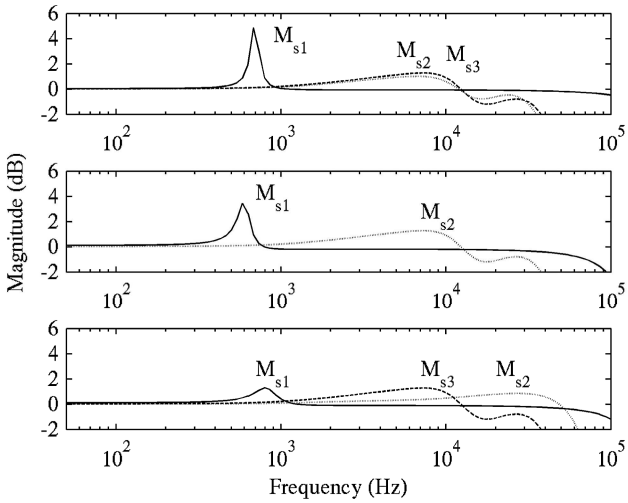

Fig. 4.11: Computed sensitivity functions at every interface for all of the architecture solutions.

Table 4.1: Computed maximum peak values and stability indices.

Interface	Architecture 1	Architecture 2	Architecture 3
M_{s1}	1.75 (4.87dB)	1.49 (3.44dB)	1.14 (1.29dB)
M_{s2}	1.12 (1.01dB)	1.16 (1.28dB)	1.1 (0.86dB)
M_{s3}	1.16 (1.28dB)		1.16 (1.28dB)
G.M.	1.31	1.28	1.13
x_∞	1.75	1.49	1.16

- Architecture 3 provides the best overall robustness of stability as well as the smallest worst case interface peak value
- Architecture 2 provides the smallest number of components and thus the smallest area with good margins for robust stability

The system robustness is operating-point dependent, and therefore, the stability index needs to be defined at certain operating condition. However, by characterizing the converters under different conditions, the stability index can be provided for each system at various operating points.

The limitation of this linear analysis method is that the system large-signal stability is not considered. Therefore, the presented analysis provides a necessary, but not sufficient condition for the global system stability. To guarantee the large-signal stability, additional time-domain simulations are required. They can be performed as discussed in (Vesti et al., 2010) based on the behavioral models including different system features.

4.4 Conclusions

In this chapter, a systematic and simplified methodology to assess the robust stability of an overall system was presented. It was based on applying the MPC-criteria, presented in this thesis, to obtain the least conservative margin for stability as a single number at every interface. By applying geometric mean, the stability information at each interface can be combined to a single figure of merit that provides a measure of the system stability. This index characterizes the overall system stability allowing architectural comparisons: the best system in terms of robust stability is the one that minimizes this value. Prior to the robustness analysis, the state of the stability needs to be defined at each interface applying the Nyquist criteria. Moreover, the infinity norm is used to identify the weakest point of the system in terms of robustness. The utilized small-signal stability assessment method is linear, and therefore, operating-point dependent implying that each component needs to be characterized at a specific operating condition.

The presented methodology allows stating the overall system stability as a single number thus enabling its integration as a part of the optimization tool. This provides simple and systematic method to assess the system small-signal stability in a short time. The practical comparison of different experimental systems consisting of few components was demonstrated based on the chosen index. Nevertheless, this method is applicable for more complex systems containing large number of components. This methodology provides a necessary but not sufficient condition for the global system stability. Therefore, additional time-domain simulations are required to validate the large-signal behavior.

5 CONCLUSIONS

This chapter presents the final conclusions, discussing first the main objectives and research questions set for the thesis. Thereafter, the findings in each chapter are summarized presenting the main contributions as well as the applicability and limitations of the results. Finally, future research topics are introduced.

5.1 Final conclusions

The main purpose of this thesis was to present methodologies to facilitate the overall design and dynamical analysis of dc-distributed systems. These systems typically consist of various interconnected commercial converters from different manufacturers and introduce unknown dynamics to the system. The dc-dc converters are standalone stable with certain specified performance but the component interconnection to form the system architecture creates unintentional couplings that might degrade the system performance. Therefore, the aim of this thesis was to answer to the following research questions:

- How to guarantee robust stability?
- How to define the dynamics and performance of a dc-distributed system without knowing the inner properties of the utilized converters?
- How to systematically assess the small-signal stability of a distributed system and compare different architectures in terms of stability?

Traditionally, the small-signal stability analysis of distributed systems is assessed based on the minor-loop gain, formed between the source output and load input impedances. The results are then typically given as a forbidden region out of which the minor-loop gain has to stay thus providing certain minimum gain and phase margins for the stability. In this thesis, the minor-loop gain was also utilized to state the system stability applying the Nyquist criterion. In order to provide the least conservative stability margins, a concept of maximum peak criteria was applied. This concept is well-known in control engineering and in Chapter 2 it was applied to the distributed systems to analyze the robustness of the stability. Based on this concept, a circular forbidden region was defined on the complex plane. Similar circle-like forbidden region had been used previously but without providing its origin and application limitations.

For the small-signal stability assessment, presented in Chapter 2, it was sufficient to characterize the system components by their input and output impedances. However, the detailed impedance-based interactions within the system depend on the internal converter dynamics. The source-side interactions analysis was established in the 1970's using the extra element theorem. However, applying this theorem the parameters describing the interactions sensitivity are not easily extractable for commercial converters. Therefore, in this thesis, the interactions were assessed using two-port structure to model the converter dynamics as was described in Chapter 3. Special parameters consisting of the internal transfer functions were extracted to describe the converter interaction sensitivity to the source and the load impedances. These internal transfer functions and thus the interaction sensitivity depend on the applied feedback and feedforward arrangements. In Chapter 3, the interaction dependence on the control method was presented obtaining detailed analytical expressions of the special parameters using existing dynamical equations for VM and PCM controls with input voltage and output current-feedforward, respectively. Furthermore, detailed theoretical formulation was provided to assess the system-level interactions due to cross-couplings.

Chapter 2 described the stability of the interconnection of two components whereas Chapter 4 concentrated to analyze the stability of the whole system consisting of various interconnections. Typically, the selection of proper commercial components from various manufacturers and their interconnections to form the distributed system architecture is a complex task with the objectives of small size, reduced cost, and high efficiency. This problem had been addressed previously by introducing a methodology to obtain optimized architectural solutions. However, the methodology is based on simplified behavioral converter models which ignore the stability. Therefore, the fourth chapter focused on assessing the robust stability of an overall system in a way that different systems could be compared. The stability at each interface was obtained applying the MPC concept introduced in Chapter 2. A geometric mean was chosen to combine the stability information to a meaningful index to characterize the average robustness of stability of the overall system. In addition, infinity norm was applied to detect the weakest interface of the system in terms of robustness.

Based on the findings within these chapters, the main contributions of this thesis were concluded as:

- It was shown that based on four internal transfer functions, the stability and performance of a system consisting of commercial or custom design modules can be predicted and analyzed.
- A methodology to obtain the least conservative stability margins as a single number guaranteeing robustness was introduced and it was shown theoretically and experimentally that using this method the robustness of stability is interface de-

pendent. Therefore, to correctly predict the robustness, the minor-loop gain is to be determined at the very input or output of the converter.

- A stability index to characterize the overall system robustness was proposed

Complete description and methodology to analyze the impedance-based interactions were provided. The source and load-side interaction sensitivity was explicitly shown to be assessable through specific transfer functions consisting of certain circuit elements. This methodology can be applied by using the frequency measurement data, time-domain identified transfer functions or analytical equations. The validity of this method was experimentally proven. It was shown that the converter transient response, in addition to the controller, might be influenced by the interactions within the system. The presented theoretical formulations can be translated into practical design rules and thus the behavior of a commercial converter within the interconnected system can be predicted.

This thesis demonstrated that the output impedance of a converter with high input-noise attenuation remains unaltered under the source interactions even though other internal transfer functions are affected. Therefore, these converters are less sensitive to the impedance based interactions. A formulation to assess system-level interactions was provided for an input parallel connected system introducing the cross-coupling mechanism. In addition, it was shown theoretically and experimentally that the special parameter characterizing the source-side interactions of a converter is altered due to the system connection as a comparison to the individual converter.

As shown in this thesis, the MPC method enables to predict the degradation in the internal dynamics and thus in the performance providing more information than any other stability assessment method. Therefore, other methods might lead rejecting a valid design solution or overdimensioned filters and extra capacitors without improving the performance due to more conservative stability margins. In addition, the robustness of the MPC concept is definable according to the system requirements and throughout this thesis, the maximum peak value of 2 (6dB) was utilized. It was also shown that the overall system small-signal stability can be stated applying the MPC concept to obtain the stability margins as a single number in each interface and combining this information by applying geometric mean. In addition to the average robust stability index, infinity norm was used to identify the worst case interface with the peak of sensitivity function. As a result by using these performance metrics, different power architectures can be compared in terms of robust stability.

The main limitation of the presented analysis methodology is that it is operating point-dependent, and therefore, the converters need to be characterized in different conditions. The worst-case condition for the interactions occurs when the source has the largest output impedance and the load has the lowest input impedance. In addition, the presented analysis methodology does not guarantee global system stability, and there-

fore, additional time-domain simulations are required to verify the large-signal stability. Moreover, in the presented analysis the converter was always assumed to be standalone stable within the normal operating mode without considering any protection features influencing the converter dynamics.

In the practical frequency domain characterization of commercial converters, it should be noted that the source and load impedances should be close to ideal to avoid any coupling with the measured internal transfer functions. Moreover, occasionally commercial modules might employ a discrete filter thus preventing the measurement of the direct input impedance for the robustness analysis. Nevertheless, the manufacturer specifies certain performance for the module and the stability is always assessable based on the minor-loop gain. In this thesis, the utilized input filters were designed in order to obtain certain output impedance value for the purpose of demonstrating the proposed analysis methodology. Therefore, no attenuation effects or any optimization in terms of size or performance are considered. The stability analysis considered only cascaded converters and a subsystem structure of input-parallel-connected converters with common source impedance.

Lastly, as final conclusion it can be stated that:

- Small-signal stability is a necessary condition for the system to comply with.
- The dc-dc converter should be characterized prior to the system integration as the discrete components used in dc-dc converters are characterized prior to the actual implementation.
- Frequency domain provides vital information for the system design.

Based on the analysis, instead of trial and error, it can be stated whether the converters can be cascaded or not, without degrading the performance. The possible performance degradation due to the interactions is typically observed in time-domain even though the origin of the problem can be only traced in the frequency domain.

5.2 Future research topics

Distributed systems typically consist of various components and for detailed analysis they are often divided into smaller subsystems. In this thesis, the interactions coupling is assessed only for input-parallel-connected converters, which share an input filter. In addition, in the presented analysis the converter is always considered in the normal operating region without any protections. Therefore, possible future research topic would be to identify different subsystem structures within a distributed system, e.g. parallel or series connected dc-dc converters, and to obtain dynamical description of these subsystems and assess the interaction couplings in more detail. Also the influence of additional fea-

tures of the converter, such as remote sensing or overcurrent protection to the converter dynamics could be analyzed.

The dynamical profiles and interaction sensitivity of traditional control methods with certain feedforward arrangements have been addressed in this thesis. However, various other control methods exist, whose dynamical influence on the dc-dc converters are unknown, such as $V^2 I_c$ and other ripple based schemes or sliding mode control. Therefore, a potential future research topic is to dynamically characterize dc-dc converters applying other control methods and assess the interaction sensitivity.

The stability index to state robust stability of a distributed system was introduced in this thesis based on the maximum peak criteria. In addition, it would be of interest to extract proper metrics to state the overall system performance referring to the system ability to supply all loads according to their transient specifications. Typically the load requirements concern time-domain transient response to a certain load change. Each converter is characterized for the stability analysis and thus their output impedance is known. Therefore, potential future research topic would be to identify the relationship between the frequency-domain information and time-domain with the objective of providing an overall index for the system performance.

REFERENCES

Abe, S., Hirokawa, M., Shoyama, M. and Ninomiya, T. (2008). Optimal intermediate bus capacitance for system stability on distributed power architecture, *IEEE Power Electron. Spec. Conf., PESC*, pp. 611–616. DOI: 10.1109/PESC.2008.4591997.

Acevedo, S. and Molinas, M. (2011). Power electronics modeling fidelity: Impact on stability estimate of micro-grid systems, *IEEE Innovative Smart Grid Technologies Asia, ISGT*, pp. 1–8. DOI: 10.1109/ISGT-Asia.2011.6167159.

Arnedo, L., Boroyevic, D., Burgos, R. and Wang, F. (2008). Un-terminated frequency response measurements and model order reduction for black-box terminal characterization models, *IEEE Appl. Power Electron. Conf. Expo., APEC*, pp. 1054–1060. DOI: 10.1109/APEC.2008.4522852.

Arnedo, L., Burgos, R., Boroyevic, D. and Wangl, F. (2009). System-level black-box dc-to-dc converter models, *IEEE Appl. Power Electron. Conf. Expo., APEC*, pp. 1476–1481. DOI: 10.1109/APEC.2009.4802861.

Aström, K. and Murray, R. (2008). *Feedback Systems: An Introduction for Scientists and Engineers*, Princeton University Press, USA.

B. Cho, J.R. Lee, F. L. (1990). Large-signal stability analysis of spacecraft power processing systems, *IEEE Trans. Power. Electron.* **5**(1): 110–116. DOI: 10.1109/63.46005.

Balog, R. and Krein, P. (2011). Bus selection in multibus dc microgrids, *IEEE Trans. Power. Electron.* **26**(3): 860–867. DOI: 10.1109/TPEL.2010.2094208.

Basso, C. (2012). The dark side of loop control theory, *IEEE Appl. Power Electron. Conf. Expo., APEC*, p. 72. Professional education seminar.

Bebic, J., Walling, R., O'Brien, K. and Kroposki, B. (2010). The Sun also rises: Planning for large-scale solar power, *IEEE Trans Ind. Electron.* **57**(4): 1330–1341. DOI: 10.1109/TIE.2009.2030219.

Bilberry, C., Mazzola, M. and Gafford, J. (2012). Power supply on chip (pwrsoc) model identification using black-box modeling techniques, *IEEE Appl. Power Electron. Conf. Expo., APEC*, pp. 1821–1825. DOI:10.1109/APEC.2012.6166069.

Brush, L. (2003). Distributed power architecture demand characteristics, *IEEE Appl. Power Electron. Conf. Expo., APEC*, pp. 342–345. DOI: 10.1109/APEC.2004.1295832.

Cespedes, M., Xing, L. and Sun, J. (2011). Constant-power system stabilization by passive damping, *IEEE Trans. Power Electron.* **26**(7): 1832–1836. DOI: 10.1109/TPEL.2011.2151880.

Choi, B., abd B. H. Cho, J. K., Choi, S. and Wildrick, C. M. (2002). Designing control loop for dc-to-dc converters loaded with unknown ac dynamics, *IEEE Trans. Ind. Electron.* **49**(4): 925–932. DOI: 10.1109/TIE.2002.801249.

Choi, B., Kim, D., Choi, S. and Sun, J. (2005). Analysis of input filter interactions in switching power converters, *IEEE Trans. Power. Electron.* **22**(2): 452–460. DOI: 10.1109/TPEL.2006.889925.

Cvetkovic, I., Boroyevic, D., Mattavelli, P., Lee, F. and Dong, D. (2013). Unterminated small-signal behavioral model of dc-dc converters, *IEEE Trans. Power. Electron.* **28**(4): 1870–1879. DOI: 10.1109/TPEL.2012.2215056.

D. Marx, P. Magne, B. N.-M. S. P. B. D. (2008). Large signal stability analysis tools in dc power systems with constant power loads and variable power loads - a review, *IEEE Trans. Power. Electron.* **27**(4): 1773–1787. DOI: 10.1109/TPEL.2011.2170202.

D.Boroyevic, Cvetkovic, I., Burgos, R., Wang, F. and Lee, F. (2010). Future electronic power distribution systems: a contemplative view, *IEEE Optim. Elect. Electron. Equip., OPTIM*, pp. 1369–1380. DOI: 10.1109/OPTIM.2010.5510477.

Dorf, R. C. and Bishop, R. H. (2001). *Modern Control Systems*, Prentice-Hall Inc., USA.

Emadi, A. and Ehsani, M. (2000). Aircraft systems: Technology, state of the art and future trends, *IEEE Trans. Aerosp. Electron. Syst.* **15**(1): 28–32. DOI: 10.1109/62.821660.

Erickson, R. and Maksimovic, D. (2001). *Fundamentals of Power Electronics*, Kluwer Academic Publishers, USA.

EricssonPowerModules (2011). Dc/dc regulator, *PMB 8518T P datasheet.* [Revised Nov. 2011].

F. Lee, M. Ming, S. W.-B. L. (1993). Design challenges for distributed power systems, *IEEE Power Electron. Motion Control Conf., IPEMC*, pp. 1–15. DOI: 10.1109/IPEMC.2006.4777941.

Fangcheng, L., Jinjun, L., Haodong, Z., Danhong, X., Saad, H. and Linyuan, Z. (2013). Stability issues of z+z or y+y type cascade system, *IEEE Energy Conversion Congr. Expo., ECCE*, pp. 434–441. DOI: 10.1109/ECCE.2013.6646734.

Feng, X. and Lee, F. (2000). On-line measurement on stability margin of dc distributed power system, *IEEE Appl. Power Electron. Conf. Expo., APEC*, pp. 1190–1196. DOI: 10.1109/APEC.2000.822838.

Fernandez-Herrero, A., Fernandez, C., Carreras, C., Zumel, P., Lazaro, A. and Barrado, A. (2012). Use of multisine excitations for frequency-response measurement of non-linear dc-dc switching converters, *IEEE Appl. Power Electron. Conf. Expo., APEC*, pp. 735–739. DOI:10.1109/APEC.2012.6165901.

Foley, R., Waldron, F., Slowey, J., Alderman, A., Narveson, B. and O'Mathuna, C. (2010). Technology roadmapping for power supply in package (psip) and power supply on chip (pwrsoc), *IEEE Appl. Power Electron. Conf. Expo., APEC*, pp. 525–532. DOI: 10.1109/APEC.2010.5433622.

Griffo, A., Wang, J. and Howe, D. (2008). Large signal stability analysis of dc power systems with constant power loads, *IEEE Veh. Power and Propulsion Conf, VPPC*, pp. 1–6. DOI: 10.1109/VPPC.2008.4677551.

Hankaniemi, M., Karppanen, M. and Suntio, T. (2006a). Dynamical characterization of voltage-mode controlled buck converter operating in ccm and dcm, *IEEE Power Electon. Motion Cont. Conf., EPE-PEMC*, pp. 816–821. DOI: 10.1109/EPEPEMC.2006.4778500.

Hankaniemi, M., Karppanen, M. and Suntio, T. (2006b). Load-imposed instability and performance degradation in a regulated converter, *IEEE Proc. Electr. Power Appl.* **153**(6): 781–786. DOI: 10.1049/ip-epa:20060080.

Hankaniemi, M., Karppanen, M. and Suntio, T. (2006c). Source-reflected load interactions in a regulated converter, *IEEE Ind. Electon. Annu. Conf.,IECON*, pp. 2893–2898. DOI: 10.1109/IECON.2006.347324.

Hankaniemi, M., Sippola, M. and Suntio, T. (2005a). Characterization of regulated converters to ensure stability and performance in distributed power supply systems, *IEEE Telec. Conf.,INTELEC*, pp. 533–538. DOI: 10.1109/INTLEC.2005.335155.

Hankaniemi, M., Sippola, M. and Suntio, T. (2005b). Load-impedance based interactions in regulated converters, *IEEE Telec. Conf.,INTELEC*, pp. 569–573. DOI: 10.1109/INTLEC.2005.335161.

Hensgens, N., Oliver, J. A., Cobos, J. A., Skibin, S. and Ecklebe, A. (2013). Design and multi-objetive optimization of emi input filters, *IEEE Appl. Power Electron. Conf. Expo., APEC*, pp. 2506–2513. DOI: 10.1109/APEC.2013.6520648.

Hentunen, H., Zenger, K. and Suntio, T. (2004). A systematic approach to analyze the stability of distributed power supply systems, *Nordic Workshop Power Electron.*, pp. 1–6.

Karppanen, M., Suntio, T. and Sippola, M. (2007a). Dynamical characterization of input-voltage-feedforward-controlled buck converter, *IEEE Trans. Ind. Electron.* **54**(2): 1005–1013. DOI: 10.1109/TIE.2007.892732.

Karppanen, M., Suntio, T. and Sippola, M. (2007b). Dynamical characterization of peak-current-mode-controlled buck converter with output-current feedforward, *IEEE Trans. Power Electron.* **22**(2): 444–451. DOI: 10.1109/TPEL.2006.889921.

Khalig, A. (2008). Realization of parasitic in stability of dc-dc converters loaded by constant power loads in advanced multiconverter automotive systems, *IEEE Trans. Ind. Electron.* **55**(6): 28–32. DOI: 10.1109/TIE.2008.918395.

Kwasinski, A. (2011). Quantitative evaluation of dc microgrids availability: Effects of system architecture and converter topology design choices, *IEEE Trans. Power. Electron.* **26**(3): 3118–3128. DOI: 10.1109/TPEL.2010.2102774.

Kwasinski, A. and Onwuchekwa, C. (2011). Dynamic behavior and stabilization of dc microgrids with instantaneous constant-power loads, *IEEE Trans. Power Electron* **26**(3): 1216–1226. DOI:10.1109/TPEL.2010.2091285.

Laguna, L., Prieto, R., Oliver, J. A., Cobos, J. A. and Visairo-Cruz, H. (2010). Fast architecture generation and evaluation techniques for the design of large power systems, *IEEE Energy Conversion Congr. Expo., ECCE*, pp. 3464–3469. DOI: 10.1109/IAS.2006.256646.

Laguna, L., Prieto, R., Oliver, J. A., Cobos, J. A., Visairo-Cruz, H. and Kumar, P. (2009). Power conversion modeling methodology based on building block models, *IEEE Energy Conversion Congr. Expo., ECCE*, pp. 3404–3410. DOI:10.1109/ECCE.2009.5316311.

Leppaaho, J. (2008). *Issues in Dynamic Analysis and Design of Interconnected DC-DC Power Supply Systems*, PhD thesis, Tampere University of Technology.

Leppaaho, J., Huusari, J., Nousiainen, L., Puukko, J. and Suntio, T. (2011). Dynamic properties and stability assessment of current-fed converters in photovoltaic applications, *IEEJ Trans. Ind. Appl.* **1**. DOI: 10.1541/ieejias.131.976.

Li, P. and Lehman, B. (2005). Accurate loop gain prediction for dc-dc converter due to the impact of source/input filter, *IEEE Trans. Power. Electron.* **20**(4): 754–761. DOI: 10.1109/TPEL.2005.850916.

Liu, X., Zhou, Y., Zhang, W. and Ma, S. (201). Stability criteria for constant power loads with multistage lc filters, *IEEE Trans. Veh. Technol.* **60**(5): 2042–2049. DOI: 10.1109/TVT.2011.2148133.

Liukkonen, M., Hinkkanen, M., Kyyra, J. and Ovaska, S. J. (2013). Modeling of multiport dc busses in power-electronic systems, *IEEE Int. Conf. Ind. Techn., ICIT*, pp. 740–745. DOI: 10.1109/ICIT.2013.6505764.

López, T. and Alarcon, E. (2012). Power mosfet technology roadmap toward high power density voltage regulators for next-generation computer processors, *IEEE Trans. Power Electron.* **27**(4): 2193–2203. DOI: 10.1109/TPEL.2011.2165343.

Luo, S. and Batarseh, I. (2005). A review of distributed power systems part i: Dc distributed power system, *IEEE Aerosp. Electron. Syst. Mag.* **20**(8): 6–16. DOI: 10.1109/MAES.2005.1499272.

Luo, S. and Batarseh, I. (2006). A review of distributed power systems part ii. high frequency ac distributed power systems, *IEEE Aerosp. Electron. Syst. Mag.* **21**(6): 5–14. DOI: 10.1109/MAES.2006.1662037.

M. Belkhayat, R. Cooley, A. W. (1995). Large signal stability criteria for distributed systems with constant power loads, *IEEE Power Electron. Spec. Conf, PESC*, pp. 1333–1338. DOI: 10.1109/PESC.1995.474987.

Mammano, B. (1993). Distributed power systems, *Unitrode Power Supply Des. Sem., SEM900*, pp. 1–11.

Maranesi, P., Tavazzi, V. and Varoli, V. (1988). Two-port characterization of pwm voltage regulators at low frequencies, *IEEE Trans. Ind. Electron.* **35**(3): 2746–2755. DOI: 10.1109/41.3120.

Middlebrook, R. (1976). Input filter considerations in design and application of switching regulators, *IEEEInd. Appl. Soc. Annu. Meeting*, pp. 366–382.

Middlebrook, R. (1978). Design techniques for preventing input filter oscillations in switched-mode regulators, *IEEE Power Convers. Conf.*, pp. 1–16.

Middlebrook, R. and Cuk, S. (1976). A general unified approach to modeling switching-converter power stages, *IEEE Power Electron. Spec. Conf.*, pp. 18–34.

Middlebrook, R. D. (1989). Null double injection and the extra element theorem, *IEEE Trans. Educ.* **32**(3): 167–180. DOI: 10.1109/13.34149.

Miftakhutdinov, R. (2009). Improving system efficiency with a new intermediate-bus architecture, *Texas Instruments Inc. Seminar*.

NationalSemiconductor (2006). Synchronous simple switcher buck regulator, *LM2853 datasheet*. [Revised Dec. 2014].

Oliver, J. A., Prieto, R., Cobos, J. A., Garcia, O. and Alou, P. (2009). Hybrid wiener-hammerstein structure for grey-box modeling of dc-dc converters, *IEEE Appl. Power Electron. Conf. Expo., APEC*, pp. 280–285. DOI: 10.1109/APEC.2009.4802669.

Oliver, J. A., Prieto, R., Laguna, L. and Cobos, J. A. (2008). Modeling and simulation requirements for the analysis and design of dc distributed power electronics systems, *IEEE Power Electron. Congress, CIEP*, pp. 204–209. DOI: 10.1109/CIEP.2008.4653844.

Oliver, J. A., Prieto, R., Romero, V. and Cobos, J. A. (2006). Behavioral modeling of dc-dc converters for large-signal simulation of distributed power systems, *IEEE Appl. Power Electron. Conf. Expo., APEC*, p. 6. DOI: 10.1109/APEC.2006.1620692.

Panovo, Y. and Jovanovic, M. (2005). Practical issues of input/output impedance measurements in switching power supplies and application of measured data to stability analysis, *IEEE Appl. Power Electron. Conf. Expo., APEC*, pp. 1339–1345. DOI: 10.1109/APEC.2005.1453183.

Peng, L. and Lehman, B. (2004). Performance prediction of dc-dc converters with impedances as loads, *IEEE Trans. Power. Electron.* **19**(1): 201–209. DOI: 10.1109/TPEL.2003.820560.

Prieto, R., Laguna, L., Oliver, J. A. and Cobos, J. A. (2009). Dc-dc converter parametric models for system level simulation, *IEEE Appl. Power Electron. Conf. Expo., APEC*, pp. 292–297. DOI: 10.1109/APEC.2009.4802671.

Rahimi, A. and Emadi, A. (2009). Optimal damping of emi filter input impedance, *IEEE Trans. Ind. Electron.* **56**(5): 363–377. DOI: 10.1109/TIA.2011.2127434.

Riccobono, A. and Santi, E. (2012a). Comprehensive review of stability criteria for dc distribution systems, *IEEE Energy Conversion Congr. Expo., ECCE*, pp. 3917–3925. DOI: 10.1109/ECCE.2012.6342299.

Riccobono, A. and Santi, E. (2012b). A novel passivity-based stability criterion (psbc) for switching converter dc distribution systems, *IEEE Appl. Power Electron. Conf. Expo., APEC*, pp. 2560–2567. DOI: 10.1109/APEC.2012.6166184.

Rodriguez, M., Stahl, G., Corradini, L. and Maksimovic, D. (2013). Smart dc power management system based on software-configurable power modules, *IEEE Trans.Power. Electron.* **28**(4): 3118–3128. DOI: 10.1109/TPEL.2012.2209681.

Sandler, S. (2014). Five things every engineer should know about bode plots, *Power Electronics Technology*.

URL: *http://powerelectronics.com/power-electronics-systems/five-things-every-engineer-should-know-about-bode-plots*

Sandler, S., Ho, P. and Hymowitz, C. (2012). When bode plots fail us.
URL: *http://powerelectronics.com/power-electronics-systems/when-bode-plots-fail-us*

Sayani, M. P. and Wanes, J. (2003). Analyzing and determining optimum onboard power architectures for 48 v-input systems, *IEEE Appl. Power Electron. Conf. Expo., APEC*, pp. 781–785. DOI: 10.1109/APEC.2003.1179304.

Skogestad, S. and Postlethwaite, I. (2001). *Multivariable Feedback Control - Analysis and Design*, John Wiley and Sons, UK.

Sokal, N. O. (1973). System oscillations from negative input resistance at power input port of switching-mode regulator, amplifier, dc/dc converter, or dc/ac inverter, *IEEEPower Electron. Spec. Conf., PESC*, pp. 138–140.

Sudhoff, S. D., Glover, S. F., Lamm, P. T., Schmucker, D. H. and Delisle, D. E. (2000). Admittance space stability analysis of power electronic systems, *IEEE Trans. Aerosp. Electron. Syst.* **36**(3): 965–973. DOI: 10.1109/7.869516.

Sudhoff, S., Pekarek, S., Kuhn, B., Glover, S., Sauer, J. and Delisle, D. (2002). Naval combat survivability testbeds for investigation of issues in shipboard power electronics based power and propulsions systems, *IEEE Power Eng. Soc. Summer Meet.*, pp. 347–350. DOI: 10.1109/PESS.2002.1043248.

Sun, J. (2009). Small-signal methods for ac distributed power systems - a review, *IEEE Trans. Power Electron.* **24**(11): 2545–2554. DOI: 10.1109/TPEL.2009.2029859.

Sun, J. (2011). Impedance-based stability criterion for grid-connected inverters, *IEEE Trans.Power Electron.* **26**(11): 3075–3078. DOI: 10.1109/TPEL.2011.2136439.

Sun, J. (2013). *Small-signal Methods for AC Power Electronics Systems*. 129 pp.

Suntio, T. (2010). Unified average and small-signal modeling of direct-on-time control, *IEEE Ind. Electron.* **53**(1): 287–295. DOI: 10.1109/TIE.2005.862221.

Suntio, T., Hankaniemi, M. and Karppanen, M. (2006). Analysing the dynamics of regulated converters, *IEEE Electr. Power Appl.* **153**(6): 905–910. DOI: 10.1049/ip-epa:20050481.

Suntio, T., Leppaaho, J. and Hankaniemi, M. (2009). On emi-filter interactions in a regulated converter - stability and load-transient performance, *IEEE Energy Conversion Congr. Expo., ECCE*, pp. 3031–3038. DOI: 10.1109/ECCE.2009.5316547.

Suntio, T., Leppaaho, J., Huusari, J. and Nousiainen, L. (2010). Issues on solar-generator interfacing with current-fed MPP-tracking converters, *IEEE Trans. Power Electron.* **25**(9): 2409–2419. DOI: 10.1109/TPEL.2010.2048580.

Tabisz, W., Jovanovic, M. and Lee, F. (1992). Present and future of distributed power systems, *IEEE Appl. Power Electron. Conf. Expo., APEC*, pp. 11–18. DOI: 10.1109/APEC.1992.228437.

Tabisz, W., Jovanovic, M. and Lee, F. (2005). Coordination of design issues in the intermediate bus architecture, *IEEE Appl. Power Electron. Conf. Expo., APEC*, pp. 169–175. DOI: 10.1109/APEC.2005.1452914.

TexasInstruments (2000). Positive step-down integrated switching regulator, *PT78ST100 datasheet*. [Revised Feb. 2014].

Tracopower (2009). Non-isolated point-of-load converter, *TSR 1-2433 datasheet*. Revised Jun. 2009.

Tse, C. K. and di Bernardo, M. (2002). Complex behavior in switching power converters, *IEEE Proc.* **90**(5): 768–781. DOI: 10.1109/JPROC.2002.1015006.

Valdivia, V., Barrado, A., Lazaro, A., Zumel, P., Raga, C. and Fernandez, C. (2009). Simple modeling and identification procedures for black-box behavioral modeling of power converters based on transient response, *IEEE Trans. Power. Electron.* **24**(12): 1131–1138. DOI:10.1109/TPEL.2009.2030957.

Valdivia, V., Barrado, A., Roldan, A. M., Fernandez, C. and Zumel, P. (2010). Black-box modeling of dc-dc converters based on transient response analysis and parametric identification methods, *IEEE Appl. Power Electron. Conf. Expo., APEC*, pp. 1131–1138. DOI: 10.1109/APEC.2010.5433361.

Vesti, S., Alou, P., Oliver, J., Garcia, O., Prieto, R. and Cobos, J. (2010). Modeling and simulation of a distributed power system for avionic application, *IEEE Energy Conversion Congr. Expo., ECCE*, pp. 4421–4427. DOI: 10.1109/ECCE.2010.5618442.

Vesti, S., Oliver, J., Prieto, R., Cobos, J., Huusari, J. and Suntio, T. (2012). Practical characterization of input-parallel-connected converters with a common input filter, *IEEE Applied Power Electronics Conf., APEC*, pp. 1845–1852. DOI10.1109/APEC.2012.6166073.

Vesti, S., Oliver, J., Prieto, R., Cobos, J. and Suntio, T. (2011). Stability and transient performance assessment in a cots-module-based distributed dc/dc system, *IEEE Telecom. Conf., INTELEC*, pp. 1–7. DOI10.1109/INTLEC.2011.6099723.

Vesti, S., Suntio, T., Oliver, J., Prieto, R. and Cobos, J. (2013a). Effect of control method on impedance-based interactions in a buck converter, *IEEE Trans. Power Electron.* **28**(11): 5311–5322. DOI: 10.1109/TPEL.2013.2247422.

Vesti, S., Suntio, T., Oliver, J., Prieto, R. and Cobos, J. (2013b). Impedance-based stability and transient-performance assessment applying maximum peak criteria, *IEEE Trans. Power Electron.* **28**(5): 2099–2104. DOI: 10.1109/TPEL.2012.2220157.

Vestii, S., Oliver, J., Prieto, R., Cobos, J. and Suntio, T. (2013). Performance metrics for small-signal stability assessment of dc-distributed power-system-architecture comparisons, *IEEE Energy Conversion Congr. Expo., ECCE*, pp. 5403–5409. DOI10.1109/ECCE.2013.6647434.

Vicor (2013). Intermediate bus converter module, *IB048E120T40N1-00 datasheet.* Revised Aug. 2013.

Wand, X., Blaaberg, F., Lizarre, M., Chen, Z., He, J. and Li, Y. (2014). An active damper for stabilizing power-electronics-based ac systems, *IEEE Ind. Electron. Mag.* **29**(7): 3318–3329. DOI: 10.1109/TPEL.2013.2278716.

Wang, J. and Howe, D. (2009). A power shaping stabilizing control strategy for dc power systems with constant power loads, *IEEE Trans. Power. Electron.* **23**(6): 2982–2989. DOI: 10.1109/TPEL.2008.2004594.

Wildrick, C. M., Lee, F. C., Cho, B. H. and Choi, B. (1995). A method of defining the load impedance specification for a stable distributed power system, *IEEE Trans. Power Electron.* **10**(3): 280–285. DOI: 10.1109/63.387992.

X.Feng, Liu, J. and Leei, F. C. (2002). Impedance specifications for stable dc distributed power systems, *IEEE Trans. Power Electron.* **17**(2): 157–162. DOI: 10.1109/63.988825.

Xing, L., Feng, F. and Sun, J. (2011). Optimal damping of emi filter input impedance, *IEEE Trans. Ind. Appl.* **47**(3): 1432–1440. DOI:10.1109/TIA.2011.2127434.

Xing, M. C. T. B. L. and Sun, J. (2012). Stabilization of constant-power loads with passive impedance damping, *IEEE Appl. Power Electron. Conf. Expo., APEC*, pp. 735–739. DOI:10.1109/APEC.2012.6165901.

Zhang, J. M., Jiao, X. X. D. Z. and Zhaoming, Q. (2004). Stability problems and input impedance improvement for cascaded power electronic systems, *IEEE Appl. Power Electron. Conf. Expo., APEC*, pp. 1018–1024. DOI:10.1109/APEC.2004.1295947.

Zwillinger, D. (1995). *Standard Mathematical Tables and Formulae*, UK.

A MEASUREMENT SETUP

In this thesis, the required parameters for the two-port model for commercial converters are obtained based on the frequency domain measurements. All measurements are performed using Venable Industries' frequency response analyzer model 3120 with an impedance measurement kit. The measurement setup is shown in Fig. A.1.

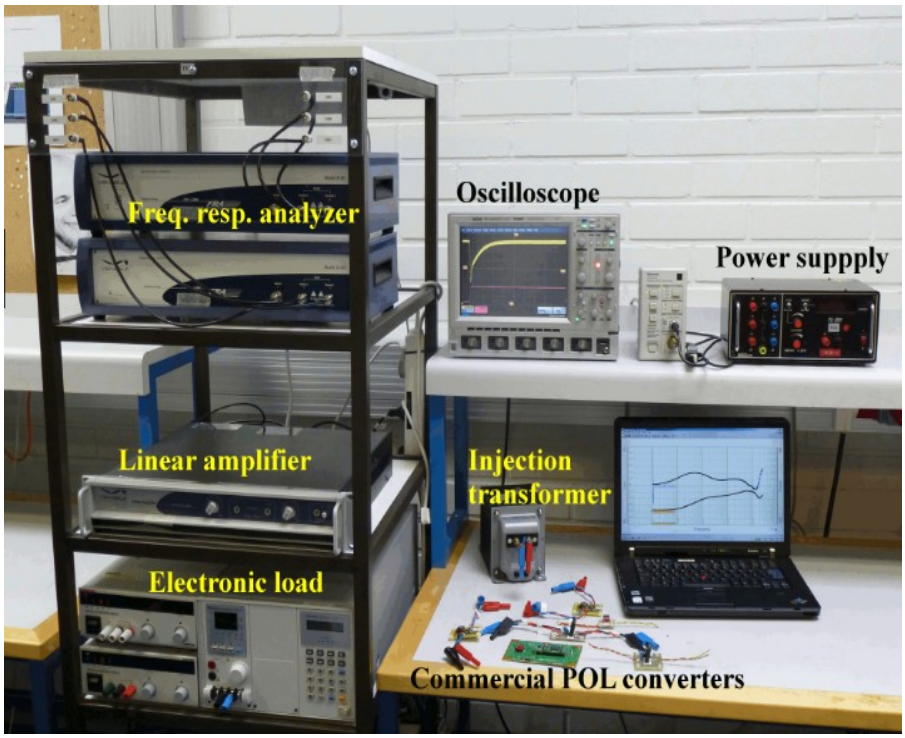

Fig. A.1: Utilized measurement setup for the frequency domain measurements.

B SOURCE-AFFECTED DYNAMICS

The converter two-port model is shown in Fig. B.1. The source and load are assumed ideal and the internal dynamics are emphasized with dashed lines and provided in (B.1).

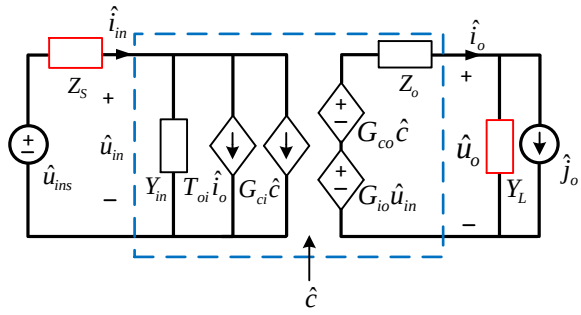

Fig. B.1: Two-port model including the control variable.

$$\begin{bmatrix} \hat{i}_{\mathrm{in}} \\ \hat{u}_{\mathrm{o}} \end{bmatrix} = \begin{bmatrix} Y_{\mathrm{in}} & T_{\mathrm{oi}} & G_{\mathrm{ci}} \\ G_{\mathrm{io}} & -Z_{\mathrm{o}} & G_{\mathrm{co}} \end{bmatrix} \begin{bmatrix} \hat{u}_{\mathrm{in}} \\ \hat{i}_{\mathrm{o}} \\ \hat{c} \end{bmatrix} \tag{B.1}$$

The influence of the source impedance to the converter dynamics is assessed by representing the input voltage as given in (B.2). This representation is replaced to the internal dynamics in (B.3), resulting the input dynamics of (B.4) and after (B.5) the output dynamics is expressed as (B.6).

$$\hat{u}_{\mathrm{in}} = \hat{u}_{\mathrm{ins}} - Z_{\mathrm{in}}\hat{i}_{\mathrm{in}} \tag{B.2}$$

$$\begin{aligned} \hat{i}_{\mathrm{in}} &= Y_{\mathrm{in}}(\hat{u}_{\mathrm{ins}} - Z_{\mathrm{s}}\hat{i}_{\mathrm{in}}) + T_{\mathrm{oi}}\hat{i}_{\mathrm{o}} + G_{\mathrm{ci}}\hat{c} \\ \hat{u}_{\mathrm{o}} &= G_{\mathrm{io}}(\hat{u}_{\mathrm{ins}} - Z_{\mathrm{s}}\hat{i}_{\mathrm{in}}) - Z_{\mathrm{o}}\hat{i}_{\mathrm{o}} + G_{\mathrm{co}}\hat{c} \end{aligned} \tag{B.3}$$

$$\hat{i}_{\text{in}} = (\frac{Y_{\text{in}}}{1 + Z_{\text{s}}Y_{\text{in}}})\hat{u}_{\text{ins}} + (\frac{T_{\text{oi}}}{1 + Z_{\text{s}}Y_{\text{in}}})\hat{i}_{\text{o}} + (\frac{G_{\text{ci}}}{1 + Z_{\text{s}}Y_{\text{in}}})\hat{c} \tag{B.4}$$

$$\begin{aligned}\hat{u}_{\text{o}} = &(\frac{G_{\text{io}} + G_{\text{io}}Z_{\text{s}}Y_{\text{in}} - G_{\text{io}}Z_{\text{s}}Y_{\text{in}}}{1 + Z_{\text{s}}Y_{\text{in}}})\hat{u}_{\text{ins}} - (\frac{Z_{\text{s}}G_{\text{io}}T_{\text{oi}} + Z_{\text{o}} + Z_{\text{o}}Z_{\text{s}}Y_{\text{in}}}{1 + Z_{\text{s}}Y_{\text{in}}})\hat{i}_{\text{o}} \\ &+ (\frac{G_{\text{co}} - Z_{\text{s}}G_{\text{io}}G_{\text{ci}} + G_{\text{co}}Z_{\text{s}}Y_{\text{in}}}{1 + Z_{\text{s}}Y_{\text{in}}})\hat{c}\end{aligned} \tag{B.5}$$

$$\begin{aligned}\hat{u}_{\text{o}} = &(\frac{G_{\text{io}}}{1 + Z_{\text{s}}Y_{\text{in}}})\hat{u}_{\text{ins}} - (\frac{1 + Z_{\text{s}}(Y_{\text{in}} + \frac{G_{\text{io}}T_{\text{oi}}}{Z_{\text{o}}})}{1 + Z_{\text{s}}Y_{\text{in}}})Z_{\text{o}}\hat{i}_{\text{o}} \\ &+ (\frac{1 + Z_{\text{s}}(Y_{\text{in}} - \frac{G_{\text{io}}G_{\text{ci}}}{G_{\text{co}}})}{1 + Z_{\text{s}}Y_{\text{in}}})G_{\text{co}}\hat{c}\end{aligned} \tag{B.6}$$

Based on these derivations , the source-affected system dynamics can be expressed as (B.7), where the expressions for the special input-side parameters $Y_{\text{in-sco}}$ (B.8) and $Y_{\text{in-}\infty}$ (B.9) are obtained from (B.6).

$$\begin{bmatrix} \hat{i}_{\text{in}} \\ \hat{u}_{\text{o}} \end{bmatrix} = \begin{bmatrix} \frac{Y_{\text{in}}}{1+Z_{\text{s}}Y_{\text{in}}} & \frac{T_{\text{oi}}}{1+Z_{\text{s}}Y_{\text{in}}} & \frac{G_{\text{ci}}}{1+Z_{\text{s}}Y_{\text{in}}} \\ \frac{G_{\text{io}}}{1+Z_{\text{s}}Y_{\text{in}}} & -\frac{1+Z_{\text{s}}Y_{\text{in-sco}}}{1+Z_{\text{s}}Y_{\text{in}}}Z_{\text{o}} & \frac{1+Z_{\text{s}}Y_{\text{in-}\infty}}{1+Z_{\text{s}}Y_{\text{in}}}G_{\text{co}} \end{bmatrix} \begin{bmatrix} \hat{u}_{\text{ins}} \\ \hat{i}_{\text{o}} \\ \hat{c} \end{bmatrix} \tag{B.7}$$

$$Y_{\text{in-sco}} = Y_{\text{in}} + \frac{G_{\text{io}}T_{\text{oi}}}{Z_{\text{o}}} \tag{B.8}$$

$$Y_{\text{in-}\infty} = Y_{\text{in}} - \frac{G_{\text{io-o}}G_{\text{ci-o}}}{G_{\text{co-o}}} \tag{B.9}$$

C SOURCE-SIDE SPECIAL PARAMETERS

The extraction of the source-side special parameters from the two-port model is provided in this appendix. In addition, it is shown that both parameters are independent of the output-side feedback state.

C.1 Extraction of special parameters $Y_{\text{in-sco}}$ and $Y_{\text{in-}\infty}$

The ideal input admittance is extracted from the original internal dynamics under the condition: $\hat{u}_{\text{o}} = 0$ and $\hat{i}_{\text{o}} = 0$ in (C.1) and solving the corresponding input impedance (C.2).

$$\begin{aligned} \hat{i}_{\text{in}} &= Y_{\text{in}}\hat{u}_{\text{in}} + G_{\text{ci}}\hat{c} \\ 0 &= G_{\text{io}}\hat{u}_{\text{in}} + G_{\text{co}}\hat{c} \end{aligned} \tag{C.1}$$

$$Y_{\text{in-}\infty} = \frac{\hat{i}_{\text{in}}}{\hat{u}_{\text{in}}} = Y_{\text{in}} - \frac{G_{\text{ci}}G_{\text{io}}}{G_{\text{co}}} \tag{C.2}$$

In a similar way, the short-circuit input admittance can be obtained but under the condition: $\hat{u}_{\text{o}} = 0$ and $\hat{c} = 0$ according to (C.3). The corresponding input impedance is obtained in (C.4).

$$\begin{aligned} \hat{i}_{\text{in}} &= Y_{\text{in}}\hat{u}_{\text{in}} + T_{\text{oi}}\hat{i}_{\text{o}} \\ 0 &= G_{\text{io}}\hat{u}_{\text{in}} - Z_{\text{o}}\hat{i}_{\text{o}} \end{aligned} \tag{C.3}$$

$$Y_{\text{in-sco}} = \frac{\hat{i}_{\text{in}}}{\hat{u}_{\text{in}}} = Y_{\text{in}} + \frac{T_{\text{oi}}G_{\text{io}}}{Z_{\text{o}}} \tag{C.4}$$

C.2 Parameter independence of the feedback

The dependence of both special parameters on the state-of-feedback can be assessed utilizing the dynamical expression in (C.5), which illustrates how the applied feedback

influences on the open-loop dynamics. The closed-loop infinite input impedance in (C.6) can be expressed using the internal dynamics from (C.5) resulting (C.7). Finally resulting to a infinite input admittance consisting of the open-loop transfer functions (C.8) thus demonstrating that the special parameter is independent of the state of the feedback.

$$\begin{bmatrix} \hat{i}_{\text{in}} \\ \hat{u}_{\text{o}} \end{bmatrix} = \begin{bmatrix} \frac{Y_{\text{in-o}}}{1+L_{\text{out}}} + \frac{L_{\text{out}}Y_{\text{in-}\infty}}{1+L_{\text{out}}} & \frac{T_{\text{oi-o}}}{1+L_{\text{out}}} + \frac{L_{\text{out}}T_{\text{oi-}\infty}}{1+L_{\text{out}}} & \frac{G_{\text{ci-o}}}{G_{\text{se}}G_{\text{co-o}}}\frac{L_{\text{out}}}{1+L_{\text{out}}} \\ \frac{G_{\text{io-o}}}{1+L_{\text{out}}} & -\frac{Z_{\text{o-o}}}{1+L_{\text{out}}} & \frac{1}{G_{\text{se}}}\frac{L_{\text{out}}}{1+L_{\text{out}}} \end{bmatrix} \begin{bmatrix} \hat{u}_{\text{in}} \\ \hat{i}_{\text{o}} \\ \hat{u}_{\text{ref}} \end{bmatrix} \tag{C.5}$$

$$Y_{\text{in-}\infty} = Y_{\text{in-c}} - \frac{G_{\text{io-c}}G_{\text{ci-c}}}{G_{\text{co-c}}} \tag{C.6}$$

$$\begin{aligned} Y_{\text{in-}\infty} &= \frac{Y_{\text{in-o}}}{1+L_{\text{out}}} + \frac{L_{\text{out}}(Y_{\text{in-o}} - \frac{G_{\text{io-o}}G_{\text{ci-o}}}{G_{\text{co-o}}})}{1+L_{\text{out}}} - \frac{\frac{G_{\text{io-o}}}{1+L_{\text{out}}}\frac{G_{\text{ci-o}}}{G_{\text{se}}G_{\text{co-o}}}\frac{L_{\text{out}}}{1+L_{\text{out}}}}{\frac{1}{G_{\text{se}}}\frac{L_{\text{out}}}{1+L_{\text{out}}}} \\ Y_{\text{in-}\infty} &= Y_{\text{in-o}} - \frac{L_{\text{out}}G_{\text{io-o}}G_{\text{ci-o}}}{G_{\text{co-o}}(1+L_{\text{out}})} - \frac{G_{\text{ci-o}}G_{\text{io-o}}}{G_{\text{co-o}}(1+L_{\text{out}})} \end{aligned} \tag{C.7}$$

$$Y_{\text{in-}\infty} = Y_{\text{in-o}} - \frac{G_{\text{io-o}}G_{\text{ci-o}}}{G_{\text{co-o}}} \tag{C.8}$$

In a corresponding manner, the feedback independence of $Y_{\text{in-sco}}$ is demonstrated by expressing the closed-loop short-circuit input admittance (C.9) using the internal transfer functions from (C.5) resulting (C.10), where the parameter $T_{\text{oi-}\infty} = T_{\text{oi-o}} + Z_{\text{o-o}}G_{\text{ci-o}}/G_{\text{co-o}}$. Based on the derivation, the open-loop representation for this parameter is obtained (C.11) demonstrating that this special parameter is independent of the state of the feedback.

$$Y_{\text{in-sco}} = Y_{\text{in-c}} + \frac{G_{\text{io-c}}T_{\text{oi-c}}}{Z_{\text{o-c}}} \tag{C.9}$$

$$\begin{aligned} Y_{\text{in-sco}} &= \frac{Y_{\text{in-o}}}{1+L_{\text{out}}} + \frac{L_{\text{out}}(Y_{\text{in-o}} - \frac{G_{\text{io-o}}G_{\text{ci-o}}}{G_{\text{co-o}}})}{1+L_{\text{out}}} + \frac{\frac{G_{\text{io-o}}}{1+L_{\text{out}}}(\frac{T_{\text{oi-o}}}{1+L_{\text{out}}} + \frac{L_{\text{out}}T_{\text{oi-o}}}{1+L_{\text{out}}} + \frac{L_{\text{out}}Z_{\text{o-o}}G_{\text{ci-o}}}{G_{\text{co-o}}(1+L_{\text{out}})})}{\frac{Z_{\text{o-o}}}{1+L_{\text{out}}}} \\ Y_{\text{in-sco}} &= Y_{\text{in-o}} - \frac{L_{\text{out}}G_{\text{io-o}}G_{\text{ci-o}}}{(1+L_{\text{out}})G_{\text{co-o}}} + \frac{G_{\text{io-o}}}{1+L_{\text{out}}}(T_{\text{oi-o}} + \frac{L_{\text{out}}Z_{\text{o-o}}G_{\text{ci-o}}}{(1+L_{\text{out}})G_{\text{co-o}}})\frac{1+L_{\text{out}}}{Z_{\text{o-o}}} \end{aligned} \tag{C.10}$$

$$Y_{\text{in-sco}} = Y_{\text{in-o}} + \frac{G_{\text{io-o}} T_{\text{oi-o}}}{Z_{\text{o-o}}} \tag{C.11}$$

D LOAD-AFFECTED DYNAMICS

The load influence to the internal dynamics in Fig. B.1 and (D.1) is assessed by representing the output current as given in (D.2). This representation is replaced to the internal dynamics in (D.3), resulting the output dynamics of (D.4) and after (D.5) the output dynamics is expressed as (D.6).

$$\begin{bmatrix} \hat{i}_{\mathrm{in}} \\ \hat{u}_{\mathrm{o}} \end{bmatrix} = \begin{bmatrix} Y_{\mathrm{in}} & T_{\mathrm{oi}} & G_{\mathrm{ci}} \\ G_{\mathrm{io}} & -Z_{\mathrm{o}} & G_{\mathrm{co}} \end{bmatrix} \begin{bmatrix} \hat{u}_{\mathrm{in}} \\ \hat{i}_{\mathrm{o}} \\ \hat{c} \end{bmatrix} \tag{D.1}$$

$$\hat{i}_{\mathrm{o}} = \hat{j}_{\mathrm{o}} - Y_{\mathrm{L}}\hat{u}_{\mathrm{o}} \tag{D.2}$$

$$\begin{aligned} \hat{i}_{\mathrm{in}} &= Y_{\mathrm{in}}\hat{u}_{\mathrm{in}} + T_{\mathrm{oi}}(\hat{j}_{\mathrm{o}} + Y_{\mathrm{L}}\hat{u}_{\mathrm{o}}) + G_{\mathrm{ci}}\hat{c} \\ \hat{u}_{\mathrm{o}} &= G_{\mathrm{io}}\hat{u}_{\mathrm{in}} - Z_{\mathrm{o}}(\hat{j}_{\mathrm{o}} + Y_{\mathrm{L}}\hat{u}_{\mathrm{o}}) + G_{\mathrm{co}}\hat{c} \end{aligned} \tag{D.3}$$

$$\hat{u}_{\mathrm{o}} = (\frac{G_{\mathrm{io}}}{1 + Z_{\mathrm{o}}Y_{\mathrm{L}}})\hat{u}_{\mathrm{in}} - (\frac{Z_{\mathrm{oi}}}{1 + Z_{\mathrm{o}}Y_{\mathrm{L}}})\hat{j}_{\mathrm{o}} + (\frac{G_{\mathrm{co}}}{1 + Z_{\mathrm{o}}Y_{\mathrm{L}}})\hat{c} \tag{D.4}$$

$$\begin{aligned} \hat{i}_{\mathrm{in}} = {} & (\frac{Y_{\mathrm{in}} + Y_{\mathrm{in}}Z_{\mathrm{o}}Y_{\mathrm{L}} + G_{\mathrm{io}}T_{\mathrm{oi}}Y_{\mathrm{L}}}{1 + Z_{\mathrm{o}}Y_{\mathrm{L}}})\hat{u}_{\mathrm{in}} + (\frac{T_{\mathrm{oi}} + T_{\mathrm{oi}}Y_{\mathrm{L}}Z_{\mathrm{o}} - T_{\mathrm{oi}}Z_{\mathrm{o}}Y_{\mathrm{L}}}{1 + Z_{\mathrm{o}}Y_{\mathrm{L}}})\hat{j}_{\mathrm{o}} \\ & + (\frac{T_{\mathrm{oi}}Y_{\mathrm{L}}G_{\mathrm{co}} + G_{\mathrm{ci}} + G_{\mathrm{ci}}Z_{\mathrm{o}}Y_{\mathrm{L}}}{1 + Z_{\mathrm{o}}Y_{\mathrm{L}}})\hat{c} \end{aligned} \tag{D.5}$$

$$\begin{aligned} \hat{i}_{\mathrm{in}} = {} & (\frac{1 + (Z_{\mathrm{o}} + \frac{T_{\mathrm{oi}}G_{\mathrm{io}}}{Y_{\mathrm{in}}})Y_{\mathrm{L}}}{1 + Z_{\mathrm{o}}Y_{\mathrm{L}}})\hat{u}_{\mathrm{in}} + (\frac{T_{\mathrm{oi}}}{1 + Z_{\mathrm{o}}Y_{\mathrm{L}}})\hat{j}_{\mathrm{o}} \\ & + (\frac{1 + (Z_{\mathrm{o}} + \frac{G_{\mathrm{co}}T_{\mathrm{oi}}}{G_{\mathrm{ci}}})Y_{\mathrm{L}}}{1 + Z_{\mathrm{o}}Y_{\mathrm{L}}})\hat{c} \end{aligned} \tag{D.6}$$

Based on these derivations, the load-affected system dynamics can be expressed as (D.7), where the expressions for the special output-side parameters $Z_{\text{o-oci}}$ (D.8) and $Z_{\text{o-}\infty}$ (D.9) are obtained from (D.6).

$$\begin{bmatrix} \hat{i}_{\text{in}} \\ \hat{u}_{\text{o}} \end{bmatrix} = \begin{bmatrix} \frac{1+Z_{\text{o-oci}}Y_{\text{L}}}{1+Z_{\text{o}}Y_{\text{L}}}Y_{\text{in}} & \frac{T_{\text{oi}}}{1+Z_{\text{o}}Y_{\text{L}}} & \frac{1+Z_{\text{o-}\infty}Y_{\text{L}}}{1+Z_{\text{o}}Y_{\text{L}}}G_{\text{ci}} \\ \frac{G_{\text{io}}}{1+Z_{\text{o}}Y_{\text{L}}} & -\frac{Z_{\text{o}}}{1+Z_{\text{o}}Y_{\text{L}}} & \frac{G_{\text{co}}}{1+Z_{\text{o}}Y_{\text{L}}} \end{bmatrix} \begin{bmatrix} \hat{u}_{\text{in}} \\ \hat{j}_{\text{o}} \\ \hat{c} \end{bmatrix} \tag{D.7}$$

$$Z_{\text{o-oci}} = Z_{\text{o}} + \frac{G_{\text{io}}T_{\text{oi}}}{Y_{\text{in}}} \tag{D.8}$$

$$Z_{\text{o-}\infty} = Z_{\text{o}} + \frac{G_{\text{co}}T_{\text{oi}}}{G_{\text{ci}}} \tag{D.9}$$

E LOAD-SIDE SPECIAL PARAMETERS

The extraction of the load-side special parameters from the two-port model is provided in this appendix. In addition, the dependence of both parameters to the output-side feedback is stated.

E.1 Extraction of special parameters $Z_{\text{o-oci}}$ and $Z_{\text{o-}\infty}$

The open-circuit output impedance is extracted from original internal dynamics under the condition: $\hat{\hat{i}}_{\text{in}} = 0$ and $\hat{c} = 0$ in (E.1) and solving the corresponding output impedance (E.2).

$$\begin{aligned} 0 &= T_{\text{oi}}\hat{\hat{i}}_{\text{o}} + Y_{\text{in}}\hat{u}_{\text{in}} \\ \hat{u}_{\text{o}} &= G_{\text{io}}\hat{u}_{\text{in}} - Z_{\text{o}}\hat{\hat{i}}_{\text{o}} \end{aligned} \tag{E.1}$$

$$Z_{\text{o-oci}} = -\frac{\hat{u}_{\text{o}}}{\hat{\hat{i}}_{\text{o}}} = Z_{\text{o}} + \frac{G_{\text{io}}T_{\text{oi}}}{Y_{\text{in}}} \tag{E.2}$$

In a similar way, the ideal output impedance can be obtained under the condition: $\hat{u}_{\text{in}} = 0$ and $\hat{\hat{i}}_{\text{in}} = 0$ according to (E.3). The corresponding impedance is obtained in (E.4).

$$\begin{aligned} 0 &= T_{\text{oi}}\hat{\hat{i}}_{\text{o}} + G_{\text{ci}}\hat{c} \\ \hat{u}_{\text{o}} &= -Z_{\text{o}}\hat{\hat{i}}_{\text{o}} + G_{\text{co}}\hat{c} \end{aligned} \tag{E.3}$$

$$Z_{\text{o-}\infty} = -\frac{\hat{u}_{\text{o}}}{\hat{\hat{i}}_{\text{o}}} = Z_{\text{o}} + \frac{G_{\text{co}}T_{\text{oi}}}{G_{\text{ci}}} \tag{E.4}$$

E.2 Parameter dependence of the feedback

The dependence or independence of both special parameters on the state-of-feedback is assessed utilizing the dynamical expression provided in (C.5). First, the closed-loop

$Z_{\text{o-}\infty}$ (E.5) independence on the state-of-feedback is demonstrated by using the internal dynamics from (C.5) and resulting a representation as in (E.6). Finally, the ideal output impedance consisting of the open-loop transfer functions is obtained in (E.7) thus demonstrating that the special parameter is independent of the state of the feedback.

$$Z_{\text{o-}\infty} = Z_{\text{o-c}} + \frac{G_{\text{co-c}} T_{\text{oi-c}}}{G_{\text{ci-c}}} \tag{E.5}$$

$$\begin{aligned} Z_{\text{o-}\infty} &= \frac{Z_{\text{o-o}}}{1 + L_{\text{out}}} + \frac{\frac{L_{\text{out}}}{G_{\text{se}}(1+L_{\text{out}})}(T_{\text{oi-o}} + \frac{L_{\text{out}} Z_{\text{o-o}} G_{\text{ci-o}}}{G_{\text{co}}(1+L_{\text{out}})})}{\frac{G_{\text{ci-o}}}{G_{\text{se}} G_{\text{co-o}}} \frac{L_{\text{out}}}{1+L_{\text{out}}}} \\ Z_{\text{o-}\infty} &= \frac{Z_{\text{o-o}}}{1 + L_{\text{out}}} + \frac{T_{\text{oi-o}} G_{\text{co-o}}}{G_{\text{ci-o}}} + \frac{L_{\text{out}} Z_{\text{o-o}}}{1 + L_{\text{out}}} \end{aligned} \tag{E.6}$$

$$Z_{\text{o-}\infty} = Z_{\text{o-o}} + \frac{T_{\text{oi-o}} G_{\text{co-o}}}{G_{\text{ci-o}}} \tag{E.7}$$

The open-circuit output impedance is dependent on the state of the output-side feedback. This dependence can be illustrated by representing the closed-loop $Z_{\text{o-oci}}$ (E.8) using the internal dynamics from (C.5) resulting (E.9). Therefore, the open-circuit output impedance has different values at open and closed- loop according to (E.10).

$$Z_{\text{o-oci}} = Z_{\text{o-c}} + \frac{G_{\text{io-c}} T_{\text{oi-c}}}{Y_{\text{in-c}}} \tag{E.8}$$

$$\begin{aligned} Z_{\text{o-oci}} &= \frac{Z_{\text{o-o}}}{1 + L_{\text{out}}} + (\frac{T_{\text{oi-o}} + \frac{L_{\text{out}} Z_{\text{o-o}} G_{\text{ci-o}}}{G_{\text{co-o}}}(1 + L_{\text{out}})}{Y_{\text{in-o}} + \frac{L_{\text{out}} G_{\text{ci-o}} G_{\text{io-o}}}{G_{\text{co-o}}(1+L_{\text{out}})}})(\frac{G_{\text{io-o}}}{1 + L_{\text{out}}}) \\ Z_{\text{o-oci}} &= \frac{Z_{\text{o-o}}}{1 + L_{\text{out}}} + \frac{T_{\text{oi-o}}}{Y_{\text{in-o}}}(\frac{1 + L_{\text{out}} \frac{T_{\text{oi-o}} G_{\text{co-o}} + Z_{\text{o-o}} G_{\text{ci-o}}}{G_{\text{co-o}} T_{\text{oi-o}}}}{(1 + L_{\text{out}}) \frac{Y_{\text{in-o}} G_{\text{co-o}} + G_{\text{ci-o}} G_{\text{io-o}}}{G_{\text{co-o}} Y_{\text{in-o}}}}(\frac{G_{\text{io-o}}}{1 + L_{\text{out}}}) \end{aligned} \tag{E.9}$$

$$\begin{aligned} Z^{o}_{\text{o-oci}} &= \frac{Z_{\text{o-o}}}{Y_{\text{in-o}}} Y_{\text{in-sco}} \\ Z^{c}_{\text{o-oci}} &= \frac{Z_{\text{o-c}}}{Y_{\text{in-c}}} Y_{\text{in-sco}} \end{aligned} \tag{E.10}$$

F OPEN-LOOP DYNAMICS OF VM AND IVFF CONTROLLED CONVERTER

The open-loop dynamics of VM and IVFF- controlled converter are given in this appendix.

F.1 VM-controlled converter

The open-loop dynamics associated with the voltage-mode controlled converter are given in (F.1), where the equivalent parameters r_{E} and U_{E} are defined as (F.2) and (F.3) including the parasitics.

$$\begin{bmatrix} \hat{i}_{\mathrm{in}} \\ \hat{u}_{\mathrm{o}} \end{bmatrix} = \frac{\begin{bmatrix} \frac{D^2 s}{L} & \frac{D(1+sr_{\mathrm{c}}C)}{LC} & \frac{DU_{\mathrm{E}}s}{L} \\ \frac{D(1+sr_{\mathrm{c}}C)}{LC} & -\frac{(r_{\mathrm{E}}+sL)(1+sr_{\mathrm{c}}C)}{LC} & \frac{U_{\mathrm{E}}(1+sr_{\mathrm{c}}C)}{LC} \end{bmatrix}}{s^2 + s\frac{r_{\mathrm{E}}+r_{\mathrm{c}}}{L} + \frac{1}{LC}} + \begin{bmatrix} 0 & 0 & I_{\mathrm{o}} \\ 0 & 0 & 0 \end{bmatrix} \begin{bmatrix} \hat{u}_{\mathrm{in}} \\ \hat{i}_{\mathrm{o}} \\ \hat{c} \end{bmatrix} \tag{F.1}$$

$$r_{\mathrm{E}} = r_{\mathrm{L}} + Dr_{\mathrm{ds1}} + Dr_{\mathrm{d}} \tag{F.2}$$

$$U_{\mathrm{E}} = U_{\mathrm{in}} + U_{\mathrm{D}} + (r_{\mathrm{d}} - r_{\mathrm{ds1}})I_{\mathrm{o}} \tag{F.3}$$

F.2 IVFF-controlled converter

The open-loop dynamics of the IVFF-controlled converter are given in (F.4), where the parameters $F_{\mathrm{m}}^{\mathrm{IF}}$ and $q_{\mathrm{i}}^{\mathrm{IF}}$ are defined in (F.6) and (F.7), where R_{x} and C_{x} are the PWM

modulator time-base components (Karppanen et al., 2007a).

$$\begin{bmatrix} \hat{i}_{\mathrm{in}} \\ \hat{u}_{\mathrm{o}} \end{bmatrix} = \frac{\begin{bmatrix} \frac{D(D-F_{\mathrm{m}}^{\mathrm{IF}} q_{\mathrm{i}}^{\mathrm{IF}} U_{\mathrm{E}})s}{L} & \frac{D(1+sr_{\mathrm{c}}C)}{LC} & \frac{F_{\mathrm{m}}^{\mathrm{IF}} DU_{\mathrm{E}}s}{L} \\ \frac{(D-F_{\mathrm{m}}^{\mathrm{IF}} q_{\mathrm{i}}^{\mathrm{IF}} U_{\mathrm{E}})(1+sr_{\mathrm{c}}C)}{LC} & -\frac{(r_{\mathrm{E}}+sL)(1+sr_{\mathrm{c}}C)}{LC} & \frac{F_{\mathrm{m}}^{\mathrm{IF}} U_{\mathrm{E}}(1+sr_{\mathrm{c}}C)}{LC} \end{bmatrix}}{s^2 + s\frac{r_{\mathrm{E}}+r_{\mathrm{c}}}{L} + \frac{1}{LC}} + \tag{F.4}$$

$$\begin{bmatrix} -F_{\mathrm{m}}^{\mathrm{IF}} q_{\mathrm{i}}^{\mathrm{IF}} I_{\mathrm{o}} & 0 & F_{\mathrm{m}}^{\mathrm{IF}} I_{\mathrm{o}} \\ 0 & 0 & 0 \end{bmatrix} \begin{bmatrix} \hat{u}_{\mathrm{in}} \\ \hat{i}_{\mathrm{o}} \\ \hat{c} \end{bmatrix} \tag{F.5}$$

$$F_{\mathrm{m}}^{\mathrm{IF}} = \frac{R_{\mathrm{x}} C_{\mathrm{x}}}{T_{\mathrm{s}} U_{\mathrm{in}}} \tag{F.6}$$

$$q_{\mathrm{i}}^{\mathrm{IF}} = \frac{DT_{\mathrm{s}}}{R_{\mathrm{x}} C_{\mathrm{x}}} \tag{F.7}$$

G OPEN-LOOP DYNAMICS OF PCM AND OCF-CONTROLLED CONVERTER

The open-loop dynamics of PCM and OCF-controlled converter are given in this appendix.

G.1 PCM-controlled converter

The open-loop dynamics associated with the peak-current-mode controlled converter are given in (G.1), where the parameters $F_{\mathrm{m}}^{\mathrm{PC}}$, $q_{\mathrm{c}}^{\mathrm{PC}}$ and $q_{\mathrm{i}}^{\mathrm{PC}}$ are defined as (G.2), (G.3) and (G.4), respectively (Karppanen et al., 2007b). In addition, the inductor current slope compensation M_{c} is defined as in (G.5)

$$\begin{bmatrix} \hat{i}_{\mathrm{in}} \\ \hat{u}_{\mathrm{o}} \end{bmatrix} = \frac{\begin{bmatrix} \frac{(D-F_{\mathrm{m}}^{\mathrm{PC}}q_{\mathrm{i}}^{\mathrm{PC}}U_{\mathrm{E}})(D-F_{\mathrm{m}}^{\mathrm{PC}}q_{\mathrm{c}}^{\mathrm{PC}}I_{\mathrm{o}})s}{L} & \frac{(D-F_{\mathrm{m}}^{\mathrm{PC}}q_{\mathrm{c}}^{\mathrm{PC}}I_{\mathrm{o}})(1+sr_{\mathrm{c}}C)}{LC} & \frac{F_{\mathrm{m}}^{\mathrm{PC}}U_{\mathrm{E}}(D-F_{\mathrm{m}}^{\mathrm{PC}}q_{\mathrm{c}}^{\mathrm{PC}}I_{\mathrm{o}})s}{L} \\ \frac{(D-F_{\mathrm{m}}^{\mathrm{PC}}q_{\mathrm{i}}^{\mathrm{PC}}U_{\mathrm{E}})(1+sr_{\mathrm{c}}C)}{LC} & -\frac{(r_{\mathrm{E}}+F_{\mathrm{m}}^{\mathrm{PC}}q_{\mathrm{c}}^{\mathrm{PC}}U_{\mathrm{E}}+sL)(1+sr_{\mathrm{c}}C)}{LC} & \frac{F_{\mathrm{m}}^{\mathrm{PC}}U_{\mathrm{E}}(1+sr_{\mathrm{c}}C)}{LC} \end{bmatrix}}{s^2 + s\frac{r_{\mathrm{E}}+F_{\mathrm{m}}^{\mathrm{PC}}q_{\mathrm{c}}^{\mathrm{PC}}U_{\mathrm{E}}+r_{\mathrm{c}}}{L} + \frac{1}{LC}} \begin{bmatrix} -F_{\mathrm{m}}^{\mathrm{PC}}q_{\mathrm{i}}^{\mathrm{PC}}I_{\mathrm{o}} & 0 & F_{\mathrm{m}}^{\mathrm{PC}}I_{\mathrm{o}} \\ 0 & 0 & 0 \end{bmatrix} \begin{bmatrix} \hat{u}_{\mathrm{in}} \\ \hat{i}_{\mathrm{o}} \\ \hat{c} \end{bmatrix} \tag{G.1}$$

$$F_{\mathrm{m}}^{\mathrm{PC}} = \frac{2L}{T_{\mathrm{s}}(2LM_{\mathrm{c}} + (D1 - D)U_{\mathrm{E}})} \tag{G.2}$$

$$q_{\mathrm{c}}^{\mathrm{PC}} = 1 + \frac{DD1T_{\mathrm{s}}}{2L}(r_{\mathrm{d}} - r_{\mathrm{ds1}}) \tag{G.3}$$

$$q_{\mathrm{i}}^{\mathrm{PC}} = \frac{DD1T_{\mathrm{s}}}{2L} \tag{G.4}$$

$$M_{\mathrm{c}} = \frac{DU_{\mathrm{E}}}{2L} \tag{G.5}$$

G.2 OCF -controlled converter

The open-loop dynamics of the PCM-controlled converter with output current feedforward can be given as in (G.6) and where the parameters $F_{\mathrm{m}}^{\mathrm{PC}}$, $q_{\mathrm{c}}^{\mathrm{PC}}$ and $q_{\mathrm{i}}^{\mathrm{PC}}$ are as previously defined in (G.2), (G.3) and (G.4) (Karppanen et al., 2007b).

$$\begin{bmatrix} \hat{i}_{\mathrm{in}} \\ \hat{u}_{\mathrm{o}} \end{bmatrix} = \frac{\begin{bmatrix} \frac{(D-F_{\mathrm{m}}^{\mathrm{PC}}q_{\mathrm{i}}^{\mathrm{PC}}U_{\mathrm{E}})(D-F_{\mathrm{m}}^{\mathrm{PC}}I_{\mathrm{o}})s}{L} & \frac{(D-F_{\mathrm{m}}^{\mathrm{PC}}I_{\mathrm{o}})(1+s(r_{\mathrm{c}}+F_{\mathrm{m}}^{\mathrm{PC}}U_{\mathrm{E}})C)}{LC} & \frac{F_{\mathrm{m}}^{\mathrm{PC}}U_{\mathrm{E}}(D-F_{\mathrm{m}}^{\mathrm{PC}}I_{\mathrm{o}})s}{R_{\mathrm{s1}}L} \\ \frac{(D-F_{\mathrm{m}}^{\mathrm{PC}}q_{\mathrm{i}}^{\mathrm{PC}}U_{\mathrm{E}})(1+sr_{\mathrm{c}}C)}{LC} & -\frac{(r_{\mathrm{E}}+sL)(1+sr_{\mathrm{c}}C)}{LC} & \frac{F_{\mathrm{m}}^{\mathrm{PC}}U_{\mathrm{E}}(1+sr_{\mathrm{c}}C)}{R_{\mathrm{s1}}LC} \end{bmatrix}}{s^2 + s\frac{r_{\mathrm{E}}+F_{\mathrm{m}}^{\mathrm{PC}}U_{\mathrm{E}}+r_{\mathrm{c}}}{L} + \frac{1}{LC}} \begin{bmatrix} -F_{\mathrm{m}}^{\mathrm{PC}}q_{\mathrm{i}}^{\mathrm{IF}}I_{\mathrm{o}} & F_{\mathrm{m}}^{\mathrm{PC}}I_{\mathrm{o}} & \frac{F_{\mathrm{m}}^{\mathrm{PC}}I_{\mathrm{o}}}{R_{\mathrm{s1}}} \\ 0 & 0 & 0 \end{bmatrix} \begin{bmatrix} \hat{u}_{\mathrm{in}} \\ \hat{i}_{\mathrm{o}} \\ \hat{c} \end{bmatrix} \tag{G.6}$$

H SOURCE-AFFECTED SYSTEM-LEVEL DYNAMICS

The dynamical model of the input-parallel connected converters with a common input filter is shown in Fig. H.1. The internal dynamics of this system structure is emphasized with dashed lines and provided in (H.1). The source and load are assumed ideal and the system input admittance is $Y_{\mathrm{in}} = Y_{\mathrm{in1}} + Y_{\mathrm{in2}}$.

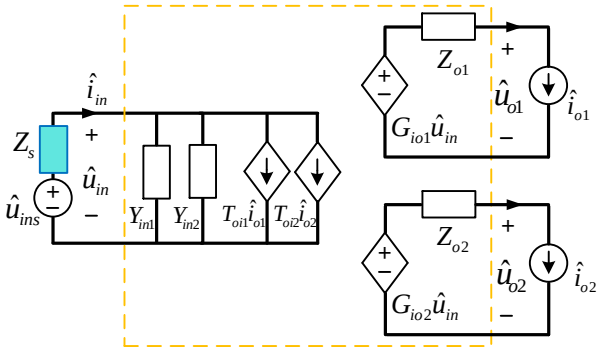

Fig. H.1: Two-port model of the system structure.

$$\begin{bmatrix} \hat{i}_{\mathrm{in}} \\ \hat{u}_{\mathrm{o1}} \\ \hat{u}_{\mathrm{o2}} \end{bmatrix} = \begin{bmatrix} Y_{\mathrm{in}} & T_{\mathrm{oi1}} & T_{\mathrm{oi2}} \\ G_{\mathrm{io1}} & -Z_{\mathrm{oi1}} & 0 \\ G_{\mathrm{io2}} & 0 & -Z_{\mathrm{oi2}} \end{bmatrix} \begin{bmatrix} \hat{u}_{\mathrm{in}} \\ \hat{i}_{\mathrm{o1}} \\ \hat{i}_{\mathrm{o2}} \end{bmatrix} \tag{H.1}$$

The influence of the filter output impedance,Z_{s}, to the system dynamics is assessed by representing the input voltage as given in (H.2). This representation is replaced to the internal dynamics in (H.3). This results input dynamics as given in (H.4). The output voltage $\hat{u}_{\mathrm{o1}}$ is provided in (H.5) resulting (H.6) and the output voltage $\hat{u}_{\mathrm{o2}}$ is defined in (H.7) resulting to (H.8).

$$\hat{u}_{\text{in}} = \hat{u}_{\text{ins}} - Z_{\text{s}}\hat{i}_{\text{in}} \tag{H.2}$$

$$\begin{aligned}
\hat{i}_{\text{in}} &= Y_{\text{in}}(\hat{u}_{\text{ins}} - Z_{\text{s}}\hat{i}_{\text{in}}) + T_{\text{oi1}}\hat{i}_{\text{o1}} + T_{\text{oi2}}\hat{i}_{\text{o2}}) \\
\hat{u}_{\text{o1}} &= G_{\text{io1}}(\hat{u}_{\text{ins}} - Z_{\text{s}}\hat{i}_{\text{in}}) - Z_{\text{o1}}\hat{i}_{\text{o1}} \\
\hat{u}_{\text{o2}} &= G_{\text{io2}}(\hat{u}_{\text{ins}} - Z_{\text{s}}\hat{i}_{\text{in}}) - Z_{\text{o2}}\hat{i}_{\text{o2}}
\end{aligned} \tag{H.3}$$

$$\hat{i}_{\text{in}} = (\frac{Y_{\text{in}}}{1 + Z_{\text{s}}Y_{\text{in}}})\hat{u}_{\text{ins}} + (\frac{T_{\text{oi1}}}{1 + Z_{\text{s}}Y_{\text{in}}})\hat{i}_{\text{o1}} + (\frac{T_{\text{oi2}}}{1 + Z_{\text{s}}Y_{\text{in}}})\hat{i}_{\text{o2}} \tag{H.4}$$

$$\begin{aligned}
\hat{u}_{\text{o1}} = &(\frac{G_{\text{io1}} + G_{\text{io1}}Z_{\text{s}}Y_{\text{in}} - G_{\text{io1}}Z_{\text{s}}Y_{\text{in}}}{1 + Z_{\text{s}}Y_{\text{in}}})\hat{u}_{\text{ins}} - (\frac{Z_{\text{s}}G_{\text{io1}}T_{\text{oi1}} + Z_{\text{o1}} + Z_{\text{o1}}Z_{\text{s}}Y_{\text{in}}}{1 + Z_{\text{s}}Y_{\text{in}}})\hat{i}_{\text{o1}} \\
&- (\frac{G_{\text{io1}}Z_{\text{s}}T_{\text{oi2}}}{1 + Z_{\text{s}}Y_{\text{in}}})\hat{i}_{\text{o2}}
\end{aligned} \tag{H.5}$$

$$\begin{aligned}
\hat{u}_{\text{o1}} = &(\frac{G_{\text{io1}}}{1 + Z_{\text{s}}Y_{\text{in}}})\hat{u}_{\text{ins}} - (\frac{1 + Z_{\text{s}}(Y_{\text{in2}} + Y_{\text{in1}} + \frac{G_{\text{io1}}T_{\text{oi1}}}{Z_{\text{o1}}})}{1 + Z_{\text{s}}Y_{\text{in}}})Z_{\text{o1}}\hat{i}_{\text{o1}} \\
&- (\frac{G_{\text{io1}}Z_{\text{s}}T_{\text{io2}}}{1 + Z_{\text{s}}Y_{\text{in}}})\hat{i}_{\text{o2}}
\end{aligned} \tag{H.6}$$

$$\begin{aligned}
\hat{u}_{\text{o2}} = &(\frac{G_{\text{io2}} + G_{\text{io2}}Z_{\text{s}}Y_{\text{in}} - G_{\text{io2}}Z_{\text{s}}Y_{\text{in}}}{1 + Z_{\text{s}}Y_{\text{in}}})\hat{u}_{\text{ins}} - (\frac{G_{\text{io2}}Z_{\text{s}}T_{\text{oi1}}}{1 + Z_{\text{s}}Y_{\text{in}}})\hat{i}_{\text{o1}} \\
&- (\frac{Z_{\text{s}}G_{\text{io2}}T_{\text{oi2}} + Z_{\text{o2}} + Z_{\text{o2}}Z_{\text{s}}Y_{\text{in}}}{1 + Z_{\text{s}}Y_{\text{in}}})\hat{i}_{\text{o2}}
\end{aligned} \tag{H.7}$$

$$\begin{aligned}
\hat{u}_{\text{o2}} = &(\frac{G_{\text{io2}}}{1 + Z_{\text{s}}Y_{\text{in}}})\hat{u}_{\text{ins}} - (\frac{G_{\text{io2}}Z_{\text{s}}T_{\text{oi1}}}{1 + Z_{\text{s}}Y_{\text{in}}})\hat{i}_{\text{o1}} \\
&- (\frac{1 + Z_{\text{s}}(Y_{\text{in1}} + Y_{\text{in2}} + \frac{G_{\text{io2}}T_{\text{oi2}}}{Z_{\text{o2}}})}{1 + Z_{\text{s}}Y_{\text{in}}})Z_{\text{o2}}\hat{i}_{\text{o2}}
\end{aligned} \tag{H.8}$$

Based on these derivations, the source-affected system dynamics can be expressed as (H.9), where the expressions for the special input-side parameters $Y^{\text{S}}_{\text{in-sco1}}$ and $Y^{\text{S}}_{\text{in-sco2}}$

(H.10) are obtained from (H.6) and (H.8), respectively.

$$\begin{bmatrix} \hat{i}_{\mathrm{in}} \\ \hat{u}_{\mathrm{o1}} \\ \hat{u}_{\mathrm{o2}} \end{bmatrix} = \begin{bmatrix} \frac{Y_{\mathrm{in}}}{1+Z_{\mathrm{s}}Y_{\mathrm{in}}} & \frac{T_{\mathrm{oi1}}}{1+Z_{\mathrm{s}}Y_{\mathrm{in}}} & \frac{T_{\mathrm{oi2}}}{1+Z_{\mathrm{s}}Y_{\mathrm{in}}} \\ \frac{G_{\mathrm{io1}}}{1+Z_{\mathrm{s}}Y_{\mathrm{in}}} & -(\frac{1+Z_{\mathrm{s}}Y^{\mathrm{S}}_{\text{in-sco1}}}{1+Z_{\mathrm{s}}Y_{\mathrm{in}}})Z_{\mathrm{o1}} & -\frac{G_{\mathrm{io1}}T_{\mathrm{oi2}}Z_{\mathrm{s}}}{1+Z_{\mathrm{s}}Y_{\mathrm{in}}} \\ \frac{G_{\mathrm{io2}}}{1+Z_{\mathrm{s}}Y_{\mathrm{in}}} & -\frac{G_{\mathrm{io2}}T_{\mathrm{oi1}}Z_{\mathrm{s}}}{1+Z_{\mathrm{s}}Y_{\mathrm{in}}} & -(\frac{1+Z_{\mathrm{s}}Y^{\mathrm{S}}_{\text{in-sco2}}}{1+Z_{\mathrm{s}}Y_{\mathrm{in}}})Z_{\mathrm{o2}} \end{bmatrix} \begin{bmatrix} \hat{u}_{\mathrm{ins}} \\ \hat{i}_{\mathrm{o1}} \\ \hat{i}_{\mathrm{o2}} \end{bmatrix} \tag{H.9}$$

$$\begin{aligned} Y^{\mathrm{S}}_{\text{in-sco1}} &= Y_{\text{in-sco1}} + Y_{\mathrm{in2}} \\ Y^{\mathrm{S}}_{\text{in-sco2}} &= Y_{\text{in-sco2}} + Y_{\mathrm{in1}} \end{aligned} \tag{H.10}$$

I LOAD-AFFECTED SYSTEM-LEVEL DYNAMICS

The source-affected dynamics of the system-level model of Fig. H.1, including the cross-coupling impedance as provided in (I.1).

$$\begin{bmatrix} \hat{i}_{\mathrm{in}} \\ \hat{u}_{\mathrm{o1}} \\ \hat{u}_{\mathrm{o2}} \end{bmatrix} = \begin{bmatrix} Y_{\mathrm{in}}^{\mathrm{S}} & T_{\mathrm{oi1}}^{\mathrm{S}} & T_{\mathrm{oi2}}^{\mathrm{S}} \\ G_{\mathrm{io1}}^{\mathrm{S}} & -Z_{\mathrm{oi1}}^{\mathrm{S}} & G_{\mathrm{cr1}}^{\mathrm{S}} \\ G_{\mathrm{io2}}^{\mathrm{S}} & G_{\mathrm{cr2}}^{\mathrm{S}} & -Z_{\mathrm{oi2}}^{\mathrm{S}} \end{bmatrix} \begin{bmatrix} \hat{u}_{\mathrm{ins}} \\ \hat{i}_{\mathrm{o1}} \\ \hat{i}_{\mathrm{o2}} \end{bmatrix} \tag{I.1}$$

The load influence at both outputs to the system dynamics is assessed separately. The load 1 influence is analyzed by representing $\hat{i}_{\mathrm{o1}}$ as given in (I.2) and by replacing it to the internal dynamics as given in (I.3). The output voltage $\hat{u}_{\mathrm{o1}}$ is obtained as (I.4), and thereafter, the $\hat{u}_{\mathrm{o2}}$ and $\hat{i}_{\mathrm{in}}$ can be expressed as (I.5) and (I.6), respectively.

$$\hat{i}_{\mathrm{o1}} = \hat{j}_{\mathrm{o1}} - Y_{\mathrm{L1}}\hat{u}_{\mathrm{o1}} \tag{I.2}$$

$$\begin{aligned} \hat{i}_{\mathrm{in}} &= Y_{\mathrm{in}}^{\mathrm{S}}\hat{u}_{\mathrm{ins}} + T_{\mathrm{oi1}}^{\mathrm{S}}(\hat{j}_{\mathrm{o1}} + Y_{\mathrm{L1}}^{\mathrm{S}}\hat{u}_{\mathrm{o1}}) + T_{\mathrm{oi2}}^{\mathrm{S}}\hat{i}_{\mathrm{o2}} \\ \hat{u}_{\mathrm{o1}} &= G_{\mathrm{io1}}^{\mathrm{S}}\hat{u}_{\mathrm{ins}} - Z_{\mathrm{o1}}^{\mathrm{S}}(\hat{j}_{\mathrm{o1}} + Y_{\mathrm{L1}}^{\mathrm{S}}\hat{u}_{\mathrm{o1}}) + G_{\mathrm{cr1}}^{\mathrm{S}}\hat{i}_{\mathrm{o2}} \\ \hat{u}_{\mathrm{o2}} &= G_{\mathrm{io2}}^{\mathrm{S}}\hat{u}_{\mathrm{ins}} + G_{\mathrm{cr2}}^{\mathrm{S}}(\hat{j}_{\mathrm{o1}} + Y_{\mathrm{L1}}^{\mathrm{S}}\hat{u}_{\mathrm{o1}}) - Z_{\mathrm{o2}}^{\mathrm{S}}\hat{i}_{\mathrm{o2}} \end{aligned} \tag{I.3}$$

$$\hat{u}_{\mathrm{o1}} = \left(\frac{G_{\mathrm{io1}}^{\mathrm{S}}}{1 + Z_{\mathrm{o1}}^{\mathrm{S}}Y_{\mathrm{L1}}^{\mathrm{S}}}\right)\hat{u}_{\mathrm{ins}} - \left(\frac{Z_{\mathrm{oi1}}^{\mathrm{S}}}{1 + Z_{\mathrm{o1}}^{\mathrm{S}}Y_{\mathrm{L1}}}\right)\hat{j}_{\mathrm{o1}} + \left(\frac{G_{\mathrm{cr1}}^{\mathrm{S}}}{1 + Z_{\mathrm{o1}}^{\mathrm{S}}Y_{\mathrm{L1}}}\right)\hat{i}_{\mathrm{o2}} \tag{I.4}$$

$$\begin{aligned} \hat{u}_{\mathrm{o2}} = &\left(G_{\mathrm{io2}}^{\mathrm{S}} + \frac{G_{\mathrm{io1}}^{\mathrm{S}}G_{\mathrm{cr2}}^{\mathrm{S}}Y_{\mathrm{L1}}}{1 + Z_{\mathrm{o1}}^{\mathrm{S}}Y_{\mathrm{L1}}}\right)\hat{u}_{\mathrm{ins}} + \left(\frac{G_{\mathrm{cr2}}^{\mathrm{S}}(1 + Z_{\mathrm{o1}}^{\mathrm{S}}Y_{\mathrm{L1}}) - G_{\mathrm{cr2}}^{\mathrm{S}}Z_{\mathrm{o1}}^{\mathrm{S}}Y_{\mathrm{L1}}}{1 + Z_{\mathrm{o1}}^{\mathrm{S}}Y_{\mathrm{L1}}}\right)\hat{j}_{\mathrm{o1}} \\ &- \left(Z_{\mathrm{o2}}^{\mathrm{S}} - \frac{G_{\mathrm{cr2}}^{\mathrm{S}}G_{\mathrm{cr1}}^{\mathrm{S}}Y_{\mathrm{L1}}}{1 + Z_{\mathrm{o1}}^{\mathrm{S}}Y_{\mathrm{L1}}}\right)\hat{i}_{\mathrm{o2}} \end{aligned} \tag{I.5}$$

$$\hat{i}_{\text{in}} = (\frac{Y^{\text{S}}_{\text{in}}(1 + Z^{\text{S}}_{\text{o1}}Y_{\text{L1}}) + Y_{\text{L1}}T^{\text{S}}_{\text{oi1}}G^{\text{S}}_{\text{io1}}}{1 + Z^{\text{S}}_{\text{o1}}Y_{\text{L1}}})\hat{u}_{\text{ins}} + (\frac{T^{\text{S}}_{\text{oi1}}(1 + Z^{\text{S}}_{\text{o1}}Y_{\text{L1}}) - T^{\text{S}}_{\text{oi1}}Y_{\text{L1}}Z^{\text{S}}_{\text{o1}}}{1 + Z^{\text{S}}_{\text{o1}}Y_{\text{L1}}})\hat{j}_{\text{o1}} + (\frac{T^{\text{S}}_{\text{oi1}}Y_{\text{L1}}G^{\text{S}}_{\text{cr1}} + T^{\text{S}}_{\text{oi2}}}{1 + Z_{\text{o1}}Y_{\text{L1}}})\hat{i}_{\text{o2}} \tag{I.6}$$

Based on these derivations, Y_{L1} influence to the system dynamics is given in (I.7), where the expression for the special output-side parameters $Z^{\text{S}}_{\text{o-oci1}}$ (I.8) is obtained from (I.6).

$$\begin{bmatrix} \hat{i}_{\text{in}} \\ \hat{u}_{\text{o1}} \\ \hat{u}_{\text{o2}} \end{bmatrix} = \begin{bmatrix} \frac{1+Z^{\text{S}}_{\text{o-oci1}}Y_{\text{L1}}}{1+Z^{\text{S}}_{\text{o1}}Y_{\text{L1}}}Y^{\text{S}}_{\text{in1}} + Y^{\text{S}}_{\text{in2}} & \frac{T^{\text{S}}_{\text{oi1}}}{1+Z^{\text{S}}_{\text{o1}}Y_{\text{L1}}} & \frac{Y_{\text{L1}}G^{\text{S}}_{\text{cr1}}T^{\text{S}}_{\text{oi1}}}{1+Z^{\text{S}}_{\text{o1}}Y_{\text{L1}}} + T^{\text{S}}_{\text{oi2}} \\ \frac{G^{\text{S}}_{\text{io1}}}{1+Z^{\text{S}}_{\text{o1}}Y_{\text{L1}}} & -\frac{Z^{\text{S}}_{\text{o1}}}{1+Z_{\text{o1}}Y_{\text{L1}}} & \frac{G^{\text{S}}_{\text{cr1}}}{1+Z^{\text{S}}_{\text{o1}}Y_{\text{L1}}} \\ G^{\text{S}}_{\text{io2}} + \frac{Y_{\text{L1}}G^{\text{S}}_{\text{io1}}G^{\text{S}}_{\text{cr2}}}{1+Z^{\text{S}}_{\text{o1}}Y_{\text{L1}}} & \frac{G^{\text{S}}_{\text{cr2}}}{1+Z^{\text{S}}_{\text{o1}}Y_{\text{L1}}} & -(Z^{\text{S}}_{\text{o2}} - \frac{Y_{\text{L1}}G^{\text{S}}_{\text{cr1}}G^{\text{S}}_{\text{cr2}}}{1+Z^{\text{S}}_{\text{o1}}Y_{\text{L1}}}) \end{bmatrix} \begin{bmatrix} \hat{u}_{\text{ins}} \\ \hat{j}_{\text{o1}} \\ \hat{j}_{\text{o2}} \end{bmatrix} \tag{I.7}$$

$$Z^{\text{S}}_{\text{o-oci1}} = Z^{\text{S}}_{\text{o1}} + \frac{G^{\text{S}}_{\text{io1}}T^{\text{S}}_{\text{oi1}}}{Y^{\text{S}}_{\text{in1}}} \tag{I.8}$$

In a similar way the load 2 influence is analyzed representing the $\hat{i}_{\text{o2}}$ as given in (I.9) and by replacing it to the internal dynamics as given in (I.10). The output voltage $\hat{u}_{\text{o2}}$ is obtained as (I.11), and thereafter, the $\hat{u}_{\text{o1}}$ and $\hat{i}_{\text{in}}$ can be expressed as (I.12) and (I.13), respectively.

$$\hat{i}_{\text{o2}} = \hat{j}_{\text{o2}} - Y_{\text{L2}}\hat{u}_{\text{o2}} \tag{I.9}$$

$$
\begin{aligned}
\hat{i}_{\mathrm{in}} &= Y^{\mathrm{S}}_{\mathrm{in}}\hat{u}_{\mathrm{ins}} + T^{\mathrm{S}}_{\mathrm{oi1}}\hat{i}_{\mathrm{o1}} + T^{\mathrm{S}}_{\mathrm{oi2}}(\hat{j}_{\mathrm{o2}} + Y^{\mathrm{S}}_{\mathrm{L2}}\hat{u}_{\mathrm{o2}}) \\
\hat{u}_{\mathrm{o1}} &= G^{\mathrm{S}}_{\mathrm{io1}}\hat{u}_{\mathrm{ins}} - Z^{\mathrm{S}}_{\mathrm{o1}}\hat{i}_{\mathrm{o1}} + G^{\mathrm{S}}_{\mathrm{cr1}}(\hat{j}_{\mathrm{o2}} + Y^{\mathrm{S}}_{\mathrm{L2}}\hat{u}_{\mathrm{o2}}) \\
\hat{u}_{\mathrm{o2}} &= G^{\mathrm{S}}_{\mathrm{io2}}\hat{u}_{\mathrm{ins}} + G^{\mathrm{S}}_{\mathrm{cr2}}\hat{i}_{\mathrm{o1}} - Z^{\mathrm{S}}_{\mathrm{o2}}(\hat{j}_{\mathrm{o2}} + Y^{\mathrm{S}}_{\mathrm{L2}}\hat{u}_{\mathrm{o2}})
\end{aligned}
\tag{I.10}
$$

$$
\hat{u}_{\mathrm{o2}} = \left(\frac{G^{\mathrm{S}}_{\mathrm{io2}}}{1 + Z^{\mathrm{S}}_{\mathrm{o2}}Y^{\mathrm{S}}_{\mathrm{L2}}}\right)\hat{u}_{\mathrm{ins}} + \left(\frac{G^{\mathrm{S}}_{\mathrm{cr2}}}{1 + Z^{\mathrm{S}}_{\mathrm{o2}}Y_{\mathrm{L2}}}\right)\hat{i}_{\mathrm{o1}} - \left(\frac{Z^{\mathrm{S}}_{\mathrm{o2}}}{1 + Z^{\mathrm{S}}_{\mathrm{o2}}Y_{\mathrm{L2}}}\right)\hat{j}_{\mathrm{o2}} \tag{I.11}
$$

$$
\begin{aligned}
\hat{u}_{\mathrm{o1}} = {} & \left(G^{\mathrm{S}}_{\mathrm{io1}} + \frac{G^{\mathrm{S}}_{\mathrm{io2}}G^{\mathrm{S}}_{\mathrm{cr1}}Y_{\mathrm{L2}}}{1 + Z^{\mathrm{S}}_{\mathrm{o2}}Y_{\mathrm{L2}}}\right)\hat{u}_{\mathrm{ins}} - \left(Z^{\mathrm{S}}_{\mathrm{o1}} - \frac{G^{\mathrm{S}}_{\mathrm{cr1}}G^{\mathrm{S}}_{\mathrm{cr2}}Y_{\mathrm{L2}}}{1 + Z^{\mathrm{S}}_{\mathrm{o2}}Y_{\mathrm{L2}}}\right)\hat{i}_{\mathrm{o1}} \\
& + \left(\frac{G^{\mathrm{S}}_{\mathrm{cr1}}(1 + Z^{\mathrm{S}}_{\mathrm{o2}}Y_{\mathrm{L2}}) - G^{\mathrm{S}}_{\mathrm{cr1}}Z^{\mathrm{S}}_{\mathrm{o2}}Y_{\mathrm{L2}}}{1 + Z^{\mathrm{S}}_{\mathrm{o2}}Y_{\mathrm{L2}}}\right)\hat{j}_{\mathrm{o2}}
\end{aligned}
\tag{I.12}
$$

$$
\begin{aligned}
\hat{i}_{\mathrm{in}} = {} & \left(\frac{Y^{\mathrm{S}}_{\mathrm{in}}(1 + Z^{\mathrm{S}}_{\mathrm{o2}}Y_{\mathrm{L2}}) + Y^{\mathrm{S}}_{\mathrm{L2}}T^{\mathrm{S}}_{\mathrm{oi2}}G^{\mathrm{S}}_{\mathrm{io2}}}{1 + Z^{\mathrm{S}}_{\mathrm{o2}}Y_{\mathrm{L2}}}\right)\hat{u}_{\mathrm{ins}} + \left(\frac{T^{\mathrm{S}}_{\mathrm{oi1}}Y_{\mathrm{L2}}G^{\mathrm{S}}_{\mathrm{cr2}} + T^{\mathrm{S}}_{\mathrm{oi2}}}{1 + Z^{\mathrm{S}}_{\mathrm{o2}}Y_{\mathrm{L2}}}\right)\hat{i}_{\mathrm{o1}} \\
& + \left(\frac{T^{\mathrm{S}}_{\mathrm{oi2}}(1 + Z^{\mathrm{S}}_{\mathrm{o2}}Y_{\mathrm{L2}}) - T^{\mathrm{S}}_{\mathrm{oi2}}Y_{\mathrm{L2}}Z^{\mathrm{S}}_{\mathrm{o2}}}{1 + Z^{\mathrm{S}}_{\mathrm{o2}}Y_{\mathrm{L2}}}\right)\hat{j}_{\mathrm{o2}}
\end{aligned}
\tag{I.13}
$$

Based on these derivations, Y_{L2} influence to the system dynamics is given in (I.14), where the expression for the special output-side parameters $Z_{\text{o-oci2}}$ (I.15) is obtained from (I.13).

$$
\begin{bmatrix} \hat{i}_{\mathrm{in}} \\ \hat{u}_{\mathrm{o1}} \\ \hat{u}_{\mathrm{o2}} \end{bmatrix} =
$$

$$
\begin{bmatrix}
\frac{1+Z^{\mathrm{S}}_{\text{o-oci2}}Y_{\mathrm{L2}}}{1+Z^{\mathrm{S}}_{\mathrm{o2}}Y_{\mathrm{L2}}}Y^{\mathrm{S}}_{\mathrm{in2}} + Y^{\mathrm{S}}_{\mathrm{in1}} & T^{\mathrm{S}}_{\mathrm{oi1}} + \frac{Y_{\mathrm{L2}}G^{\mathrm{S}}_{\mathrm{cr2}}T^{\mathrm{S}}_{\mathrm{oi2}}}{1+Z^{\mathrm{S}}_{\mathrm{o2}}Y_{\mathrm{L}}} & \frac{T^{\mathrm{S}}_{\mathrm{oi2}}}{1+Z^{\mathrm{S}}_{\mathrm{o2}}Y_{\mathrm{L2}}} \\
G^{\mathrm{S}}_{\mathrm{io1}} + \frac{Y_{\mathrm{L2}}G^{\mathrm{S}}_{\mathrm{io2}}G^{\mathrm{S}}_{\mathrm{cr1}}}{1+Z^{\mathrm{S}}_{\mathrm{o2}}Y_{\mathrm{L2}}} & -(Z^{\mathrm{S}}_{\mathrm{o1}} - \frac{Y_{\mathrm{L2}}G^{\mathrm{S}}_{\mathrm{cr2}}G^{\mathrm{S}}_{\mathrm{cr1}}}{1+Z^{\mathrm{S}}_{\mathrm{o2}}Y_{\mathrm{L2}}}) & \frac{G^{\mathrm{S}}_{\mathrm{cr1}}}{1+Z^{\mathrm{S}}_{\mathrm{o2}}Y_{\mathrm{L2}}} \\
\frac{G^{\mathrm{S}}_{\mathrm{io2}}}{1+Z^{\mathrm{S}}_{\mathrm{o2}}Y_{\mathrm{L2}}} & \frac{G^{\mathrm{S}}_{\mathrm{cr2}}}{1+Z^{\mathrm{S}}_{\mathrm{o2}}Y_{\mathrm{L2}}} & -\frac{Z^{\mathrm{S}}_{\mathrm{o2}}}{1+Z_{\mathrm{o2}}Y_{\mathrm{L2}}}
\end{bmatrix}
\begin{bmatrix} \hat{u}_{\mathrm{ins}} \\ \hat{i}_{\mathrm{o1}} \\ \hat{j}_{\mathrm{o2}} \end{bmatrix}
\tag{I.14}
$$

$$Z^{\mathrm{S}}_{\text{o-oci2}} = Z^{\mathrm{S}}_{\text{o2}} + \frac{G^{\mathrm{S}}_{\text{io2}} T^{\mathrm{S}}_{\text{oi2}}}{Y^{\mathrm{S}}_{\text{in2}}} \tag{I.15}$$

J GRAPHICAL USER INTERACE OF THE OPTIMIZATION TOOL

The Graphical user interface of the optimization tool is illustrated in Fig. J.1, where the user needs to provide the following specifications:

- Source specification (System input voltage)
- Load specifications (number of loads and their static parameters, input voltage and maximum power)
- Library of commercial converter models

Utilizing this information, the tool provides a set of optimized architectural solutions and the user can compare the options in terms of optimized size, cost and efficiency and select the most appropriate solution for the intended application.

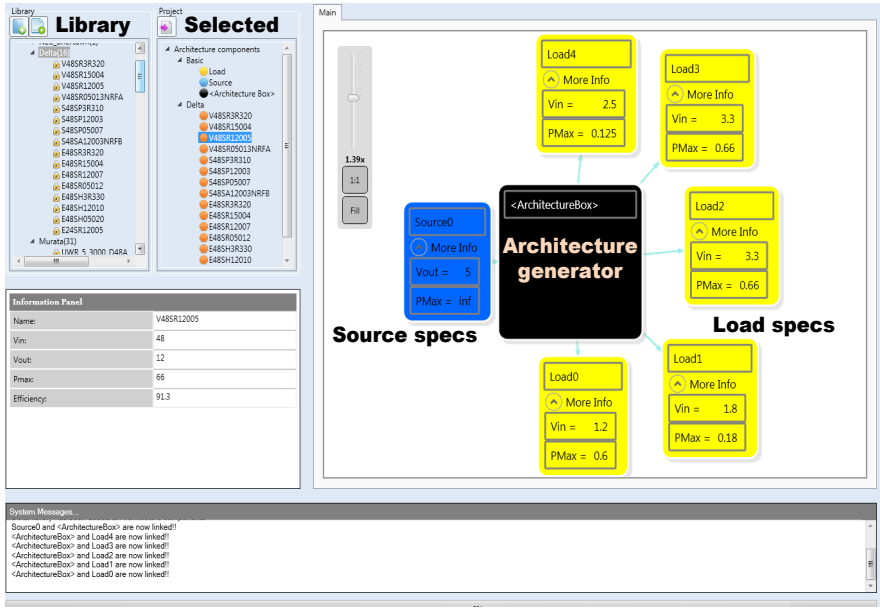

Fig. J.1: Graphical user interface of the optimization tool.

Tampereen teknillinen yliopisto
PL 527
33101 Tampere

Tampere University of Technology
P.O.B. 527
FI-33101 Tampere, Finland

ISBN 978-952-15-3584-0
ISSN 1459-2045